Characterization and Analysis of Acoustical Sensor Devices for KM3NeT and ANTARES

Masterarbeit aus der Physik

Vorgelegt von

Robert Karl

28. März 2013

Lehrstuhl für Experimentalphysik (Astroteilchenphysik)
Friedrich-Alexander-Universität Erlangen-Nürnberg

Betreuer: Prof. Dr. Uli Katz

Contents

1 Introduction

Our planet is only a tiny part in our galaxy, insignificant in our universe. Countless mysteries, from which we have not even dared to dream about, are still waiting out there in the vastness to be discovered. So we look to the stars and ask ourselves what lies out there, beyond our reach. For this reason we build telescopes, to come a little bit closer to the galaxy and its countless stars. Always on the lookout for new phenomena, new mysteries to perplex and eventually tell us more about the universe, from its earliest beginnings to its fate millennia into the future.
Starting with the first telescopes the exploration of the universe with the naked eye was on its way, limited only by the visual spectrum. This brought forth many valuable insights and discoveries, along with even more new questions and many secrets still undiscovered. For this reason new methods were sought to probe even further and obtain more information about the universe. The next step was to use particle physics, which allow the analysis of the entire electromagnetic spectrum as well as the hadronic and leptonic components of the cosmic rays.
Every part of the cosmic radiation yields a contribution to the understanding of the universe. But due to the sheer size of the galaxy many of the particles are screened by many obstacles along their way. In addition, charged particles are diverted from their course by magnetic fields, resulting in a loss of information from their point of origin. This is why neutrinos are of great interest. Since they are electromagnetically neutral, no electronic or magnetic field can influence them. Aside from that, they have only a very small cross section, allowing them to travel through objects with ease.
It is this small cross sections which makes neutrino astronomy every bit as promising as difficult. For this reason precise measurement are of great importance. Most neutrino telescopes use the optical detection of secondary particles through Cherenkov radiation measurement. Underwater neutrino telescopes rely on a precise positioning of their optical sensors which can be ensured by acoustical sensors. Apart from this, there is the possibility of using sound pulses in order to detect the interaction of neutrino with their environment on an acoustic level.
The objective of this work is a better understanding of the acoustic sensors. To this purpose, a precise characterization and a detailed analysis of acoustic sensors foreseen for KM3NeT as well as a characterization of the complete hydrophones for ANTARES were undertaken.

2 The Assignment of the acoustical Sensors in Deep Sea Neutrino Telescopes

Increasingly detailed observations of the universe require increasingly accurate and diverse detection methods. The current method of neutrino astronomy by deep sea neutrino telescopes is the measurement of Cherenkov radiation produced by the secondary particle generated by the neutrino interaction with its environment. Due to the effect of the sea current, this requires a determination of the position and orientation of the optical sensors. Nevertheless, the positioning of the optical module and, additionally, the detection of neutrino interactions with their environment, through measuring the resulting pressure impulse, can be undertaken by acoustical sensors.

2.1 Positioning System of Deep Sea Neutrino Telescopes

At the moment, the main task of acoustical sensors is the positioning of the optical modules in deep sea Cherenkov neutrino telescopes. ANTARES and KM3NeT shall representatively serve as examples for the general deep sea neutrino telescopes in this section. Thus, this positioning is illustrated with reference to the ANTARES positioning system [1], but it can also be applied for the KM3NeT. In addition, a possible expansion of the positioning system is outlined by determination of the heading with acoustical sensors.

2.1.1 Deep Sea Neutrino Telescopes

The current deep sea neutrino telescopes, such as ANTARES and KM3NeT seen in fig. 2.1, consist of several separate vertical strings (so-called lines) which are held on the ground by a heavy anchor, in the case of ANTARES called a bottom string socket (BSS), and held taut by a buoy. These strings contain the optical modules holding the photomultiplier tubes (PMT). [1]
At high enough energies, charged particles generated e.g. by neutrino interactions propagate with a velocity higher than speed of light in the same medium and thus they emit Cherenkov radiation measured by the PMTs while crossing the telescope. According to the arrival times from different PMTs and the speed of light, it is possible to reconstruct

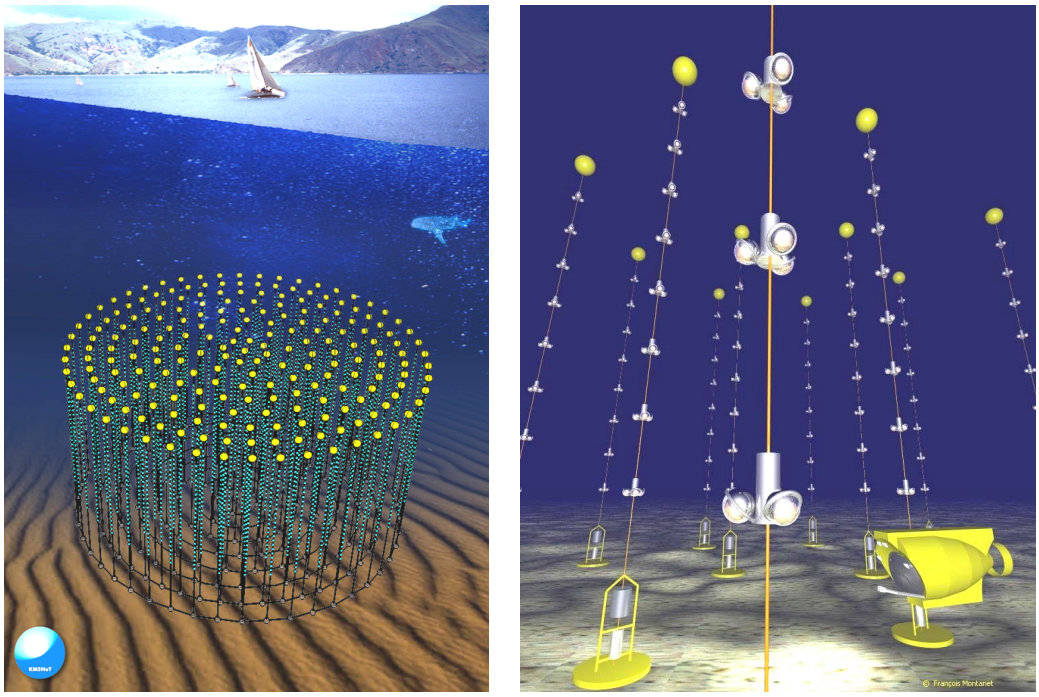

(a) KM3NeT Neutrino Telescope. Taken from [2]

(b) ANTARES Neutrino Telescope, detailing the storeys. Taken from [3]

Figure 2.1: Artworks of two deep sea neutrino telescopes

the path of the particle. Hence, the uncertainty in the reconstruction is inter alia constituted by the uncertainty in the position and the heading of the optical modules.
Due to the structure of the lines, they are only fixed to the sea floor, while the rest is displaced from the vertical and rotated along the line axis by the sea current. This causes a time dependent change in the optical module position and heading, which has to be considered for the reconstruction of the particle path. For a precise reconstruction, it is necessary to know the current orientation of the optical module; consequently, a system has to be installed to obtain the values of the orientation. [1]

2.1.2 Positioning of the Optical Modules

There are two different subsystems of the ANTARES positioning system; the low frequency long baseline (LFLBL) and the high frequency long baseline positioning system (HFLBL). The LFLBL uses the 8-16 kHz frequency range allowing the measurement of long propagation times, meaning that distances up to 8km can be resolved. Therefore, this system is well suited to determine the position of ANTARES structures by triangulation from a ship on the sea surface. [1]
Of greater interest for the application of acoustical sensors is the HFLBL. It determines the position of the detector elements relative to the BSS position with high precision by measuring the travel times of acoustical sinusoidal pulses between an acoustical

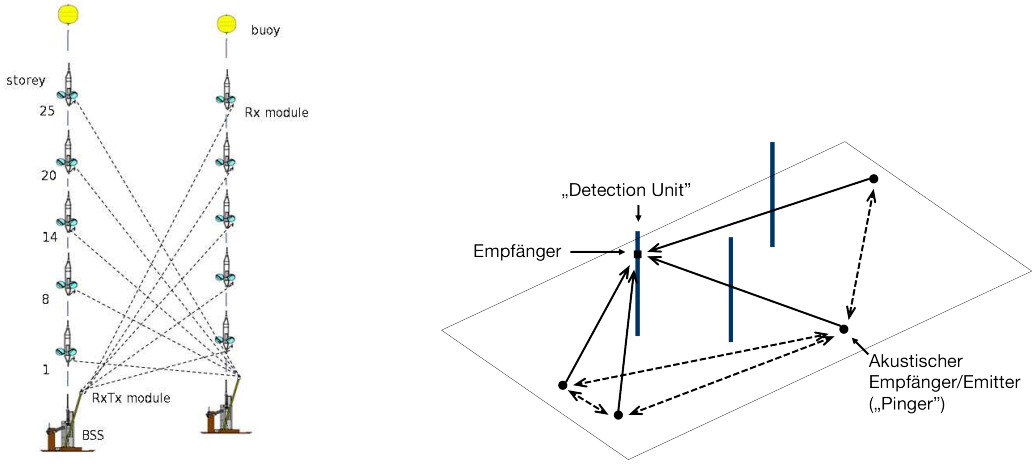

(a) for two complete lines of ANTARES. Taken from [1]

(b) for several emitter of different positions

Figure 2.2: Schematic demonstrating the principle of the positioning system

transceiver at the anchor and the hydrophones on a detector line in the frequency range from 40 to 60 kHz. Then the position of the hydrophones is obtained by triangulation [1]. The transceiver, fixed on a rod at the BSS, is operated as receiver and emitter (RxTx module). The receiving hydrophones (Rx modules) are carried by five different storeys of a detection line. Each RxTx module successively sends acoustical wave packets (typical duration 2ms) at different frequencies to unambiguously identify the emitting module. The acoustical emission is organized in a periodic succession of cycles consisting of the emissions of all RxTx modules at their respective frequencies between 44.522kHz and 60.235kHz in a predefined sequence. In the case that an acoustical signal is detected at the given parameters, all receiving modules provide both the detection time and the measured amplitude. A schematic of the HFLBL system is shown in fig. 2.2(a). [1]
After convolution with the sea sound profile, the distance between an emitter (called "pinger") and a detection unit (e.g. a hydrophone) is obtained; a schematic is shown in fig. 2.2(b). With respect of the known pinger positions, at least three distances for a receiving module are necessary to make the calculation of a three-dimensional triangulation for the module position possible. Usually, there are more than three distances which leads to a over-determination. Therefore, the positions are obtained by minimization through an iterative convergence procedure [1]. For more detail, see [1].

For ANTARES, the inclination of a storey is measured by a compass tilt meter system [1]. The tilt measurement is based on the movement of a fluid in the sensor due to the inclination of the storey. For the determination of the heading angle, i.e. rotation around the line axis, three flux tube magnetic sensors measure the Earth's magnetic field in three perpendicular local directions.
Through the integration of two acoustical sensors in a module, exemplarily seen in fig. 2.3(a), it is also possible to measure the position together with the heading using the acoustical sensors. Fig. 2.3(b) shows the differences in heading between both

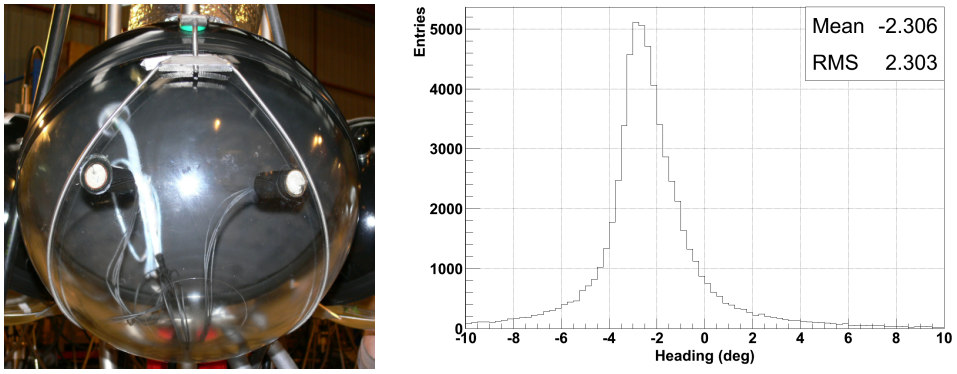

(a) Two included acoustical modules

(b) The difference in heading

Figure 2.3: The heading received by acoustical sensors as compared to compass-tiltmeter system

measurements. According to a mean difference of only about 2.3°, the acoustical determination of the heading yields results with a similar accuracy.
All together, the acoustical sensors can ensure the complete determination of the position and orientation of the storeys. Thus, They prove themselves valuable for the optical particle detection in deep sea neutrino telescopes.

2.2 Acoustical Neutrino Detection

A prospective task of acoustical sensors is to measure the sound signal caused by a neutrino interaction. The creation of acoustic signals by elementary particles in water or similar media was first described by G. A. Askaryan and B. A. Dolgoshein in the so-called thermo-acoustic model [4].

2.2.1 The Thermo-Acoustic Model

If a neutrino interacts with its environment, more precisely interacting with a quark in an atomic nucleus, it can generate a charged lepton through the weak interaction. In the case of e.g. a muon neutrino or muon antineutrino, eq. 2.1 shows an exemplary reaction.

$$\nu_\mu + d \longrightarrow \mu^- + u \tag{2.1a}$$
$$\overline{\nu}_\mu + u \longrightarrow \mu^+ + d \tag{2.1b}$$

Muons generated by this reaction are one kind of secondary particles which are detected by the optical modules, if their energy is high enough to produce Cherenkov radiation. Such a reaction also leads to a hadronic cascade (also called hadronic shower), according

to the thermo-acoustic model, resulting in a near-instantaneous heating of the surrounded water volume. Consequently, the volume expands creating a pressure pulse. This kind of pressure pulse is bipolar, its amplitude is understandable as the magnitude of the expansion resulting from the heating and it is roughly linear in the neutrino's energy, depending greatly on both distance and direction with respect to the hadronic cascade. While the actual shape depends on the lateral density distribution assumed for the cascade. The characteristic frequency depends on both the lateral dimensions of the shower "core" and the speed of sound in the medium. For water, it is close to 20 kHz. Fig. 2.4(a) shows the resulting bipolar pressure signal for three different parameterizations of energy deposition. [5, sec. 2.3]

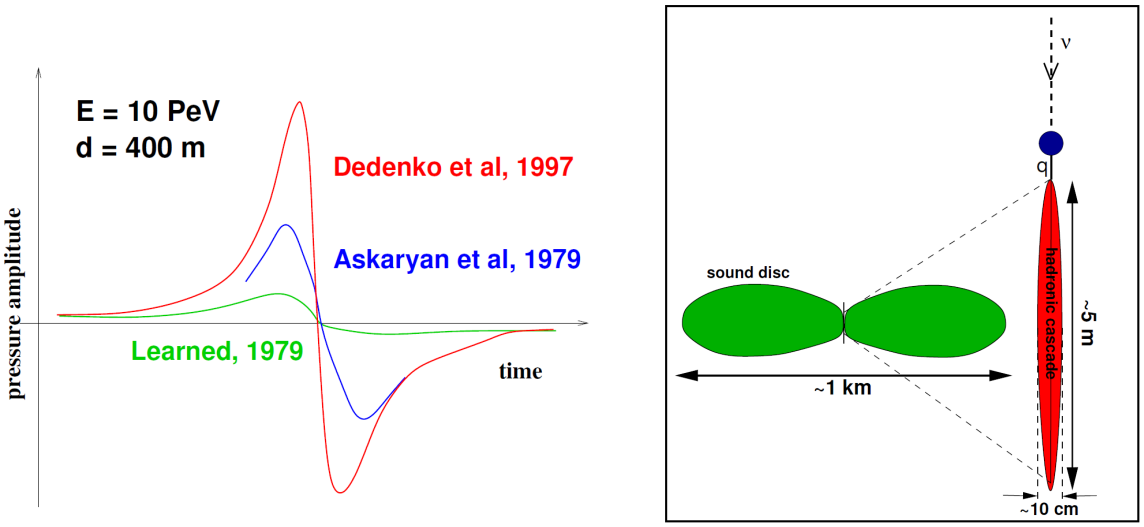

(a) Thermo-acoustic pressure signals for a 10 PeV primary in 400 m distance, for different modeling of the energy deposition.

(b) Sketch of the geometry of the hadronic shower and the resulting sound "disc". The x and y dimensions of both the shower and the disc are not to scale, with the shorter dimension greatly exaggerated.

Figure 2.4: The thermo acoustic signal and its geometry of a particle interaction. The figures were taken from [5].

The shape of the sound source is basically the shape of a cigar about 5 meters long and about 5 to 10cm in diameter, see fig. 2.4(b). Almost the total signal power is emitted within a narrow disc ("pancake") perpendicular to the hadronic cascade and its initial thickness is given by the length of the cascade.
Corresponding to this disc slowly widening for longer distances from the shower axis, only a few degrees outside the centre plane there is virtually no signal amplitude left. "This peculiar geometry of the sound field is indicative of the thermo-acoustic signal generation, of great importance for both the suppression of point-like transient noise sources and for the reconstruction of the direction of flight of the original neutrino." By ignoring the absorption and near-field effects, the pressure signal amplitude scales

with the inverse distance to the shower axis inside the sound "disc", thus $p(r) \propto 1/r$. [5, sec. 2.3]

2.2.2 Detection in the Deep Sea

With roughly ten times greater attenuation length in the frequency range of interest as compared to light, the range of sound is much larger in the water, which allows the construction of much larger detector volumes for the acoustical particle detection with a moderate increase of the number of individual detector elements. Thus, by increasing the inter-sensor distance by one order of magnitude, an acoustical detector could easily be three orders of magnitude greater than an optical one with the same number of sensors. [5, sec. 2.3]
"Ocean water is both the best understood and most easily accessible as compared to ice and salt. The acoustic properties of sea water are well known from long-running military and civilian research campaigns. In general, the energy thresholds for acoustic detection in water are well above the EeV scale, due to the intrinsically relatively low signal amplitudes and the presence of acoustic noise. Ongoing efforts are focusing on means of lowering this threshold by improved site selection, signal processing and background rejection." Finally, the combination of e.g. optical and acoustical particle detection in a single telescope could make the simultaneous detection of a neutrino possible, resulting in a reduction of the respective intrinsic errors. [5, sec. 2.3]

3 Characterization of the Amplifiers of the acoustical Sensor

Goal of this chapter is to find the transfer function which reconstructs the output signal $U_{\text{out}}(t)$ from a given input signal $U_{\text{in}}(t)$.
For this purpose, two different ways of characterization are used to arrive at the best approximation of the transfer function. This has been done to make sure that artefacts are based on the amplifier and not on a mismatch of the measurement setup.
Both ways are separately used for the master and pre-amplifier to obtain a transfer function for each amplifier. The principle idea is to treat both amplifiers as independent systems. So only the output signal from the pre-amplifier is used as input signal for the master amplifier without any other interaction between the amplifiers.
After the transfer function was found, it was tested on a reconstruction of the output signal from the given input signal. This was done to see which parts are well reconstructed and which characteristics could be used for further analysis.

3.1 Theoretical Background

In this section, a heuristic derivation to find the transfer function is explained, in addition the theoretical background of the two experimental procedures, *Sine-* and *Pulse-Analysis*, are demonstrated in detail.
Note that the main focus of this chapter is on the approximation of the measured data.

3.1.1 Frequency Response

Each amplifier is made up of cascading low and high pass filters. These filter were treated independently as were the amplifiers. So, for the nth filter the output signal is given by

$$\frac{U_{\text{in}}^{(n)}}{Z_{\text{in}}^{(n)}} = \frac{U_{\text{out}}^{(n)}}{Z_{\text{out}}^{(n)}} \qquad \Rightarrow \qquad U_{\text{out}}^{(n)} = \frac{Z_{\text{out}}^{(n)}}{Z_{\text{in}}^{(n)}} \cdot U_{\text{in}}^{(n)} \tag{3.1}$$

For the (n+1)th filter, the input signal is equal to the output signal of the nth filter. From this follows that

$$U_{\text{out}}^{(n+1)} = \frac{Z_{\text{out}}^{(n+1)}}{Z_{\text{in}}^{(n+1)}} \cdot U_{\text{in}}^{(n+1)} = \frac{Z_{\text{out}}^{(n+1)}}{Z_{\text{in}}^{(n+1)}} \cdot U_{\text{out}}^{(n)} = \frac{Z_{\text{out}}^{(n+1)}}{Z_{\text{in}}^{(n+1)}} \cdot \frac{Z_{\text{out}}^{(n)}}{Z_{\text{in}}^{(n)}} \cdot U_{\text{in}}^{(n)} \tag{3.2}$$

The output signal of the whole amplifier is given by

$$U_{\text{out}} = \prod_{i=1}^{N} \left(\frac{Z_{\text{out}}^{(i)}}{Z_{\text{in}}^{(i)}} \right) \cdot U_{\text{in}} = H \cdot U_{\text{in}} \tag{3.3}$$

However, Z is an impedance and depends on the frequency of the input signal. So, eq. 3.3 describes the behavior only for single frequencies. Therefore, the output signal is transformed into the Fourier space to describe it by a frequency depended quantity $\hat{U}_{\text{out}}(\omega)$. From this follows that

$$U_{\text{out}}(t) = \int_{\mathbb{R}} \frac{\mathrm{d}\omega}{\sqrt{2\pi}} \hat{U}_{\text{out}}(\omega)\, e^{i\,\omega\cdot t} = \int_{\mathbb{R}} \frac{\mathrm{d}\omega}{\sqrt{2\pi}} \hat{H}(\omega) \cdot \hat{U}_{\text{in}}(\omega)\, e^{i\,\omega\cdot t} \tag{3.4a}$$

$$\Rightarrow U_{\text{out}}(t) = \left(H \otimes U_{\text{in}}\right)(t) \tag{3.4b}$$

$$\text{with} \quad U_{\text{in}}(t) = \int_{\mathbb{R}} \frac{\mathrm{d}\omega}{\sqrt{2\pi}} \hat{U}_{\text{in}}(\omega)\, e^{i\,\omega\cdot t} \tag{3.4c}$$

$$H(t) = \int_{\mathbb{R}} \frac{\mathrm{d}\omega}{\sqrt{2\pi}} \hat{H}(\omega)\, e^{i\,\omega\cdot t} \tag{3.4d}$$

Therefore, to get the output signal, the convolution of the transfer function with the input signal has to be calculated. But first, $\hat{H}(\omega)$ had to be calculated.
To determine the transfer function $\hat{H}(\omega)$ by experiment, eq. 3.3 is solved for $\hat{H}$ and from this follows:

$$\hat{H}(\omega) = \frac{\hat{U}_{\text{out}}(\omega)}{\hat{U}_{\text{in}}(\omega)} \tag{3.5}$$

Note that $\hat{H}(\omega)$ is a complex quantity, thus $\hat{U}_{\text{out}}(\omega)$ and $\hat{U}_{\text{in}}(\omega)$ are treated as complex quantities, too. W.l.o.g. $\hat{H}(\omega)$, $\hat{U}_{\text{out}}(\omega)$ and $\hat{U}_{\text{in}}(\omega)$ can be described by

$$\hat{H}(\omega) = \hat{A}(\omega)\, \exp\left(i\varphi(\omega)\right) \tag{3.6a}$$

$$\hat{U}_{\text{out}}(\omega) = \hat{A}_{\text{out}}(\omega)\, \exp\left(i\varphi_{\text{out}}(\omega)\right) \tag{3.6b}$$

$$\hat{U}_{\text{in}}(\omega) = \hat{A}_{\text{in}}(\omega)\, \exp\left(i\varphi_{\text{in}}(\omega)\right) \tag{3.6c}$$

So $\hat{H}(\omega)$ can calculate via $\hat{A}$ and φ which are given by

$$\hat{A} = \frac{\hat{A}_{\text{out}}}{\hat{A}_{\text{in}}} := \left| \frac{\hat{U}_{\text{out}}}{\hat{U}_{\text{in}}} \right| \tag{3.7a}$$

$$\varphi = \varphi_{\text{out}} - \varphi_{\text{in}} \tag{3.7b}$$

Now, only the determination of the four parameters $\hat{A}_{\text{out}}$, $\hat{A}_{\text{in}}$, φ_{out}, φ_{in} are missing. These four parameters are determined by two different methods as mentioned earlier. This will be the focus of the next subsections.

To determine the transfer function $\hat{H}(\omega)$ by an analytic function, $\hat{A}$ and φ can also be calculated via

$$\hat{H}(\omega) = \hat{A}\, \exp(i\varphi) = \prod_{k=1}^{N} \left(\frac{Z_{\text{out}}^{(k)}}{Z_{\text{in}}^{(k)}} \right) \tag{3.8a}$$

$$\Rightarrow \hat{A}\, \exp(i\varphi) = \prod_{k=1}^{N} \left(\hat{A}_k\, \exp(i\varphi_k) \right) = \prod_{k=1}^{N} \left(\frac{Z_{\text{out}}^{(k)}}{Z_{\text{in}}^{(k)}} \right) \tag{3.8b}$$

$$\Rightarrow \hat{A}_k\, \exp(i\varphi_k) = \frac{Z_{\text{out}}^{(k)}}{Z_{\text{in}}^{(k)}} \tag{3.8c}$$

It can be seen, that $\hat{A}_k$ and φ_k are defined by the magnitude and phase of the impedance ratio. This yields an analytic function which approximates the transfer function $\hat{H}(\omega)$. The parameters of this analytic function are initialized by the theoretical values and determined by a fit to the measured data given in eq. 3.6. This will be discussed in detail in chap. 3.2.
Note that in the following the focus will be on the search for $\hat{H}(\omega)$ instead of $H(t)$ because it is easier to compare with the theoretical found function and it is better suited for numeric calculations.

3.1.2 Sine-Analysis

One way to determinate $\hat{A}$ and φ by experiment is to measure each frequency separately. To do this, a constant sine signal is sent through the amplifier and both the incoming and outgoing signals are measured.
To characterize the whole frequency spectrum, the input and output signals are measured for M different frequencies $f_m = \omega_m / 2\pi$ with $m \in \{0, \ldots, M-1\}$. Each signal can be described by

$$U_{\text{out}}^{(m)}(t) = A_{\text{out}}^{(m)}\, \sin\left(2\pi f_m t + \varphi_{\text{out}}^{(m)} \right) + O_{\text{out}}^{(m)} \tag{3.9a}$$

$$U_{\text{in}}^{(m)}(t) = A_{\text{in}}^{(m)}\, \sin\left(2\pi f_m t + \varphi_{\text{in}}^{(m)} \right) + O_{\text{in}}^{(m)} \tag{3.9b}$$

The transfer function $\hat{H}(f)$ can now be calculated from the parameters of the input and output signals for the discrete frequencies f_m. From this follows, that

$$\hat{H}(f_m) := \hat{H}_m := A_m\, \exp(i\varphi_m) \tag{3.10a}$$

$$A_m := \frac{A_{\text{out}}^{(m)}}{A_{\text{in}}^{(m)}} \tag{3.10b}$$

$$\varphi_m := \varphi_{\text{out}}^{(m)} - \varphi_{\text{in}}^{(m)} \tag{3.10c}$$

W.l.o.g. the magnitudes A_m, $A_{\text{out}}^{(m)}$ and $A_{\text{in}}^{(m)}$ can be assumed as positive in this analysis, because negative magnitudes can be represented with a shift of the phase, i.e.

$$A_m \longrightarrow A'_m := |A_m| \tag{3.11a}$$

$$\varphi_m \longrightarrow \varphi'_m := \varphi_m \pm \pi \tag{3.11b}$$

Note that there is no use for the constant offsets $O_{\text{out}}^{(m)}$ and $O_{\text{in}}^{(m)}$ in this analysis, but to get a correct parameterization of the signals they are essential.
Another important thing is that the sine is a 2π-periodic function, so the phase φ_m is defined only in the interval $[-\pi, \pi]$. This has the result that

$$\varphi \longrightarrow \varphi + 2n\pi \quad \text{with } n \in \mathbb{Z} \tag{3.12}$$

has no effect on the parameterization of the signal. Because the transfer function will be approximated by an analytic function, it must be ensured that the values of $\hat{H}_m$ can be described by a continuous function. To implement that an integer k_m for each measure is chosen, so that

$$\left|\varphi_m - \varphi'_{m+1}\right| < 2\pi \tag{3.13a}$$

$$\varphi'_{m+1} := \varphi_{m+1} + 2k_m\pi \quad \forall m \in \{0, \ldots, M-2\} \tag{3.13b}$$

3.1.3 Pulse-Analysis

The other way used in this analysis is to measure all frequencies at once. So an input signal which is constant in frequency is sent through the amplifier, i.e.

$$\hat{U}_{\text{in}}(\omega) = \hat{U}_0 \tag{3.14a}$$

$$\Rightarrow U_{\text{out}}(t) = \int_{\mathbb{R}} \frac{\mathrm{d}\omega}{\sqrt{2\pi}}\, \hat{H}(\omega) \cdot \hat{U}_{\text{in}}(\omega)\, e^{i\,\omega\cdot t} = \hat{U}_0 \cdot \int_{\mathbb{R}} \frac{\mathrm{d}\omega}{\sqrt{2\pi}}\, \hat{H}(\omega)\, e^{i\,\omega\cdot t} \tag{3.14b}$$

$$\Rightarrow \hat{H}(\omega) = \int_{\mathbb{R}} \frac{\mathrm{d}t}{\sqrt{2\pi}}\, U_{\text{out}}(t)/\hat{U}_0\, e^{-i\,\omega\cdot t} \tag{3.14c}$$

To find a time dependent input signal to which this applies, $\hat{U}_{\text{in}}(\omega)$ is Fourier transformed into the time domain. From this follows that

$$U_{\text{in}}(t) = \int_{\mathbb{R}} \frac{\mathrm{d}\omega}{\sqrt{2\pi}}\, \hat{U}_{\text{in}}(\omega)\, e^{i\,\omega\cdot t} = \hat{U}_0 \cdot \int_{\mathbb{R}} \frac{\mathrm{d}\omega}{\sqrt{2\pi}}\, e^{i\,\omega\cdot t} = \sqrt{2\pi}\hat{U}_0\, \delta(t) \tag{3.15}$$

In theory, a δ-pulse, being flat in the frequency domain, is sent through the amplifier and the output signal is already proportional to the time dependent transfer function. To get the frequency dependent function, the normed output signal has to be Fourier transformed.
However, it is not possible to create an exact δ-pulse. So it has to be approximated by a Gaussian-distribution. That implies

$$U_{\text{in}}(t) := U_0\, \exp\left(-\frac{t^2}{2\tau^2}\right) \tag{3.16a}$$

$$\begin{aligned}\hat{U}_{\text{in}}(\omega) &= \int_{\mathbb{R}} \frac{\mathrm{d}t}{\sqrt{2\pi}}\, U_{\text{in}}(t)\, e^{i\,\omega\cdot t} = U_0 \cdot \int_{\mathbb{R}} \frac{\mathrm{d}t}{\sqrt{2\pi}}\, \exp\left(-\frac{t^2}{2\tau^2}\right)\, e^{i\,\omega\cdot t} \\ &= U_0 \cdot \tau \cdot \exp\left(-\tau^2\omega^2/2\right) = \hat{U}_0 \cdot \exp\left(-\frac{\omega^2}{2\omega_0^2}\right)\end{aligned} \tag{3.16b}$$

$$\text{with} \qquad \hat{U}_0 := U_0 \cdot \tau, \quad \omega_0 := \frac{1}{\tau} \tag{3.16c}$$

As eq. 3.16 shows, a δ-pulse can be created if τ approaches zero. Because of the fact that τ could not be exactly zero, the frequency spectrum will not be perfectly flat. But if τ is small enough, the spectrum will be only slightly curved. In this way, eq. 3.14c changes to

$$\hat{H}(\omega) = \exp\left(\frac{\omega^2}{2\omega_0^2}\right) \int_{\mathbb{R}} \frac{\mathrm{d}t}{\sqrt{2\pi}}\, U_{\mathrm{out}}(t)/\hat{U}_0\, e^{-i\,\omega\cdot t} \tag{3.17}$$

Note that for high frequencies ($\omega \gg \omega_0$) eq. 3.17 loses its validity because the frequency spectrum of the input signal is not exactly flat and spectrum converges to zero. So the spectrum gets an additional cut off and thereby it is treated as limited.
To flatten out the spectrum as far as possible, τ has to be as small as possible but $\hat{U}_0$ also becomes small as seen in eq. 3.16c. If $\hat{U}_0$ is too low, the frequency dependent input signal cannot be well distinguished from the background noise. It is not possible to simply increase U_0 because the amplifier would just overdrive or in the worst case it could be damaged.
To get a significant input signal, the Gaussian-pulses will be sent in periodic intervals. Then, the single Gaussian-pulses are averaged, i.e.

$$U_{\mathrm{in}}(t) := \sum_{k=0}^{K-1} U_0\, \exp\left(-\frac{(t-kT)^2}{2\tau^2}\right) \tag{3.18a}$$

$$\overline{U_{\mathrm{in}}}(t) = \frac{1}{K-1} \sum_{k=0}^{K} U_{\mathrm{in}}\,(t+kT) \qquad \forall t \in [-T/2, T/2] \tag{3.18b}$$

$$\overline{U_{\mathrm{out}}}(t) = \frac{1}{K-1} \sum_{k=0}^{K} U_{\mathrm{out}}\,(t+kT) \qquad \forall t \in [-T/2, T/2] \tag{3.18c}$$

$$\tag{3.18d}$$

Following this step, the averaged signals are used for the further analysis.
Another important fact is that the time interval of the measurement is limited. Meaning if the measurement starts at time $-t_0$ and stops at t_0, eq. 3.17 changes to

$$\hat{H}(\omega) = \exp\left(\frac{\omega^2}{2\omega_0^2}\right) \int_{-t_0}^{t_0} \frac{\mathrm{d}t}{\sqrt{2\pi}}\, U_{\mathrm{out}}(t)/\hat{U}_0\, e^{-i\,\omega\cdot t} \tag{3.19a}$$

$$= \exp\left(\frac{\omega^2}{2\omega_0^2}\right) \int_{-\infty}^{\infty} \frac{\mathrm{d}t}{\sqrt{2\pi}} 1_{[-t_0,\,t_0]}\,(t)\; U_{\mathrm{out}}(t)/\hat{U}_0\, e^{-i\,\omega\cdot t} \tag{3.19b}$$

$$= \exp\left(\frac{\omega^2}{2\omega_0^2}\right) \left(\sqrt{\frac{2}{\pi}} \underbrace{\frac{\sin\,(t_0\omega)}{\omega}}_{\propto\, \mathrm{sinc}(\omega)} \otimes \int_{\mathbb{R}} \frac{\mathrm{d}t}{\sqrt{2\pi}}\, U_{\mathrm{out}}(t)/\hat{U}_0\, e^{-i\,\omega\cdot t} \right) \tag{3.19c}$$

$$1_{[-t_0,\,t_0]}\,(t) := \begin{cases} 1 & \text{if } t \in [-t_0,\, t_0] \\ 0 & \text{otherwise} \end{cases} \tag{3.19d}$$

The result of the limited time interval is a convolution with a sinc-function in the frequency domain. So it must be ensured that artefacts in the Fourier transformation which are based on the sinc-function are not used for the further analysis. Note that the Fourier transformation is also a 2π periodic in the phase. Therefore, the phase has to be smoothed as described in eq. 3.13.

3.2 Measurement of the Amplifiers

In this section, the characterization of the main- and pre-amplifier are discussed separately in detail.
For this purpose, the experimental data is taken and approximated, as mentioned in sec. 3.1, for each amplifier. The input signals are generated by a function generator and sent to both the amplifier and an oscilloscope. The input and output signals are averaged and stored by the oscilloscope. The oscilloscope has a maximum sampling frequency of 1GHz. However, the sampling frequency is automatically adjusted to the set time interval by the oscilloscope, thus it differs slightly for each measurement.
The sine signals are averaged to minimize background noise and thereby receiving clear sine signals. The pulse signals are averaged as described in eq. 3.18, also minimizing background noise.
The further analysis and the graphical representation of the data are provided by ROOT [6].
After that, the data of the first prototype of the pre-amplifier is presented as an example why it is sensible to use more than one kind of characterization.

3.2.1 Master amplifier

In the first step, the data of the Sine-Analysis are discussed. The frequency spectrum of the master amplifier is approximated over 114 different frequencies and for each frequency a sine signal is sent through the amplifier as mentioned in sec. 3.1.2. Examples of the input signal are shown in fig. 3.1 and of the output signal in fig. 3.2.
To get the current parameters of the sine signals, each signal is approximated by a sine fit. The fit searches for a minimum in the χ^2-domain, yet there are more local minima for a sine fit, thus it is not easy to find the absolute one. It depends on a precise estimation on the initial fit values. If they are not accurate enough, the fit will probably find a local minimum, but not the absolute one. This results in a failure of the fit and consequently in a miscalculation of the fit parameters.
Because the initial values are generically determined, it may happen that they are not precise enough and the fit fails. However, the parameters of a failed fit are definitely wrong and this would lead to miscalculation of the transfer function. If this could not be fixed for all frequencies, those where the fit obviously failed have to be sorted out and were not taken into account for the further calculation of the transfer function. Alternatively, the initial values would have to be determined manually, but this is not advisably for time reasons. An example of such a fit failure will addressed in sec. 3.2.2.
The generic decision whether a fit has failed is made by the RMS ΔU of the residuals

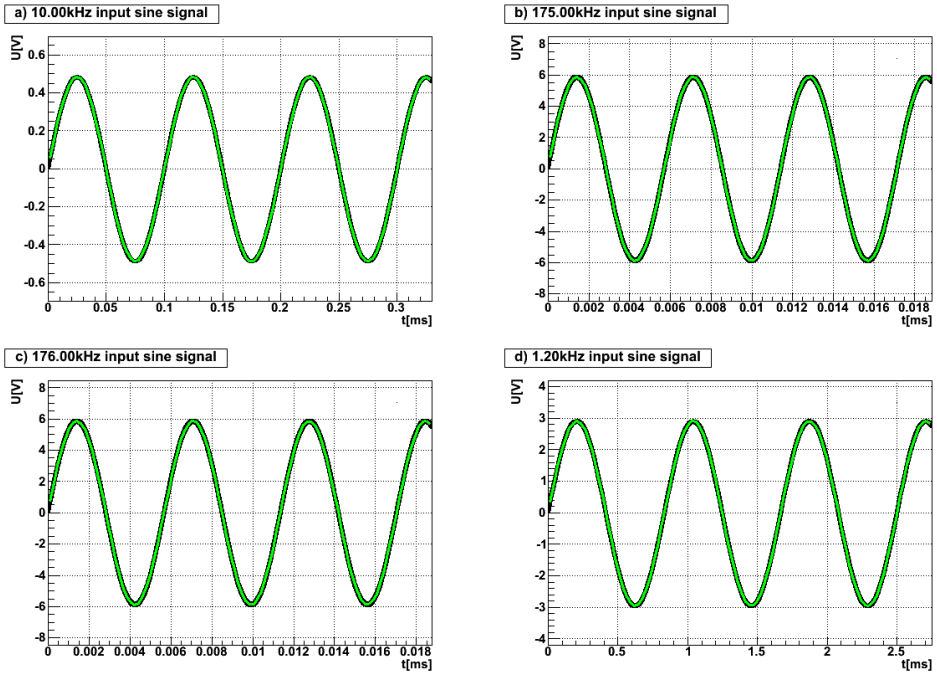

Figure 3.1: Input signals for four different frequencies. The *black* curve represents the measured data and the *green* line shows the approximation by the fit

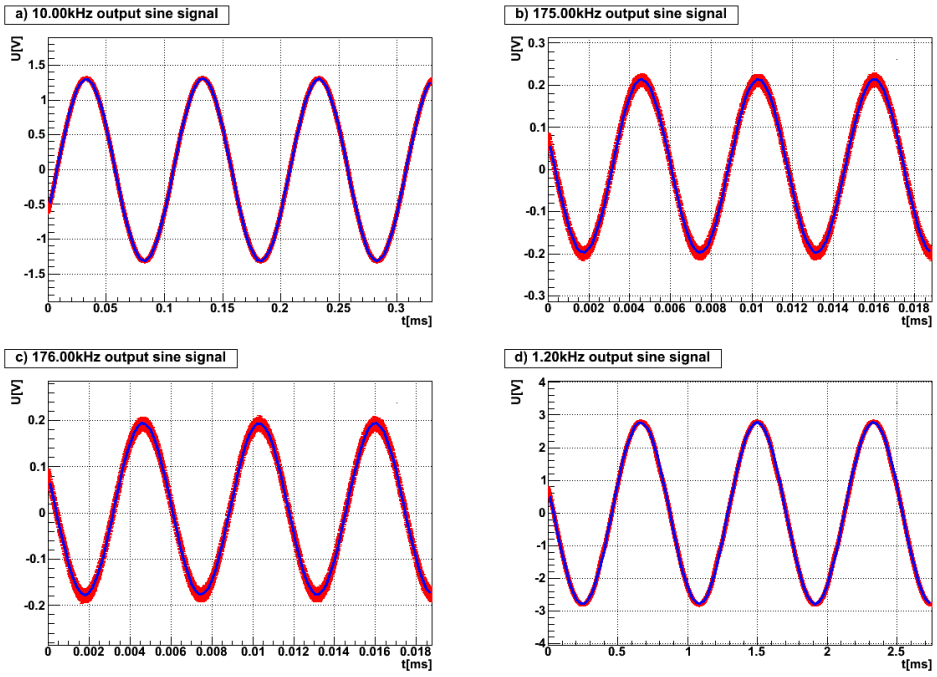

Figure 3.2: Output signals for four different frequencies. The *red* curve represents the measured data and the *blue* line shows the approximation by the fit

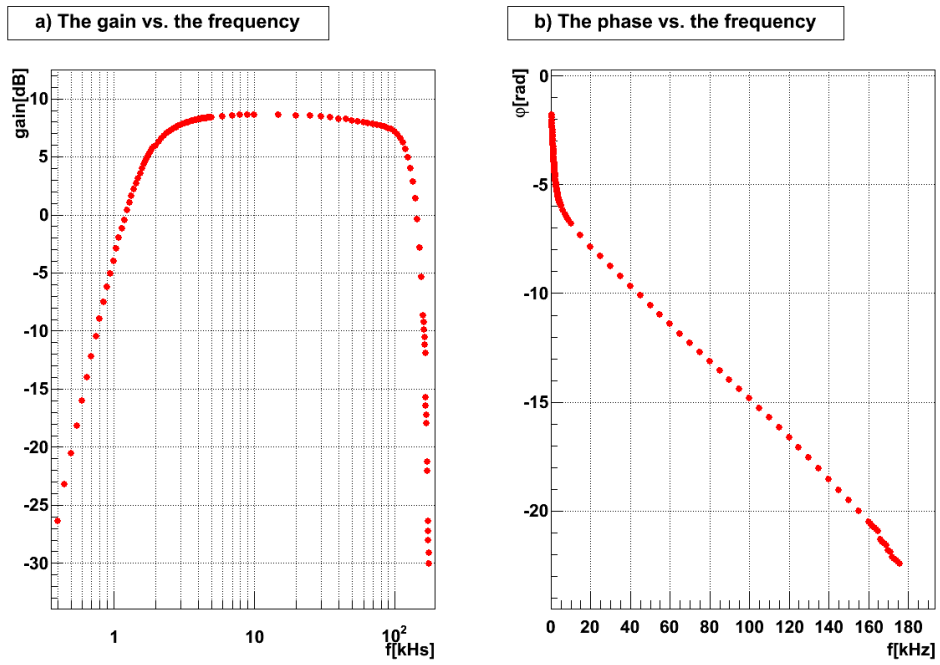

Figure 3.3: The gain (*left*) and phase (*right*) of the transfer function determined by the sine signals as a function of the frequency

between the measured signal U_k at time t_k and the fit function $u(t)$. As usual the RMS is defined by

$$\Delta U := \sqrt{\frac{1}{K}\sum_{k=0}^{K-1}\left(U_k - u\left(t_k\right)\right)^2} \tag{3.20}$$

A fit is considered to have failed if $\Delta U \geq 0.02V$. This value is estimated on the one hand by the precision of the measurements (2σ), and on the other hand by the fit results of a few selected measurements.
Fig. 3.3 shows the gain ($20 \cdot \log_{10}\left(A_m\right)$) and the phase ($\varphi_m$) of the transfer function as given in eq. 3.10. Both quantities describe a continuous map and no artefacts have been occurred. Thus, the 114 frequencies are used for further analysis.

In the next step, the data of the Pulse-Analysis will be discussed. As mentioned in sec. 3.1.3, four different Gaussian pulses are periodically sent through the amplifier. The incoming and outgoing signals were averaged over 1000 sweeps, as described in eq. 3.18. Examples of these averaged signals are shown in fig. 3.4 and 3.5. Primarily, the amplitude of the input Gaussian signal can be set arbitrarily, but it had to be ensured that on the one hand, the amplifier do not overdrive and, on the other hand, the signal was powerful enough to distinguish the output signal from background noise. Consequently, the amplitude of the input signal were set for each pulse separately. The wider the pulse, the smaller its frequency spectrum and thus the lower frequencies are more involved; the

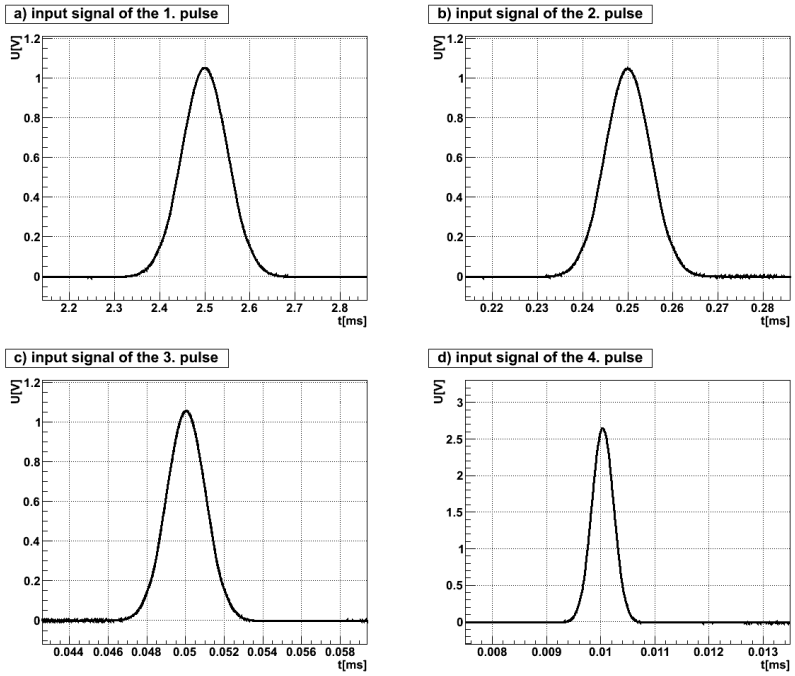

Figure 3.4: The four input Gaussian pulses of various width. The pulses have already been averaged as described in eq. 3.18

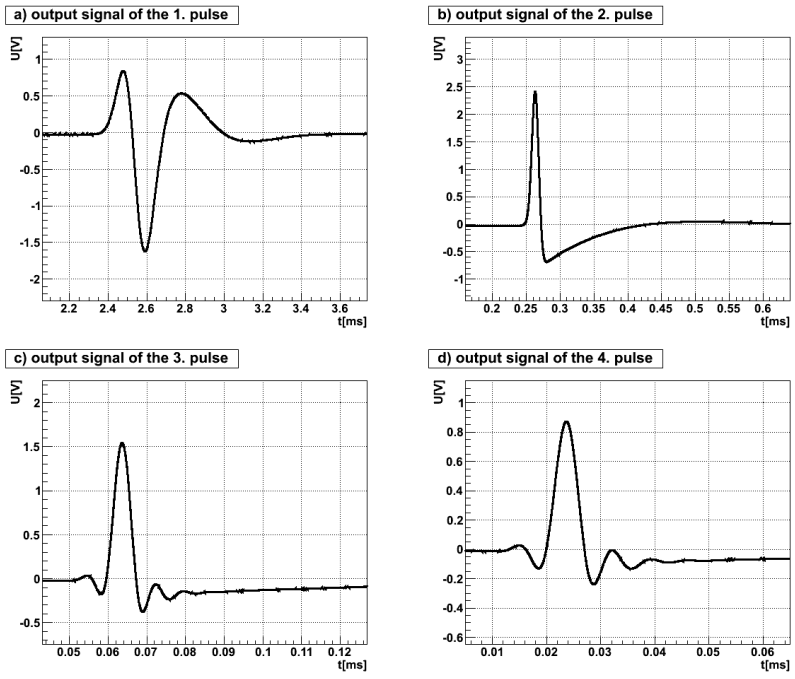

Figure 3.5: The four response signals of the input Gaussian pulses. The response signals have already been averaged as described in eq. 3.18

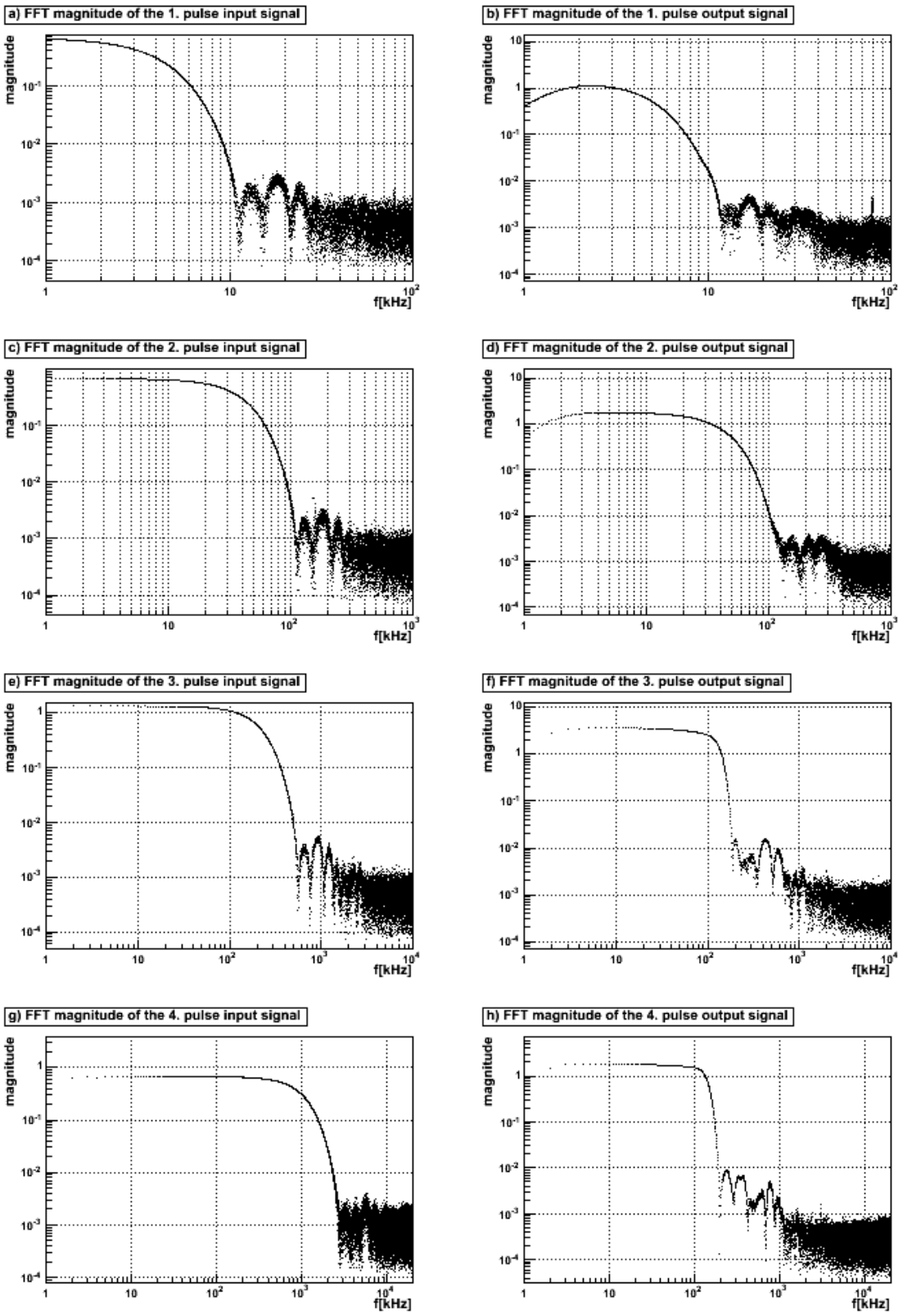

Figure 3.6: The FFTW magnitude of the input and output signal double logarithmically plotted

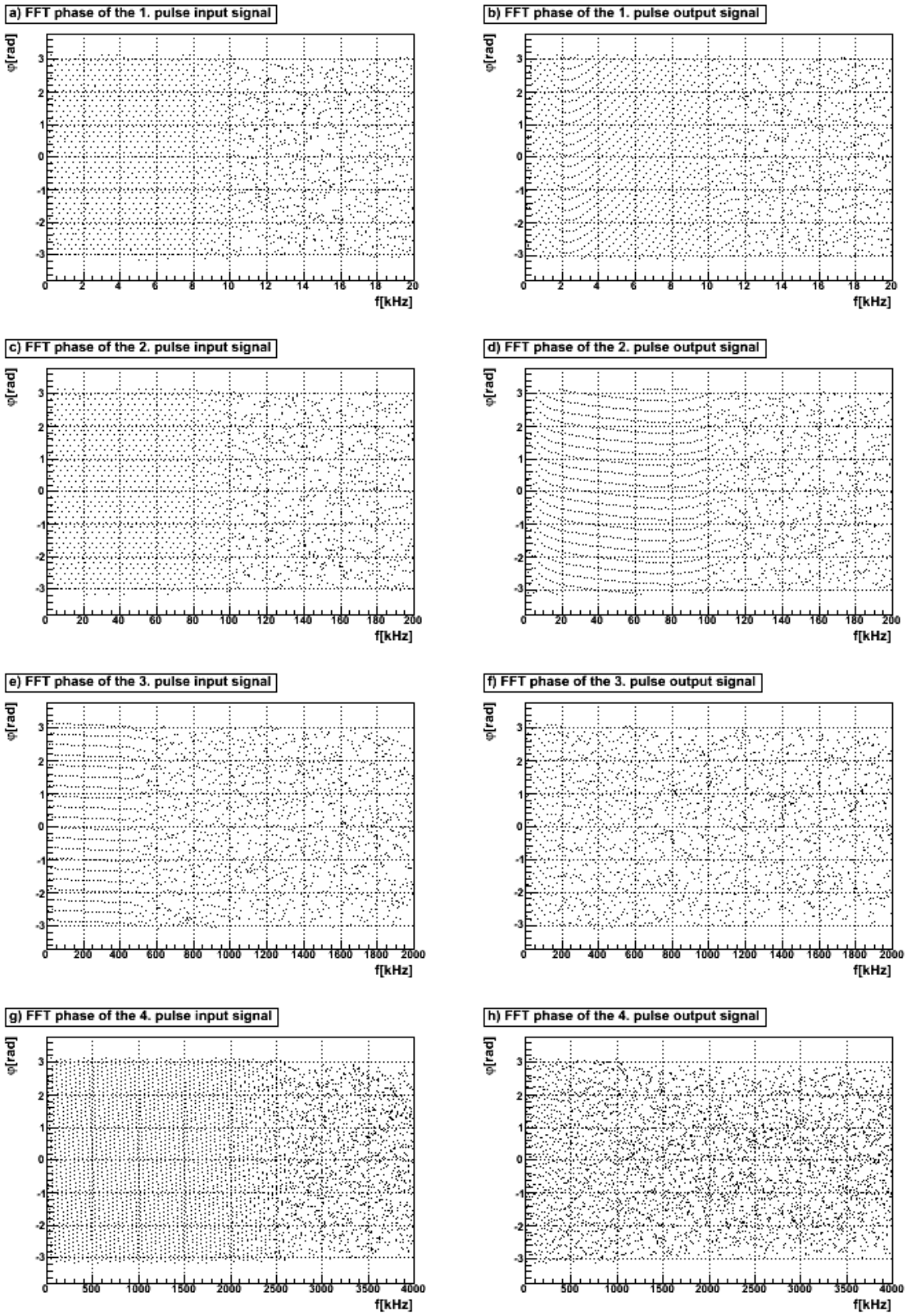

Figure 3.7: The FFTW phase of the input and output signal

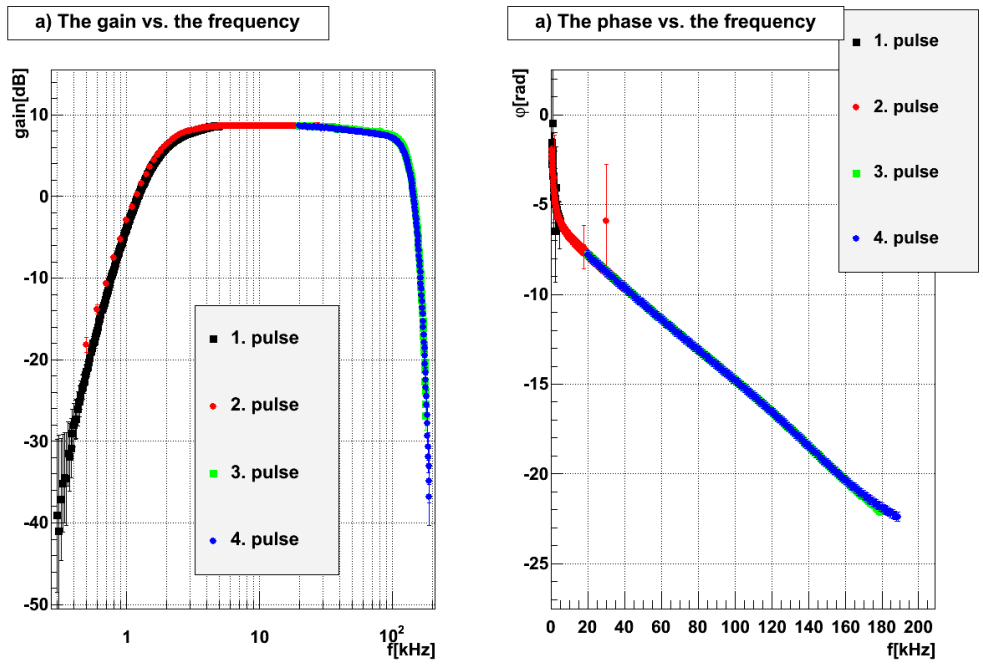

Figure 3.8: The gain (*left*) and phase (*right*) of the transfer function determined by the four Gaussian signals as a function of the frequency.

smaller the pulse the wider its frequency spectrum and thus the higher frequencies are more involved, respectively. For this reason, the widths of the pulses were determined so that the full spectrum is involved.
By using the *Fastest Fourier Transform in the West* (FFTW) the frequency spectra of the input and output signals were generated. To minimize the fluctuations of the FFTW the four generated spectra are averaged a second time by using 300 of these averaged signals for each spectrum.
The magnitude of the averaged spectra is shown in fig. 3.6 and the phase in fig 3.7. On closer inspection of the magnitude, after the decrease of the spectrum, there are side maxima. A Fourier transformation of a Gaussian results in a Gaussian again as seen in eq. 3.16c. So the side maxima do not probably belong to the FFT of the input Gaussian signal. In fact, it seems that they are an artefact of the limited measurement period, shown in eq. 3.19. Therefore, the spectra of the magnitude are cut off the decrease, just before the maxima, and only this first the part is used.
As can be seen in fig. 3.7, for the most part, the phase seems to be homogenously distributed. However, up to the frequency at which the side maxima occur a pattern can be seen and beyond it, the phase seems to be statistically distributed, especially for the phase of input signal. The reason for this statistic distribution are the fluctuations which dominate after the decreasing of the spectrum. Therefore, the spectra of the phase gets the same cut off as the magnitude. Even if the absolute phase of both the input and the output signals seem to be homogenously distributed, the difference between these phases is essential for the signal reconstruction. It is very important that the phase has

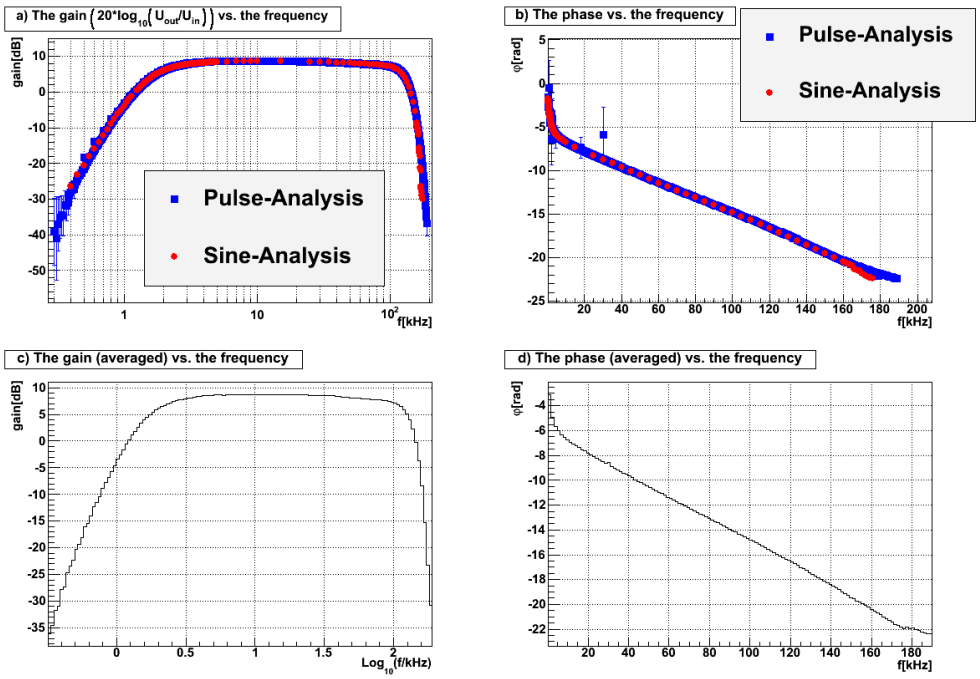

Figure 3.9: The upper pictures show the experimentally found transfer function of both characterizations used. The pictures below show the average of both ways via a histogram respectively.

to be taken into account for the further analysis.
To get the transfer function, the spectra of the magnitude were divided and those of the phase were subtracted, i.e. for each frequency the value of the magnitude of the output signal is divided by its respective input signal value, while the value of the output signal's phase is subtracted by the respective phase value of the input signal. Note that the phase has to be smoothed, as described in eq. 3.13, too
The result is given in fig. 3.8 showing that, depending on the width of a single pulse, a different part of the frequency spectrum can be better approximated. Care had been taken that there had been an overlap of the single parts to get an continuous distribution by averaging of the single parts. If that had not been the case, it would have been difficult adjusting the parts to each other, in order to ensure a continuous distribution.

In the last step, the data from both methods of characterization, Sine- and Pulse-Analysis, are merged and approximated by an analytic function. It can be seen that both ways describe the same frequency response of both the gain (fig. 3.9a) and the phase (fig. 3.9b). So, it can be assumed that there are no side effects which could disturb the system as the two methods yields the same result independently. But there are always fluctuations in a measurement so the frequency response cannot be mathematically identical. Therefore, to get a better approximation, all measured data are smoothed. The smoothed gain is shown in fig. 3.9c and the smoothed phase in fig. 3.9d. As described in sec. 3.1.1, the analytic function approximating the transfer function is

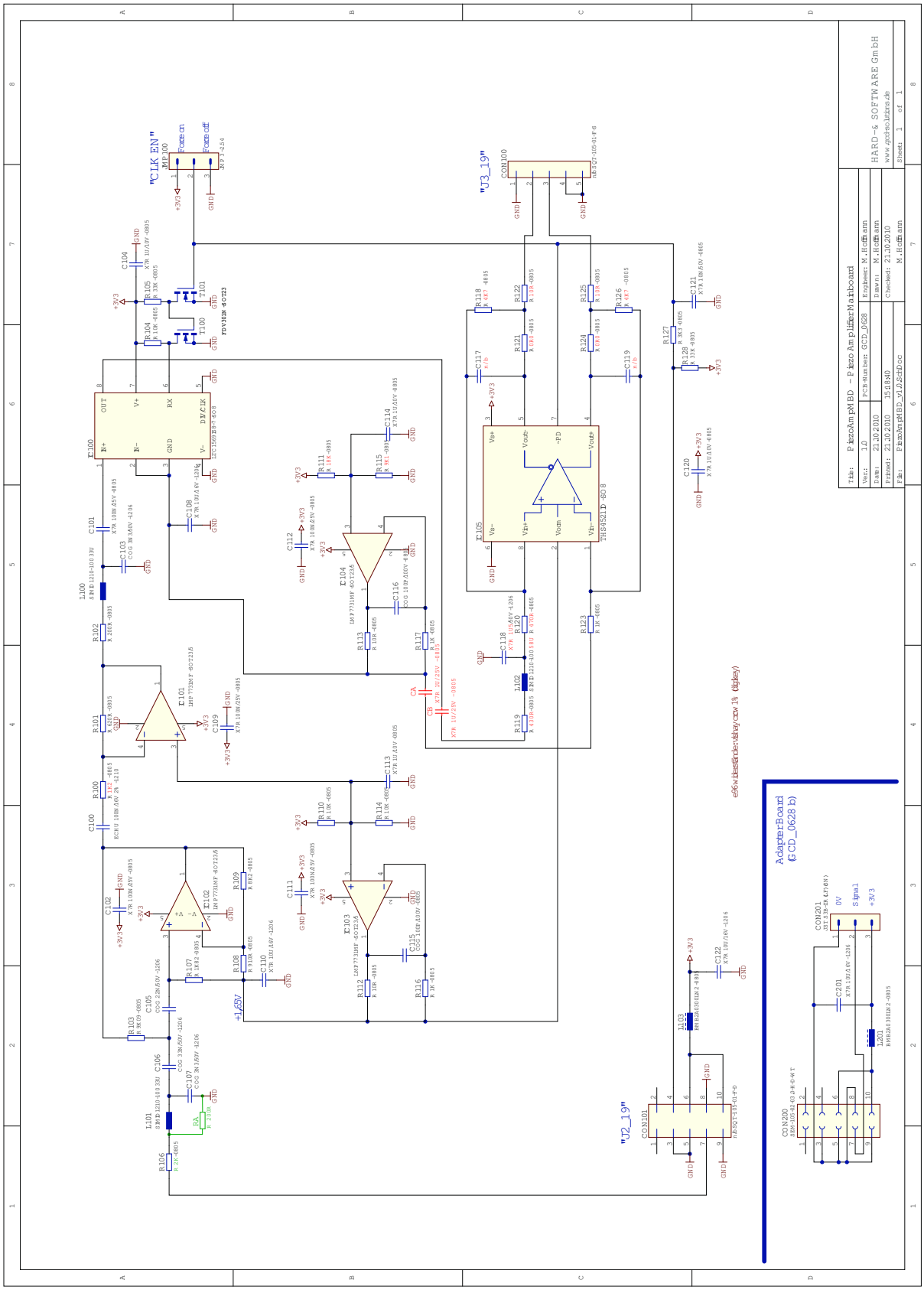

Figure 3.10: The schematic of the master amplifier.

generated by the low and high pass filters used in the amplifier. As the schematics in fig. 3.10 show the master amplifier is made of a cascade of one Sallen-Key-high pass, one first order high pass, three second order low passes and one 10th Order Low pass Filter of type *LTC1569-7*. Since there is no exact mathematical function available for the LTC, its magnitude is approximated by three general nth order low pass filters and its phase by the linear term. For a better approximation of the transfer function, it was necessary to add an additional nth order high pass filter.
As demonstrated in eq. 3.8, the transfer function is split up into in the single magnitudes and phases of the resistance ratio. Thus, the gain of the transfer function was calculated from the magnitude of the impedance ratio and it is given by

$$A = A_{\text{tot}} \cdot \prod_{i=1}^{1} \left[A_i^{\text{sallen}}\right] \cdot \prod_{j=1}^{2} \left[A_j^{\text{high}}\right] \cdot \prod_{k=1}^{3} \left[A_k^{\text{low}}\right] \cdot \prod_{l=1}^{3} \left[A_l^{\text{general}}\right] \tag{3.21a}$$

$$A_i^{\text{sallen}} = \frac{\left(f/f_i^{\text{sallen}}\right)^2}{\sqrt{\left(1-\left(f/f_i^{\text{sallen}}\right)^2\right)^2 + \delta_i^{\text{sallen}} \cdot \left(f/f_i^{\text{sallen}}\right)^2}} \quad (\textit{Sallen-Key high pass}) \tag{3.21b}$$

$$A_j^{\text{high}} = \left(\frac{f/f_j^{\text{high}}}{\sqrt{1+\left(f/f_j^{\text{high}}\right)^2}}\right)^{n_j^{\text{high}}} \quad (\textit{nth order high pass}) \tag{3.21c}$$

$$A_k^{\text{low}} = \frac{1}{\sqrt{\left(1-\left(f/f_k^{\text{low}}\right)^2\right)^2 + \delta_k^{\text{low}} \cdot \left(f/f_k^{\text{low}}\right)^2}} \quad (\textit{2nd order low pass}) \tag{3.21d}$$

$$A_l^{\text{general}} = \frac{1}{\sqrt{1+\left(f/f_l^{\text{general}}\right)^{2 \cdot n_l^{\text{general}}}}} \quad (\textit{general nth order low pass}) \tag{3.21e}$$

The phase of the transfer function is calculated from the phase of the impedance ratio and it is given by

$$\varphi = \varphi_{\text{tot}} + \sum_{i=1}^{1} \left[\varphi_i^{\text{sallen}}\right] + \sum_{j=1}^{2} \left[\varphi_j^{\text{high}}\right] + \sum_{k=1}^{3} \left[\varphi_k^{\text{low}}\right] + \varphi^{\text{lin}} \tag{3.22a}$$

$$\varphi_i^{\text{sallen}} = \arctan\left(\frac{\sqrt{\delta_i^{\text{sallen}}} \cdot f/f_i^{\text{sallen}}}{\left(f/f_i^{\text{sallen}}\right)^2 - 1}\right) \quad (\textit{Sallen-Key high pass}) \tag{3.22b}$$

$$\varphi_j^{\text{high}} = n_j^{\text{high}} \cdot \left(\pi/2 - \arctan\left(f/f_j^{\text{high}}\right)\right) \quad (\textit{nth order high pass}) \tag{3.22c}$$

$$\varphi_k^{\text{low}} = \arctan\left(\frac{\sqrt{\delta_i^{\text{low}}} \cdot f/f_i^{\text{low}}}{\left(f/f_i^{\text{low}}\right)^2 - 1}\right) \quad (\textit{2nd order low pass}) \tag{3.22d}$$

$$\varphi^{\text{lin}} = -2\pi \cdot \delta^{\text{lin}} \cdot f \quad (\textit{linear phase}) \tag{3.22e}$$

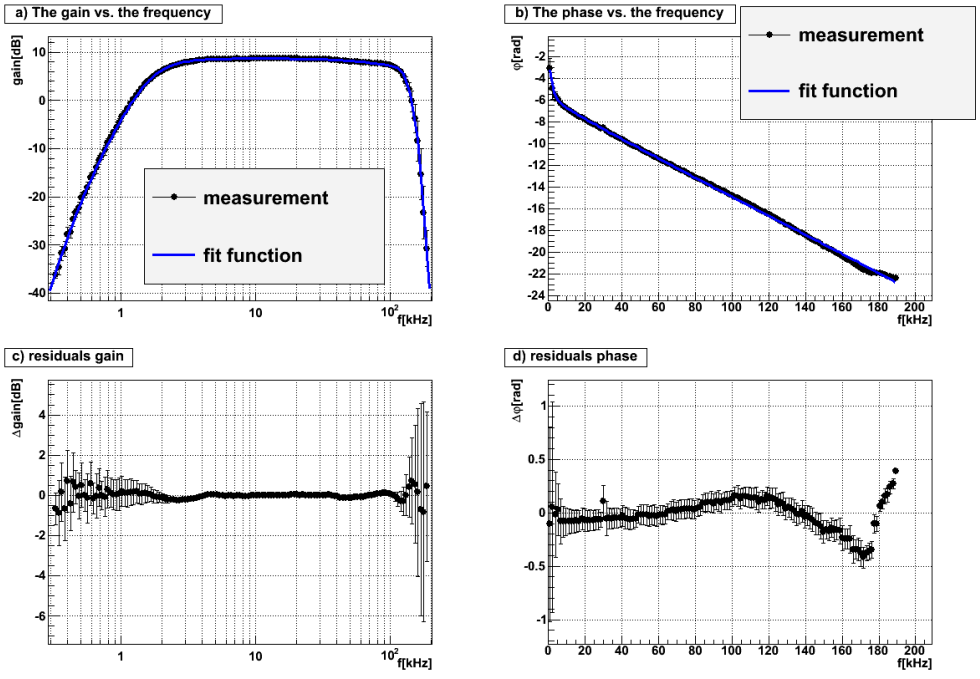

Figure 3.11: In the upper pictures the averaged transfer function (*black curve*) and its fit function (*blue line*) are shown. The pictures below shows the linear residuals respectively and the errors are taken directly from the data.

As a consequence, there are 19 free parameters of the gain and 14 of the phase to adjust.

The initial fit values of these 33 parameters are calculated from the impedances seen in fig. 3.10. Finding the minimum in a 19 dimensional χ^2-domain is not trivial and it was not possible for the fit to converge to a minimum, i.e. the result of the fit can be a good approximation but it does not have to. However, there are only 20 different parameters, because some of the gain and phase function parameters are identical. Nevertheless, all 33 parameters are treated as independent, because possible differences could have been caused by the fluctuations of the measurement or by the fact that the functions for the gain and the phase do not generate the exact transfer function, but rather an approximation of it.
To get another criterion whether the function approximates the measured data the linear residuals between the function and the data are used. To this end, the fit is repeated with the parameter values of the previous fit as new initial values, and iterated until the residuals becomes as low as possible.
Note that in this case the number of iterations cannot be arbitrarily high. At some point the residuals increases again. This happens because the fit cannot find any minimum in the χ^2-domain and it has to be aborted manually.
The final result is shown in fig. 3.11. As can seen, frequencies lower than 0.3kHz and higher than 200kHz are so strongly suppressed that the output signal could not be discerned from the background noise any more. So potential artefacts at these frequencies could not be studied. It has been assumed that the function can be analytical continued. There are obvious fluctuations in the residuals of the phase at frequencies higher than 100kHz as seen in fig. 3.11d. The reason is that the phase of the 10th Order Low Pass chip is not exact linear, as assumed. However, these fluctuations are in accordance with the measuring inaccuracy.
The final values of the parameterization of the transfer function are given in tab. 3.1. There are two things to be noted. First, as expected the parameters of the gain and the phase have partial discrepancies ($\approx 2\sigma$). Second, the values of the filter order are not always integers but they should be. As previously mentioned, this is due to the fact that on the one hand the analytic function does not exactly describe the transfer function but only an approximation, and on the other hand it is caused by the measurement's fluctuations.

3.2.2 Pre-amplifier

The pre-amplifier is characterized in the same way as the master amplifier. There are two things to be noted. First, this is the second prototype of the pre-amplifier but with identical schematics as the first one. The situation of the first pre-amplifier prototype and the reasons, why it has to be rebuilt, are described in the next section. Second, because of the high gain of the pre-amplifier a frequency independent voltage divider is used between the function generator and the amplifier for the characterization. But for calculation of the transfer function it has been taken into account so that the transfer function describes the original behavior without this voltage divider.
The following will focus on the characterization with sine signals. The frequency spectrum of the pre-amplifier is approximated by 82 sine signal with different frequencies.

total gain:	2.733e+000 ± 4.915e-004	
total phase:	-1.554e+001 ± 2.646e-002	
1. high pass	frequency f_1^{high} [kHz]	order n_1^{high}
gain	8.776e-001 ± 1.434e-001	7.770e-001 ± 1.391e-001
phase	6.489e-001 ± 1.883e-001	7.225e-001 ± 2.095e-001
2. high pass	frequency f_2^{high} [kHz]	order n_2^{high}
gain	2.183e-001 ± 4.374e-002	5.288e+000 ± 1.275e+000
phase	2.021e-001 ± 5.104e-002	3.910e+000 ± 9.874e-001
1. low pass	frequency f_1^{low} [kHz]	shift δ_1^{low}
gain	5.710e+002 ± 2.979e+001	1.504e+001 ± 7.427e-001
phase	6.028e+002 ± 1.333e+001	1.489e+001 ± 5.600e-001
2. low pass	frequency f_2^{low} [kHz]	shift δ_2^{low}
gain	2.422e+002 ± 9.356e+000	4.063e-002 ± 1.024e-002
phase	2.454e+002 ± 1.153e+001	5.497e-002 ± 1.167e-002
3. low pass	frequency f_3^{low} [kHz]	shift δ_3^{low}
gain	2.929e+002 ± 1.769e+001	5.779e+000 ± 1.270e-001
phase	3.919e+002 ± 2.159e+001	4.308e+000 ± 2.094e-001
1. Sallen-Key high pass	frequency f_1^{sallen} [kHz]	shift δ_1^{sallen}
gain	1.714e+000 ± 2.111e-002	1.897e+000 ± 2.545e-002
phase	1.472e+000 ± 1.026e-001	1.639e+000 ± 3.984e-001
general low pass	frequency f_1^{general} [kHz]	order n_1^{general}
1. low pass	1.320e+002 ± 1.985e+000	8.241e+000 ± 9.172e-001
2. low pass	1.648e+002 ± 6.212e+000	1.417e+001 ± 3.425e+000
3. low pass	3.235e+002 ± 6.270e+001	2.218e+001 ± 4.970e+000
linear phase [ms]:	1.212e-002 ± 5.638e-005	

Table 3.1: The final parameter values for the functions describe in eq. 3.21 and 3.22

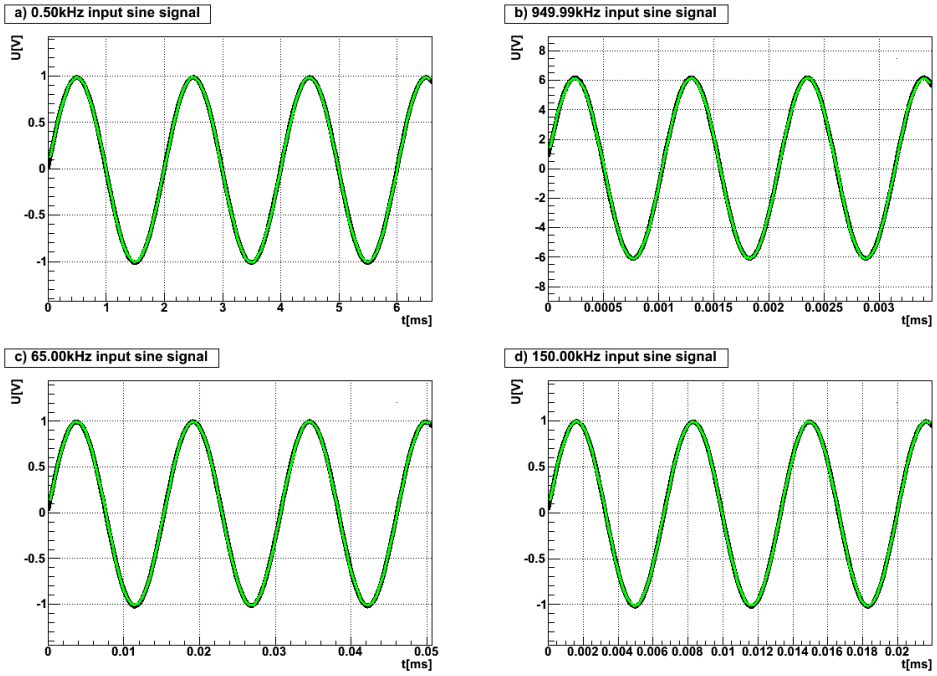

Figure 3.12: Input signals for four different frequencies. The *black* curve represents the measured data and the *green* line shows the approximation by the fit

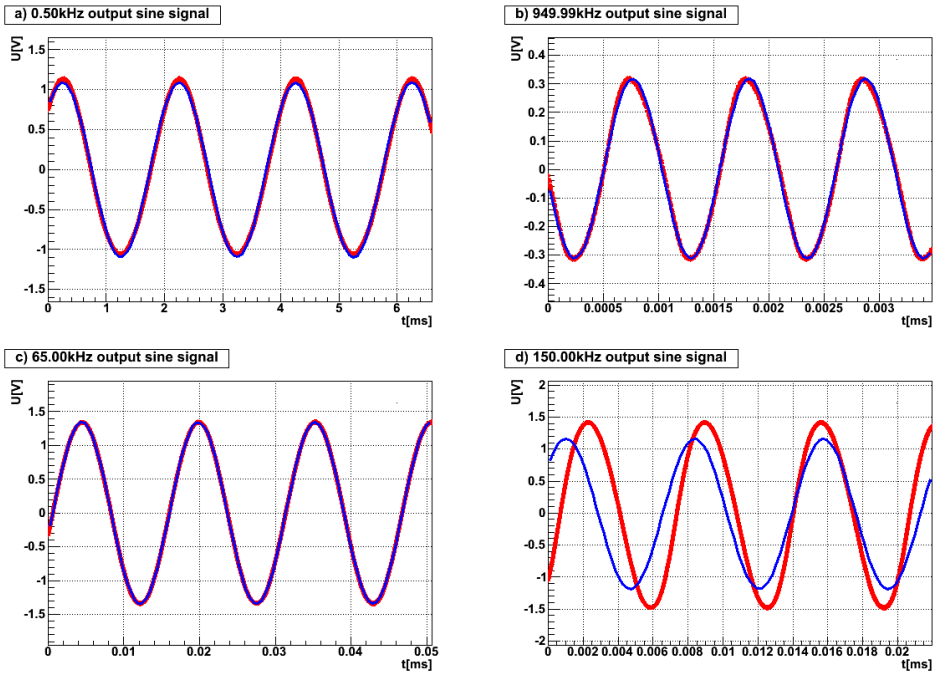

Figure 3.13: Output signals for four different frequencies. The *red* curve represents the measured data and the *blue* line shows the approximation by the fit

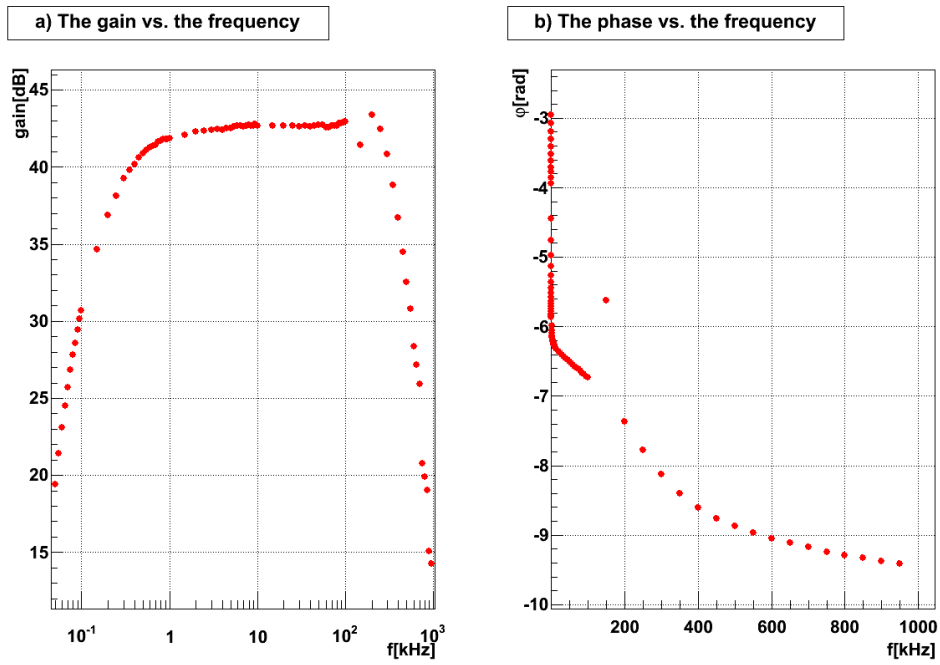

Figure 3.14: The gain (*left*) and phase (*right*) of the transfer function determined by the sine signals as a function of the frequency

Four examples of the input signal are given in fig. 3.12 and four of the output signal in fig. 3.13. As previously mentioned, without a precise determination of the initial fit values the fit cannot find the absolute minimum in the χ^2-domain and thus the fit fails. The generic decision, whether the fit has failed or not, is made by the linear residuals ΔU defined in eq. 3.20. Now, the fit is considered to have failed if $\Delta U \geq 0.1$. It was possible to determine the generic initial values, so that only one fit has failed, which can be seen in fig. 3.13d. This fit must not be taken into account for the further analysis, resulting in its removal. Otherwise, it would lead to a miscalculation of the transfer function.
The whole spectrum is shown in fig. 3.14. It can be seen, that the spectrum describes a continuous distribution except for this one value at 150kHz caused by the failed fit. This is an example of how notable the effect of a miscalculated fit is and it should illustrate the importance of its removal.

The next part will focus on the characterization by four Gaussian pulses with different widths. The incoming and outgoing signals are averaged by 1000 sweeps as described in eq. 3.18. The averaged input Gaussian pulses are shown in fig. 3.15 whereas the averaged response signals are shown in fig 3.16 respectively. As it was done for the master amplifier the amplitudes of the input pulses are set so that the amplifier on the one hand do not overdrive and on the other hand output signal is powerful enough to be distinguished from the background noise.
By using the FFTW, the frequency spectra of the input and output signals are generated. To minimize the fluctuations of the FFTW, the spectra are separately averaged by

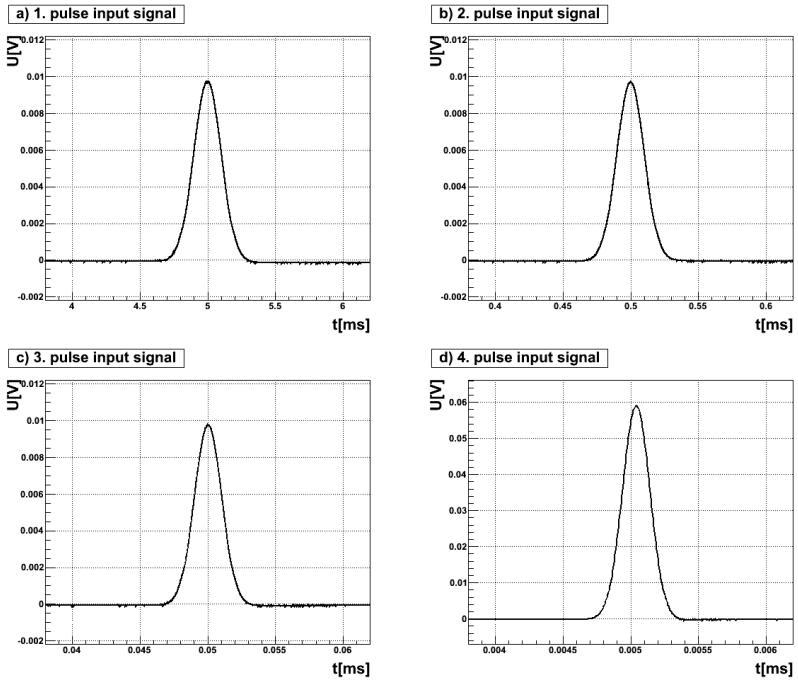

Figure 3.15: The four input Gaussian pulses of different width. The pulses have already been averaged as described in eq. 3.18

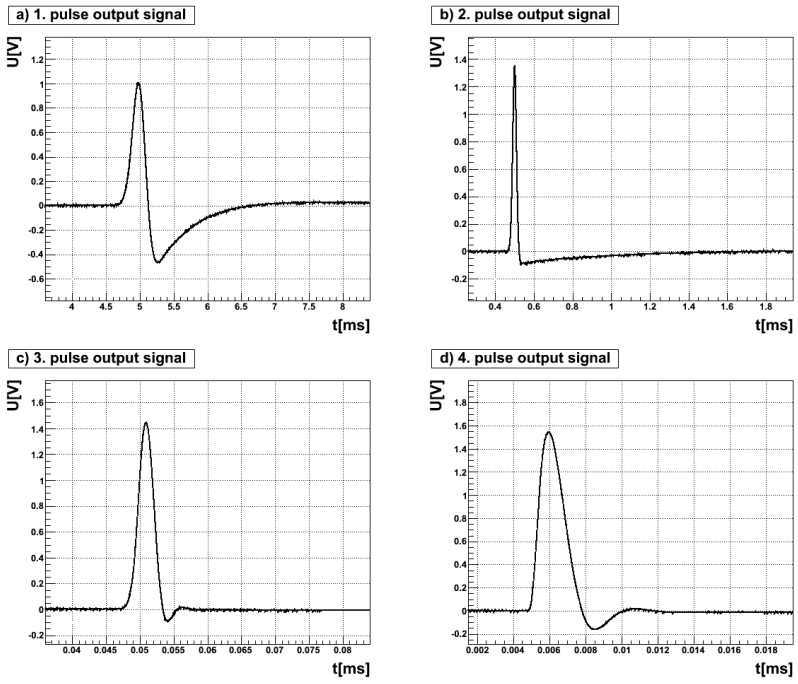

Figure 3.16: The four response signals of the input Gaussian pulses. The response signals have already been averaged as described in eq. 3.18

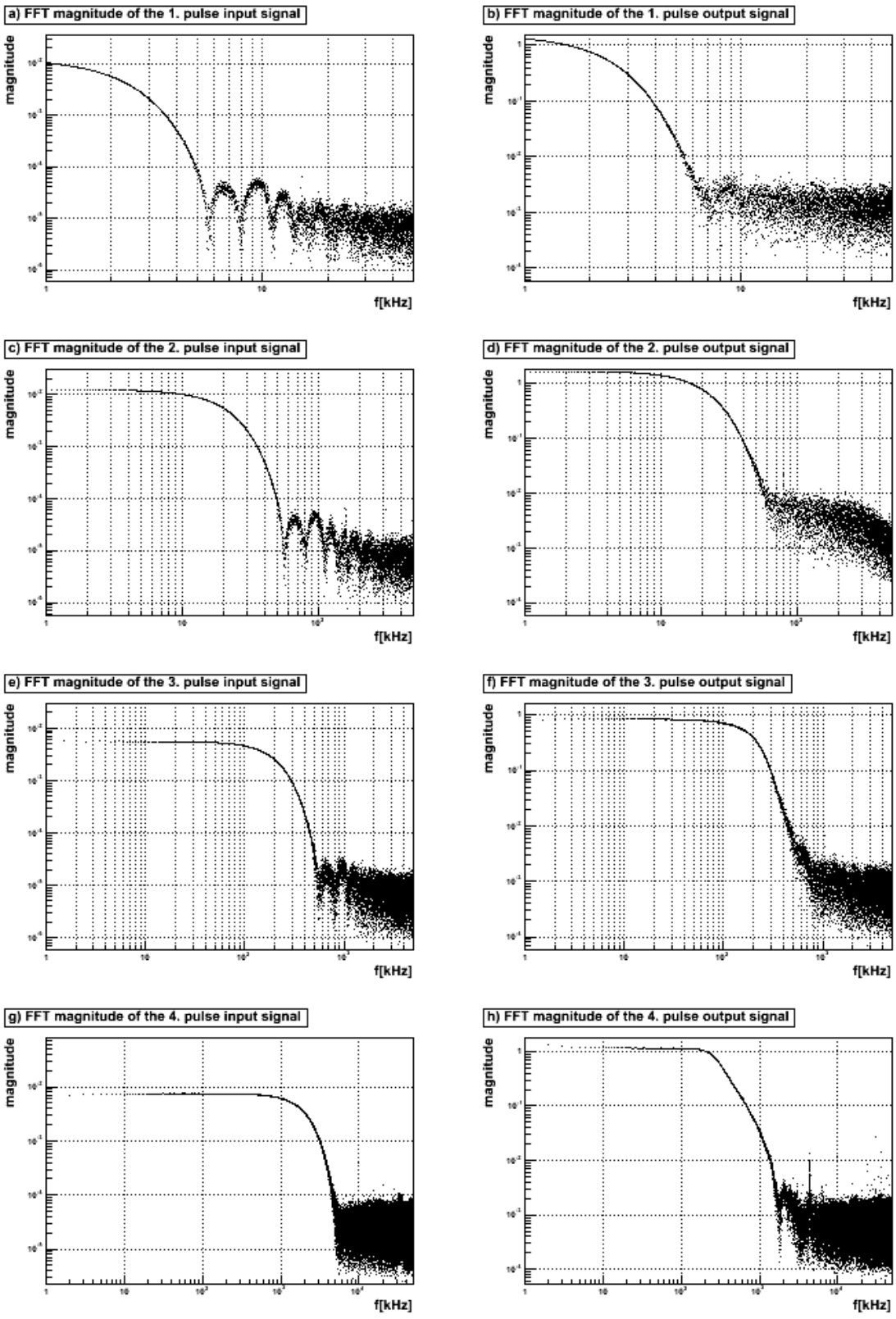

Figure 3.17: FFTW the magnitude of the input and output signal double logarithmically plotted

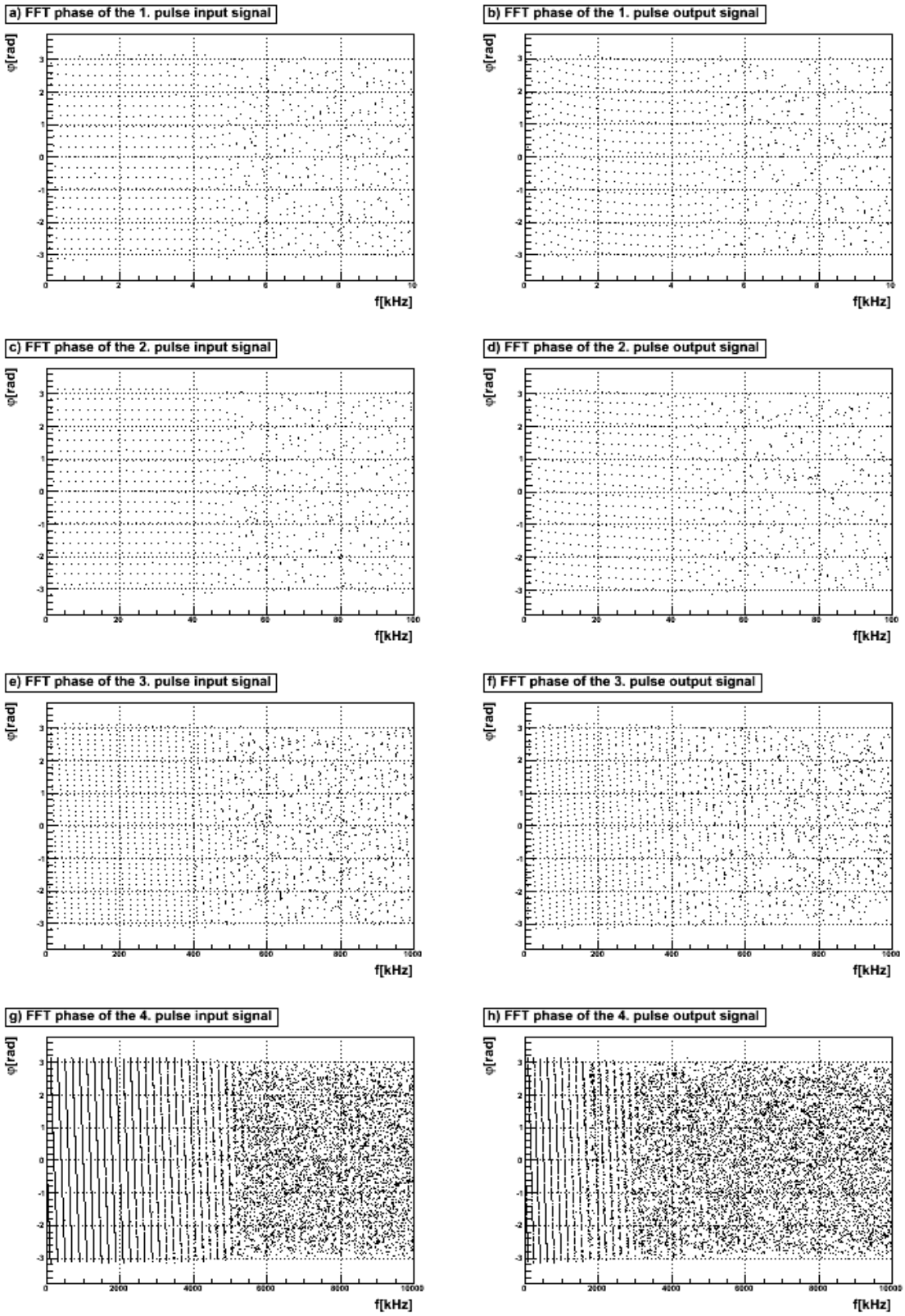

Figure 3.18: FFTW the phase of the input and output signal

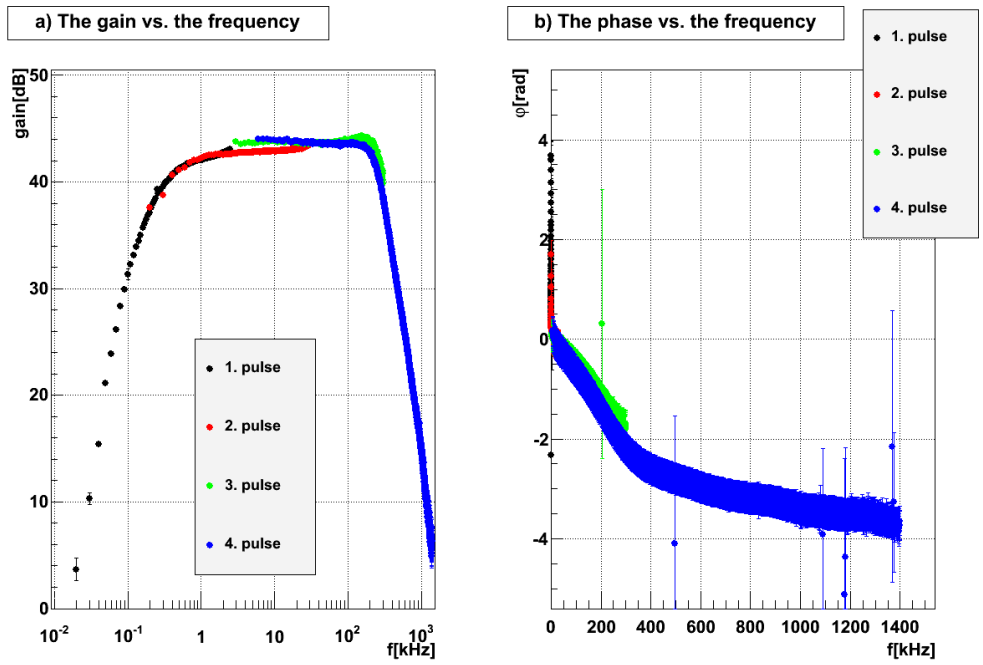

Figure 3.19: The gain (*left*) and phase (*right*) of the transfer function determined by the four Gaussian signals as a function of the frequency.

100 averaged signals for each spectra. The magnitude of the FFTW is given in fig. 3.17 and the phase in fig. 3.18, respectively.
On closer inspection of the magnitude (especially in fig. 3.17a,c) the side maxima resulting from the sinc function can be identified, demonstrated in eq. 3.19. But in other spectra (cf fig. 3.17f,g) the side maxima cannot identified, because they disappear in background noise. So to ensure that no side effects of the sinc function or the background noise disturb further calculations, each spectrum of the magnitude is cut off after its decrease and just before the side maxima occur, similar to the master amplifier. Looking at fig. 3.18, the phase seems to be quite homogenously distributed. Similar for the master amplifier, the phase is statistically distributed after the frequency where the side maxima occur. This is caused by the fluctuations and therefore, the spectra of the phase get the same cut off as the magnitude. Even if the absolute phase seems to be homogenously distributed for both the master and the pre-amplifier, the difference between the input and output phases is essential for the signal reconstruction. So it has to be taken into account for the further analysis.
As mentioned for the master amplifier, the spectra of the FFTW magnitude are divided and those of the phase are subtracted and smoothed as described in eq. 3.13. The result is shown in fig. 3.19. As the figure shows depending on the width of a single pulse, a different part of the frequency spectrum can be better approximated. Care had been taken that there had been an overlap of the single parts to get an continuous distribution by averaging of the single parts. Fig. 3.19 also emphasize the difficulty of aligning the single part to each other because of the slight, but obvious discrepancies.

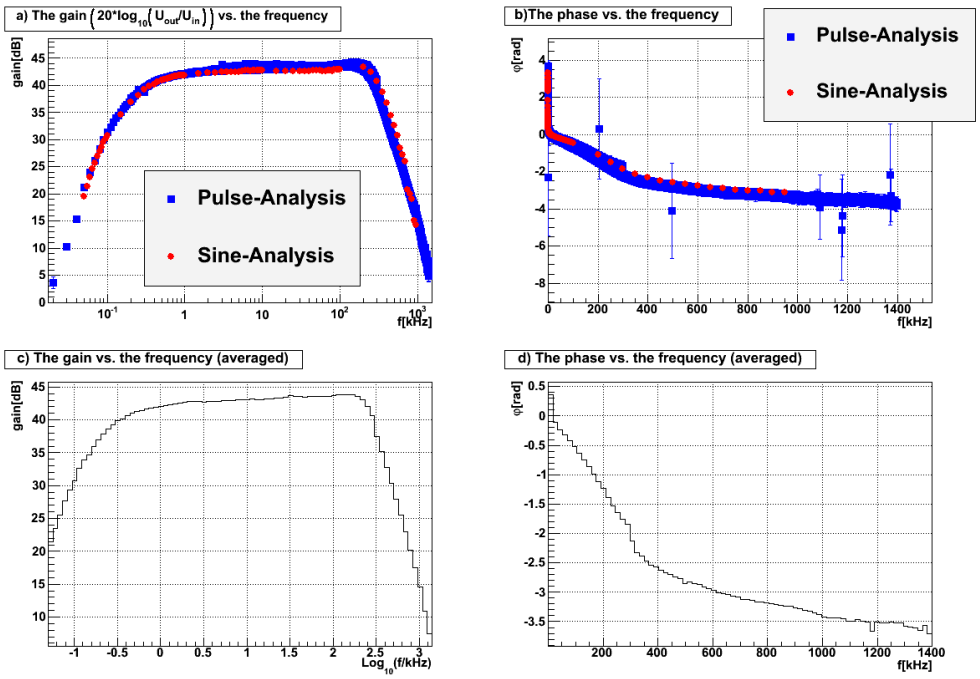

Figure 3.20: The upper pictures shows the experimentally found transfer function of the both used characterizations. The pictures below shows the average of both methods via a histogram respectively

Finally, the data of both characterizations, Sine- and Pulse-Analysis, has to be merged and approximated by an analytic function.
Fig. 3.20a,b shows the result of both methods. Within the accuracy of the measurement, they describe the same distribution. So it can be assumed that there are no side effects which do not originate from the amplifier itself. To minimize the fluctuations caused by the measurement inaccuracy the data of both methods are smoothed; the result is shown in fig 3.20c for the gain and in fig 3.20d for the phase.
According to the schematics of the pre-amplifier shown in fig. 3.21, the first part of the amplifier will be approximated by a Sallen-Key low pass filter whereas the rest will be described by two 1st order high passes, a 1st order low pass and a linear phase term. As indicated in eq. 3.8, the whole transfer function is given by the cascade of analytic functions and each of these functions is generated by the found filter, as mentioned for the master amplifier. The gain of the transfer function is calculated from the magnitudes of impedance ratio and therefore given by

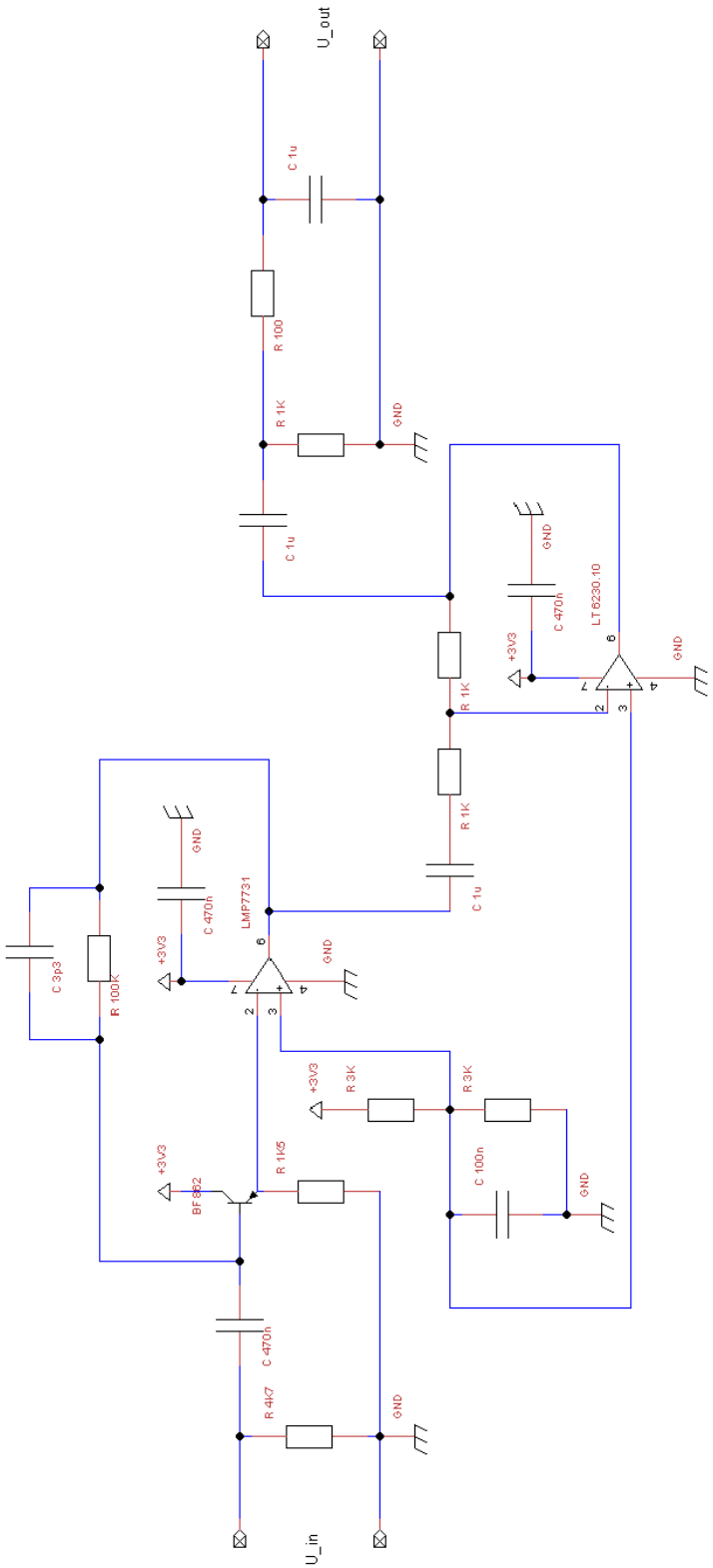

Figure 3.21: The schematic of the pre-amplifier.

$$A = A_{\text{tot}} \cdot \prod_{i=1}^{1} \left[A_i^{\text{sallen}}\right] \cdot \prod_{j=1}^{2} \left[A_j^{\text{high}}\right] \cdot \prod_{k=1}^{1} \left[A_k^{\text{low}}\right] \tag{3.23a}$$

$$A_i^{\text{sallen}} = \frac{1}{\sqrt{\left(1 - \left(f/f_i^{\text{sallen}}\right)^2\right)^2 + \delta_i^{\text{sallen}} \cdot \left(f/f_i^{\text{sallen}}\right)^2}} \quad (\textit{Sallen-Key low pass}) \tag{3.23b}$$

$$A_j^{\text{high}} = \left(\frac{f/f_j^{\text{high}}}{\sqrt{1 + \left(f/f_j^{\text{high}}\right)^2}}\right)^{n_j^{\text{high}}} \quad (\textit{nth order high pass}) \tag{3.23c}$$

$$A_k^{\text{low}} = \left(\frac{1}{\sqrt{1 + \left(f/f_k^{\text{low}}\right)^2}}\right)^{n_k^{\text{low}}} \quad (\textit{nth order low pass}) \tag{3.23d}$$

The phase of transfer function is calculated from the phase of complex resistance ratio and it is given by

$$\varphi = \varphi_{\text{tot}} + \sum_{i=1}^{1} \left[\varphi_i^{\text{sallen}}\right] + \sum_{j=1}^{2} \left[\varphi_j^{\text{high}}\right] + \sum_{k=1}^{1} \left[\varphi_k^{\text{low}}\right] + \varphi^{\text{lin}} \tag{3.24a}$$

$$\varphi_i^{\text{sallen}} = \arctan\left(\frac{\sqrt{\delta_i^{\text{sallen}}} \cdot f/f_i^{\text{sallen}}}{\left(f/f_i^{\text{sallen}}\right)^2 - 1}\right) \quad (\textit{Sallen-Key low pass}) \tag{3.24b}$$

$$\varphi_j^{\text{high}} = n_j^{\text{high}} \cdot \left(\pi/2 - \arctan\left(f/f_j^{\text{high}}\right)\right) \quad (\textit{nth order high pass}) \tag{3.24c}$$

$$\varphi_k^{\text{low}} = -n_k^{\text{low}} \cdot \arctan\left(f/f_k^{\text{low}}\right) \quad (\textit{nth order low pass}) \tag{3.24d}$$

$$\varphi^{\text{lin}} = -2\pi \cdot \delta^{\text{lin}} \cdot f \quad (\textit{linear phase}) \tag{3.24e}$$

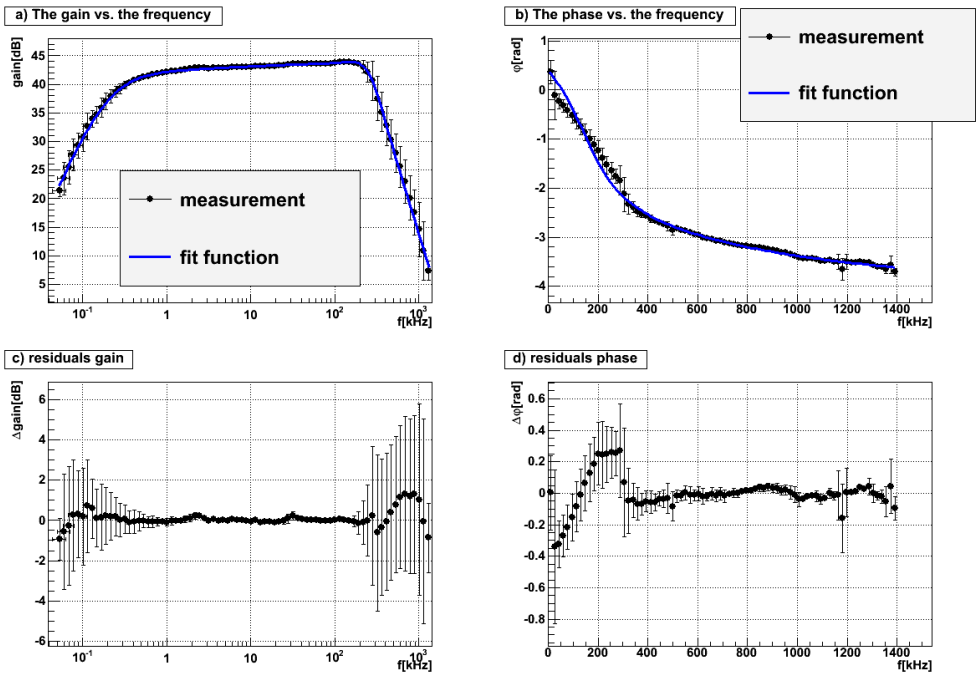

Figure 3.22: In the upper pictures the averaged transfer function (*black curve*) and its fit function (*blue line*) are shown. The pictures below shows the linear residuals respectively and the errors are taken directly from the data.

According to eq. 3.23 and 3.24, there are 9 free parameters for the gain and 10 free parameters for the phase to adjust to. The initial parameter values are generated by the impedances of the schematics given in fig. 3.21. Similar to the master amplifier, the functions for the gain and the phase do not generate the exact transfer function. Thus and because of the measurement inaccuracy, it can be expected that the fit parameters for the gain and the phase are not identical, although they should be.
The decision whether to approximate the data by a fit is based on the linear residuals between the fit function and the data. Therefore, the parameter values from the previous fit are used as initial values for the current fit. This has been iterated until the fit could converged.
The final result for the gain is given in fig 3.22a and for the phase in fig. 3.22b. The linear residuals are given in fig. 3.22c,d respectively. Within the accuracy of the measurement and according to the residuals, it is assumed that the fit function describes the same distribution as the measurement data.
The parameter values for the fit are given in tab. 3.2. The discrepancies ($\approx 2\sigma$) for the Sallen-Key and low pass filter can be explained by the measurement inaccuracy, but not for those of the high pass filters. Actually, this could be caused by the analytic found function for the gain and the phase not describing the exact transfer function for the lower frequencies. Nevertheless, this solutions was applied because it yields a good approximation of the measurement data and finding a more exact analytic function would have been too time intensive.

total gain:	1.558e+002 ± 1.052e+001	
total phase:	-2.717e+000 ± 0.000e+000	
1. high pass	frequency f_1^{high} [kHz]	order n_1^{high}
gain	1.963e-001 ± 2.825e-002	1.650e+000 ± 2.775e-001
phase	4.210e-006 ± 5.705e-006	6.498e-005 ± 4.899e-005
2. high pass	frequency f_2^{high} [kHz]	order n_2^{high}
gain	1.226e+002 ± 8.332e+001	3.453e-002 ± 2.418e-003
phase	7.532e-006 ± 8.678e-006	2.213e-005 ± 2.549e-005
1. low pass	frequency f_1^{low} [kHz]	shift δ_1^{low}
gain	1.228e+002 ± 3.532e+001	3.356e-001 ± 1.073e-001
phase	8.897e+002 ± 9.748e+001	1.056e+000 ± 4.944e-002
1. Sallen-Key high pass	frequency f_1^{sallen} [kHz]	shift δ_1^{sallen}
gain	2.498e+002 ± 1.449e+001	8.673e-001 ± 9.679e-002
phase	1.897e+002 ± 6.957e+000	1.393e+000 ± 2.268e-001
linear phase[ms]:	3.486e-008 ± 1.618e-008	

Table 3.2: The final parameter values for the functions described in eq. 3.23 and 3.24

3.2.3 Pre-amplifier (first prototype)

This subsection will illustrate an example of the importance of having a consistent check to find out whether some effects disturb the measurement. For this reason, the analysis of the first pre-amplifier prototype are discussed. It has the identical schematics as shown in fig. 3.21 and it is characterized by sine and pulse signals, just as for the master and pre-amplifier in the previous sections.
The results of both characterizations are shown in fig. 3.23. Two things are to be pointed out. First, there is a kind of anti-resonance or dip at ≈ 400kHz in the gain distribution and ≈ 500kHz in the phase distribution. Second, both characterizations seem to differ from each other at frequencies higher than 50kHz. Because of this discrepancies it can be assumed that some effects disturbed the measurement. Primarily, no decision can be made which of the two yield the correct distribution, yet.
To find the cause for these two feature, the first thing to be scrutinized are the incoming and outgoing pulse signals. Therefore, the input signals are parameterized by a Gaussian distribution, as seen in fig. 3.24, and the output signals are parameterized by a Gaussian distribution for the first peak and a Landau distribution for the second one, shown in fig. 3.25. As it can be seen, the Landau distribution is a good approximation of the measured distribution. However, this is not an anticipate impulse response. One would expect some version of a decaying oscillation, but the Landau distribution seems to completely interfere with this.
A possible explanation could be a reflection or an overlap of several reflections between the oscilloscope and the amplifier. For a more detailed analysis, the prototype should be disassembled, but this was not possible. Thus it was rebuilt with identical schematics

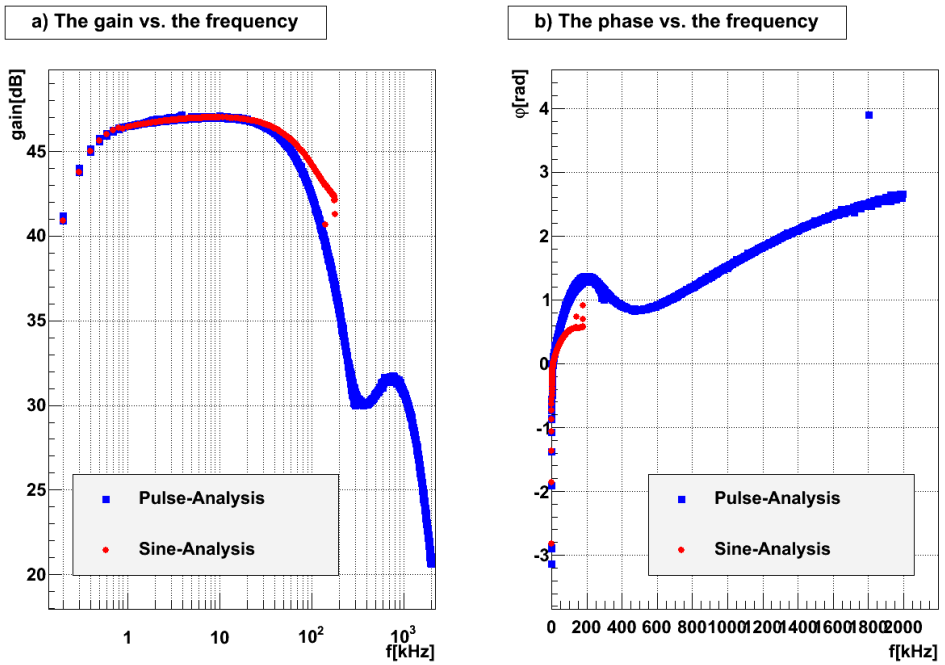

Figure 3.23: The experimentally found transfer function of the both characterizations used.

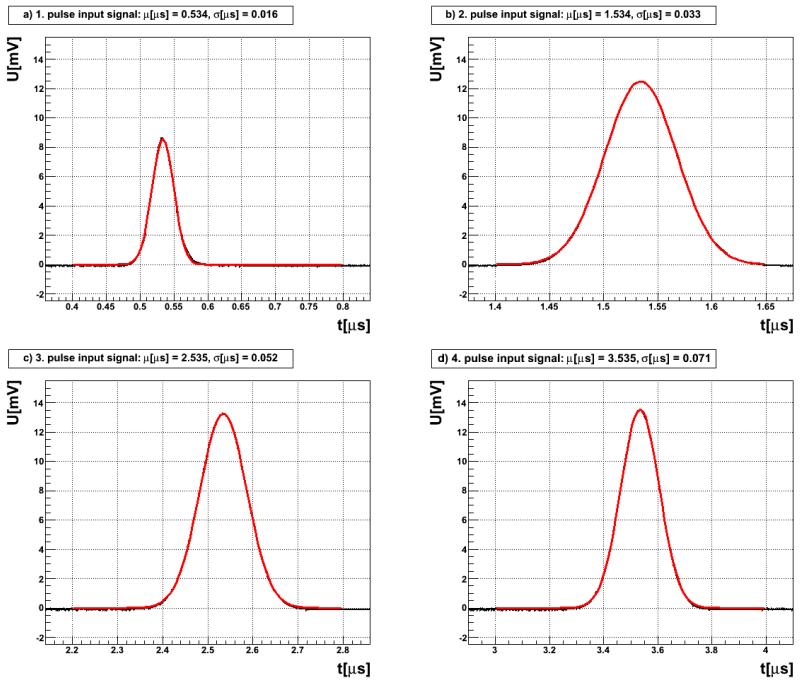

Figure 3.24: The four input Gaussian pulses (*black*) of variant width. The pulses are already averaged as described in eq. 3.18. The *red* line is the approximation by the Gaussian fit.

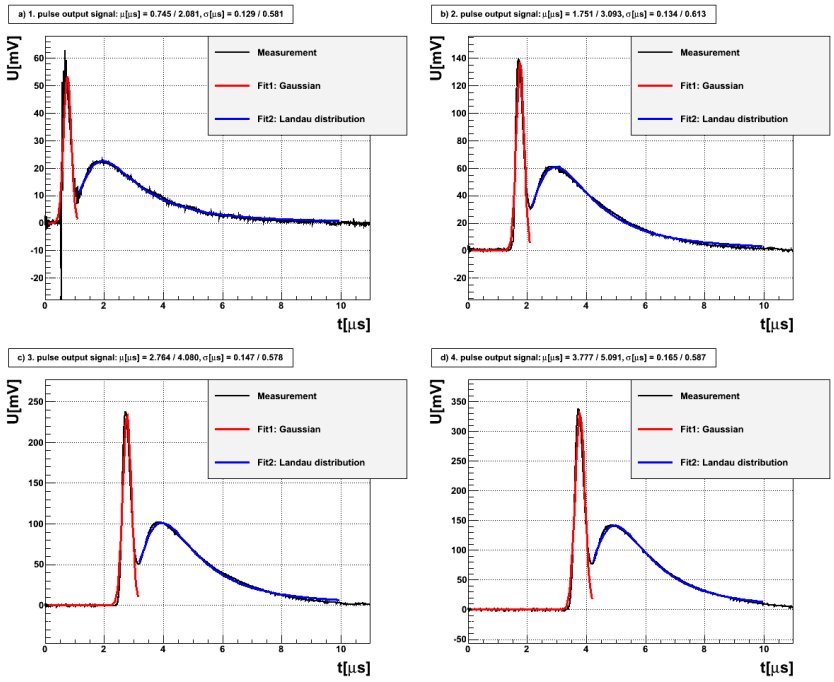

Figure 3.25: The four response signals of the input Gaussian pulses. The response signals are already averaged as described in eq. 3.18

to find out whether this was a feature of the circuit. This was not the case, as seen in sec.3.2.2 and it is assumed that the failure has been caused by a damage of the prototype itself.

3.3 Results

In the following, the input signal is reconstructed by a given output signal, and the output signal by a given input signal, respectively, through the analytic transfer functions ascertained in the previous section.
Since a convolution is difficult to calculate numerically, the frequency spectrum of the given signal generated by the FFTW is scaled by the transfer function in order to arrive at the frequency spectrum of the reconstructed signal.
In the first step, the signals for the master and pre-amplifier are separately reconstructed. For this purpose, the same four pulse signals which were applied for the respective Pulse-Analysis of each amplifier are used for the reconstruction.
After that, the signals of the complete acoustic sensor array, consisting of the piezo[7], the pre- and the master amplifier, are reconstructed.

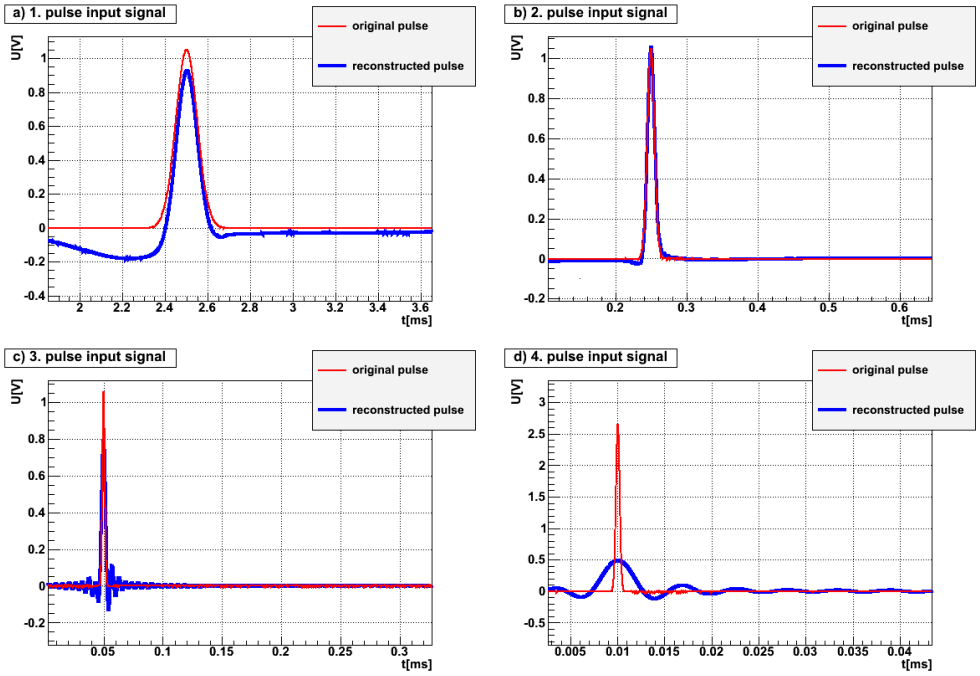

Figure 3.26: The comparison between the original input signal and the reconstructed one for the master amplifier

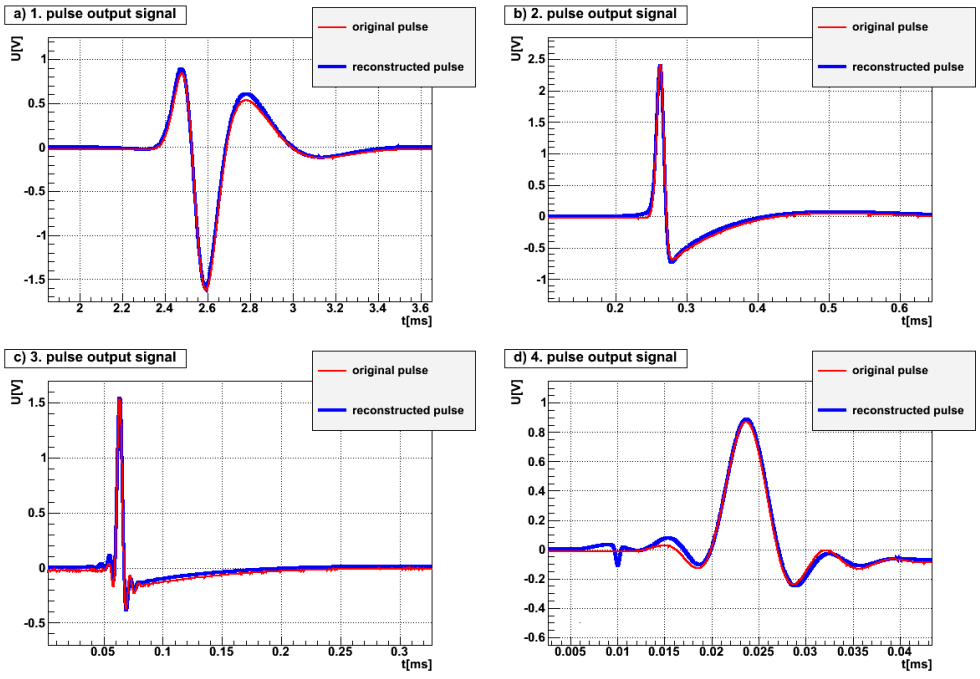

Figure 3.27: The comparison between the original output signal and the reconstructed one for the master amplifier

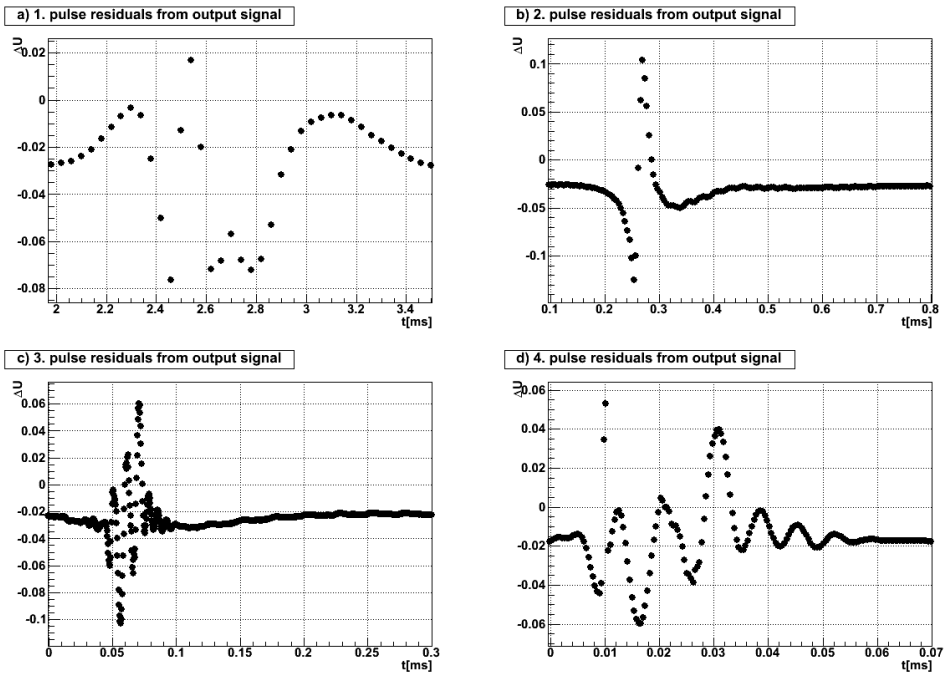

Figure 3.28: The linear residuals between the original output signal and the reconstructed one for the master amplifier

3.3.1 Signal reconstruction of the master amplifier

Fig. 3.26 shows the reconstruction of the input signal, which could not be well reconstructed. The reason for this is that on the one hand the amplifiers just let frequencies in a designated interval pass through, while the lower and higher ones are heavily suppressed, resulting in an information loss for the output signal for these frequencies. And on the other hand, while the transfer function had to suppress these frequencies for the output signal, the inverse transfer function has to intensify these frequencies, but in fact it only intensified the background noise of the amplifier, disturbing the reconstruction. Taken all this into account, it is not possible to reconstruct the input signal by just scaling the frequency spectrum of the output signal with the inverse transfer function.
As it can be seen in fig. 3.27, the original and reconstructed output signal describe qualitatively almost an identical distribution, meaning that it could be reconstructed very well. The linear residuals, shown in fig. 3.28, are examined in order to receive quantitative information on the discrepancy between the original and the reconstructed signal. As it can be gathered, there is an constant offset of approximately -25mV, but this is no great cause for concern, because a constant offset just shifts the distribution along the axis. More precise information can be obtained from the standard deviation of the residuals. The calculation yields a standard deviation, averaged through the four signals, of 5mV and this is absolutely within the same order of magnitude as the intrinsic noise of the amplifier of about 10mV.

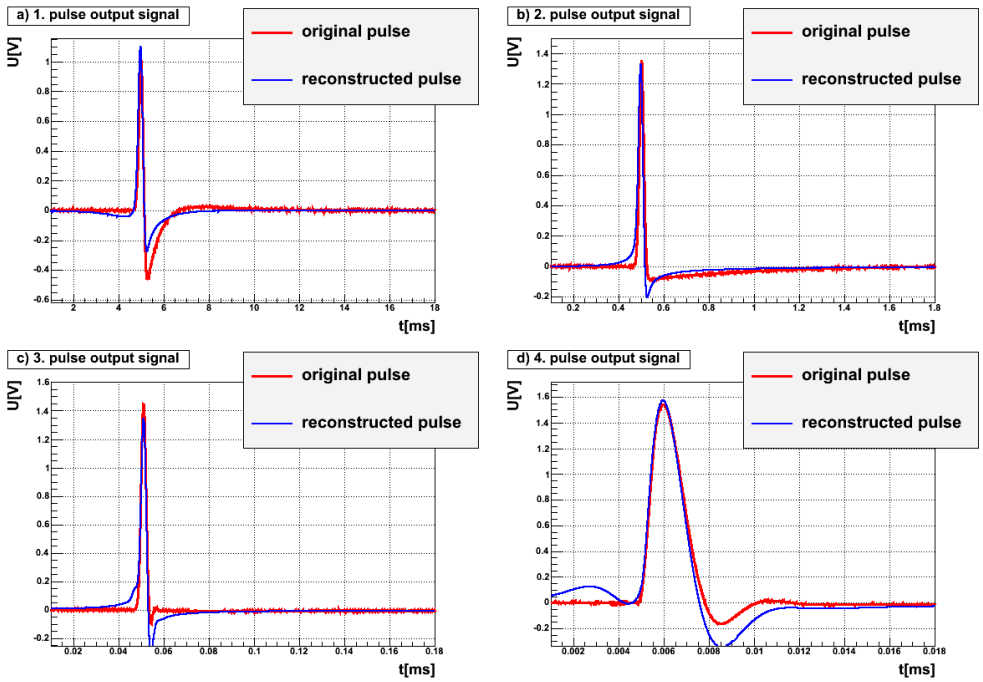

Figure 3.29: The comparison between the original output signal and the reconstructed one for the pre-amplifier

3.3.2 Signal reconstruction of the pre-amplifier

First of all, it should be noted that it was not possible to reconstruct the input signal for the pre-amplifier. Owing to the well-ordered construction of the second prototype of the pre-amplifier, its background noise was considerably increased. So the main focus of the reconstruction is on the output signal.
Looking at fig. 3.29, the original and reconstructed output signal describes qualitatively an similar distribution. But to get a quantitative information of the discrepancy between the original and the reconstructed signal, the linear residuals, shown in fig. 3.30 are scrutinized. The standard deviation of the residuals is calculated and averaged through the four signals, giving a standard deviation of 15mV and this is absolutely within the same order of magnitude as the intrinsic noise of the amplifier of about 50mV.

3.3.3 Signal reconstruction of the whole analog acoustical Part

In this last subsection, the signal reconstruction of the whole analog acoustical part is investigated, i.e. the output signal of the cascade of the piezo, pre-amplifier and master amplifier is reconstructed. To achieve this, the piezo is excited by an electrical signal and its response signal is sent directly to the pre-amplifier as the input signal. Note that because of the high gain of the pre-amplifier, the same frequency independent voltage divider as for the characterization in sec. 3.2.2 is used upstream of it, but this has been taken into account for the calculation of the reconstruction. The response signal of the pre-amplifier is used as input signal of the master amplifier. Finally, the response signal

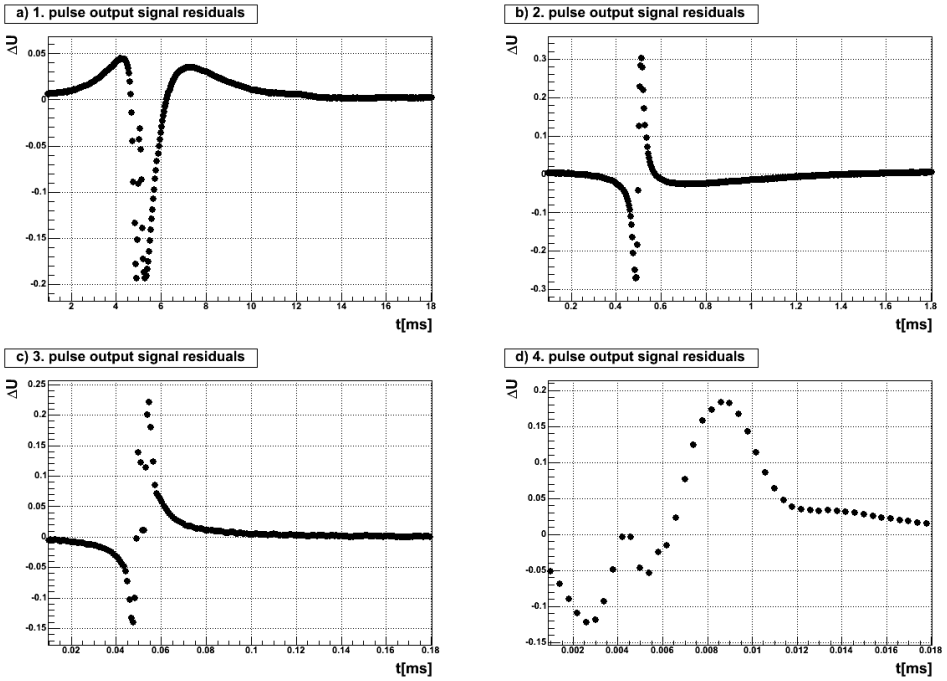

Figure 3.30: The linear residuals between the original output signal and the reconstructed one for the pre-amplifier

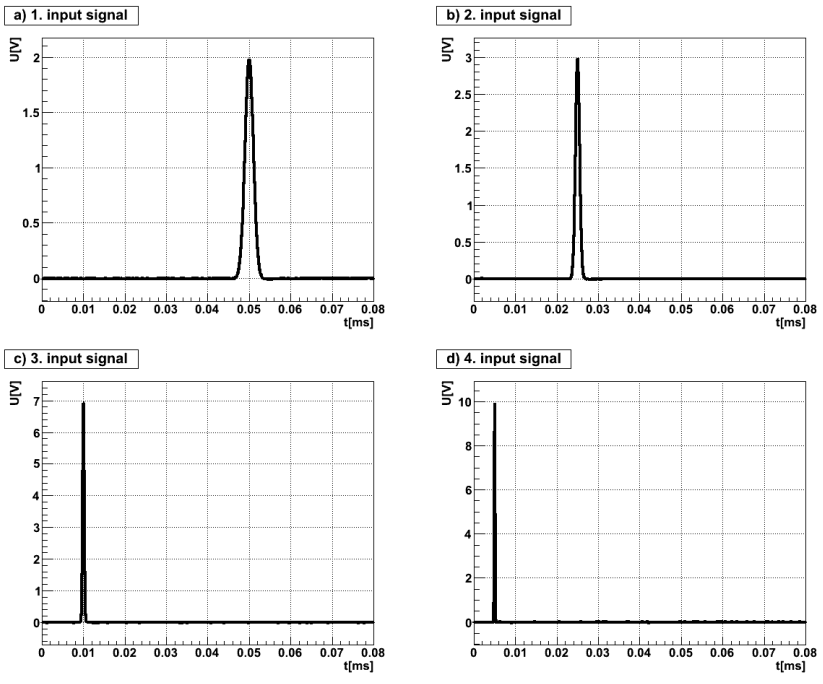

Figure 3.31: The four input signals used for the reconstruction of the output signal of the whole analog acoustical part

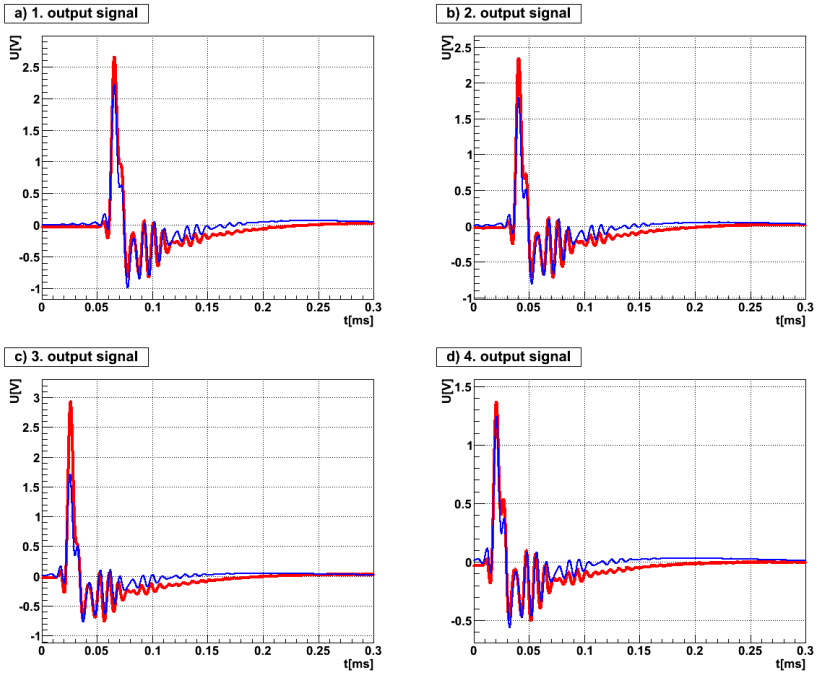

Figure 3.32: The four original (*red*) and reconstructed (*blue*) output signal of the whole acoustical part

of the master amplifier is stored as the final output signal. It is assumed that these are the only interactions between the amplifiers and the piezo. The analytic transfer function of the piezo is taken from S. Pickel[7].
A broad frequency spectrum has to be involved for the reconstruction to achieve a significant description of the reconstruction. Therefore, four Gaussian pulses of different widths (see fig. 3.31) are used as input signals of the cascade, because a small Gaussian distribution approximate a δ-pulse, which is flat in the frequency domain, as described in sec. 3.1.3.
As it can be seen in fig. 3.32, the original and reconstructed signal are in good agreement with each other, with only minimal discrepancies between both signals. The cause of these discrepancies could possibly arise when the output couples to the amplifier. To verify whether this is the case, the first two resonances of the piezo transfer function are adjusted to the spectra of the four Gaussian pulses.

Only the first two resonances' parameters of the complete transfer function are adjusted by a fit and all other parameters are fixed. The resulting transfer function is given in fig. 3.33: It approximates the distribution well for frequencies higher than 50kHz. But for the lower frequencies the transfer function is too low, probably caused by the transfer functions of the pre- and the master amplifier. It seems they are too low in this part and thus the multiplication becomes even lower. To see how high the resonances have exactly changed, the adjusted parameters are given in tab. 3.3. All parameters except for two have just slightly changed by a factor two or lower. Thus the reconstructed signal is also

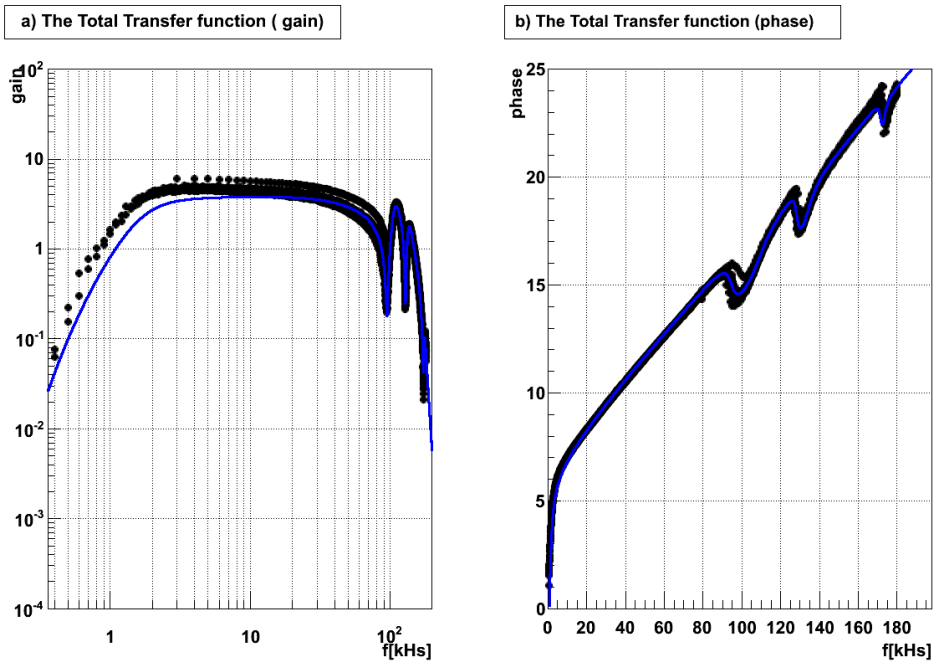

Figure 3.33: The adaption of the piezo resonances to the whole acoustical part.

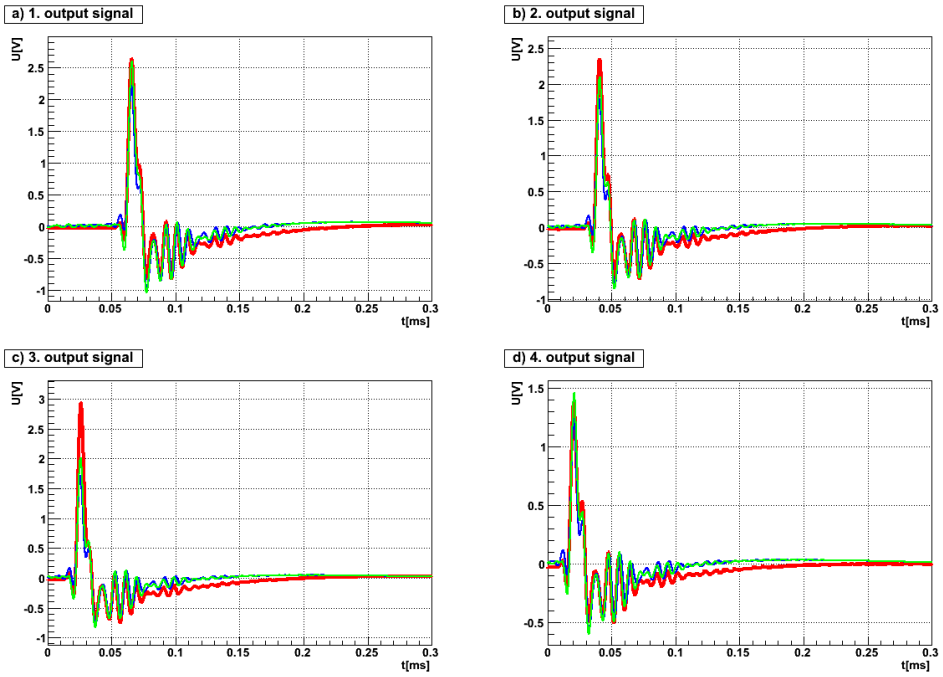

Figure 3.34: The four original (*red*) and reconstructed (*blue*) output signal of the whole acoustical part. The *green* curve describes the reconstruction with adjusted transfer function.

Comparison of the new and old parameters for the gain			
Type	old value	new value	ratio (new/old)
General C[mF]	$2.50606 \cdot 10^{-07}$	$1.42531 \cdot 10^{-07}$	0.568746
1. L[mH]:	27.1526	39.3828	1.45043
1. C[mF]:	$1.10743 \cdot 10^{-07}$	$7.19784 \cdot 10^{-08}$	0.649959
1. R[Ω]:	69.587	526.586	7.56731
2. L[mH]:	82.621	98.1793	1.18831
2. C[mF]:	$1.9221 \cdot 10^{-08}$	$1.5776 \cdot 10^{-08}$	0.820767
2. R[Ω]:	1959.33	1021.45	0.521325
Comparison of the new and old parameters for the phase			
Type	old value	new value	ratio (new/old)
General C[mF]	$2.22285 \cdot 10^{-07}$	$2.8972 \cdot 10^{-07}$	1.30337
1. L[mH]:	31.3086	22.404	0.715587
1. C[mF]:	$9.60256 \cdot 10^{-08}$	$1.26344 \cdot 10^{-07}$	1.31574
1. R[Ω]:	209.483	736.26	3.51465
2. L[mH]:	93.7185	74.7641	0.797752
2. C[mF]:	$1.69513 \cdot 10^{-08}$	$2.05754 \cdot 10^{-08}$	1.21379
2. R[Ω]:	2305.3	1126.87	0.488819

Table 3.3: The comparison of the old parameter values of the first two piezo resonances (described in [7]) with newly generated values

slightly changed, as fig. 3.34 shows. According to the data, the resonances of the piezo can be treated as unchanged.
Further examples of reconstructed signals are given in fig. 3.35 and fig. 3.36. For these signals the adjusted transfer function was applied. It can be seen that most signals could be well reconstructed. Note that these are not the typical signals to search for, they merely served as a test what was possible.

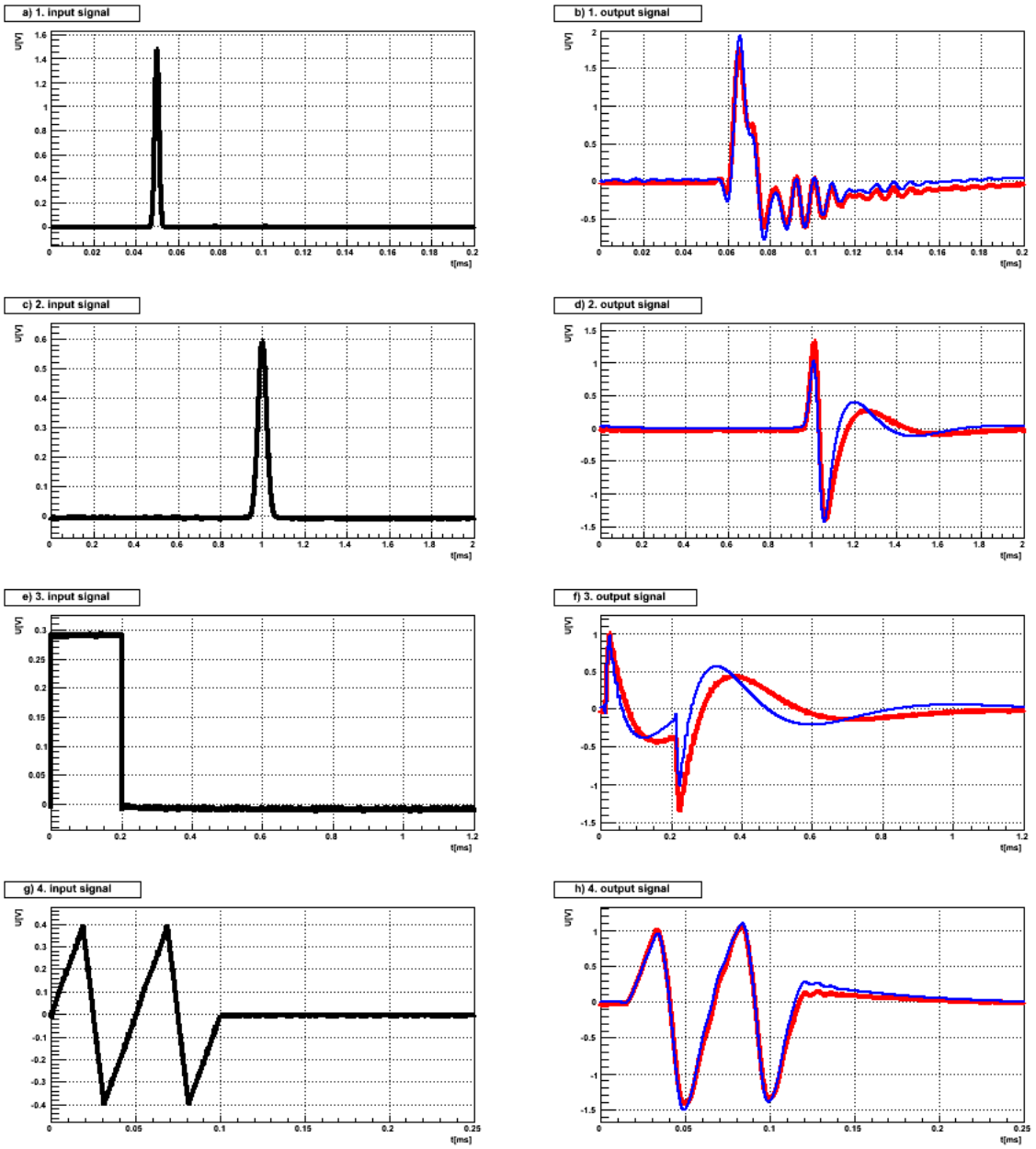

Figure 3.35: The first four examples of reconstructed signals by using the adjusted transfer function. The *right* pictures show the input signal and the respective *left* pictures show the original (*red*) and the reconstructed (*blue*) output signals

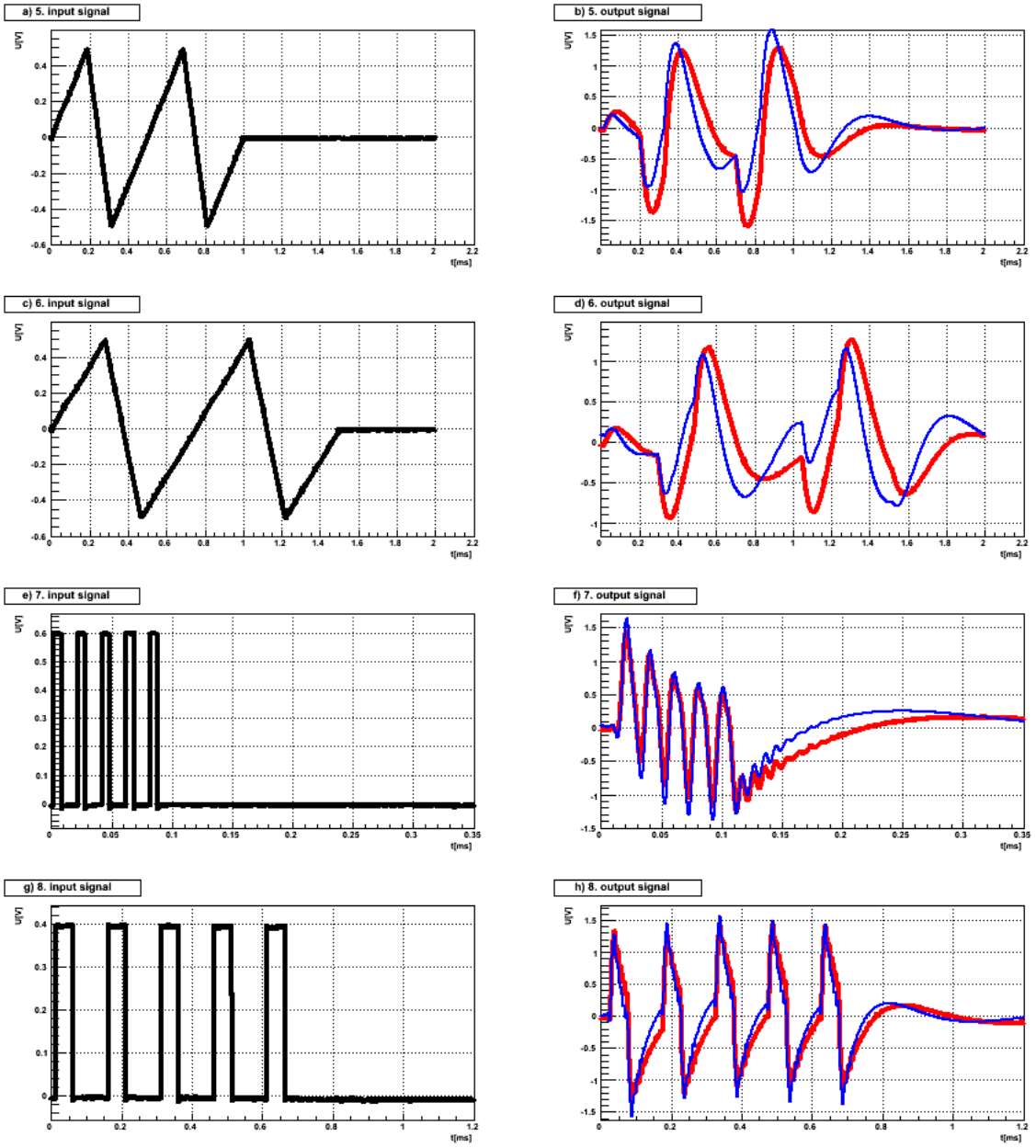

Figure 3.36: The latter four examples of reconstructed signals by using the adjusted transfer function. The *right* pictures show the input signal and the respective *left* pictures show the original (*red*) and the reconstructed (*blue*) output signals

4 Analysis for the positioning with the acoustical sensor array

Goal of this chapter is a feasibility check of the positioning with the acoustical sensor array, characterized in the previous section. For this purpose, a detailed understanding of the sensor properties is required, after it is installed in the optical module.
As mentioned before, the position of an optical module is determined by triangulation. The distances required for the triangulation, are obtained from the convolution of the travel time with the sea sound profile. As a first step, the accuracy of this travel time and response of the integrated array through an acoustical input are studied. In the next step, the possibility of the pinger detection is investigated according to their signal strength as compared to the background noise.

4.1 Analysis for Travel Time Measurement

Regardless of other uncertainties, the sole focus lies on the uncertainty caused by sensor array for the study of the travel time accuracy. Furthermore, the determination of the accuracy is based on theoretical calculations without any measurements.
After the integration of the sensor array into the optical module at the National Institute for Subatomic Physics (NIKHEF) in Amsterdam, the subsequent measurements were done by Robert Lahmann from the Friedrich-Alexander University of Erlangen in May 2012.

4.1.1 Time Delay in the Sensor Array

The delay, arising as the signals pass through the sensor array, has to be taken into account for the travel time measurement. This delay could come across as a shift in time of signal, but the sensor array changes the shape of the input signal, leading to a loss of the information of a precise arrival time point. The effect is that there is no exact time point for the arrival of the output signal.
The transformation of time shifted signal into the Fourier space results in an additional linear phase term as opposed to the Fourier transformation of the original signal, i.e.:

$$\mathcal{F}\left[U(t-t_0)\right](\omega) = \mathcal{F}\left[U(t)\right](\omega) \cdot \exp\left(-it_0\omega\right) \tag{4.1}$$

As a consequence, the time shift is determined by the slope of the linear phase term. Therefore, the linear phase terms of the amplifiers should give at least the time shift's

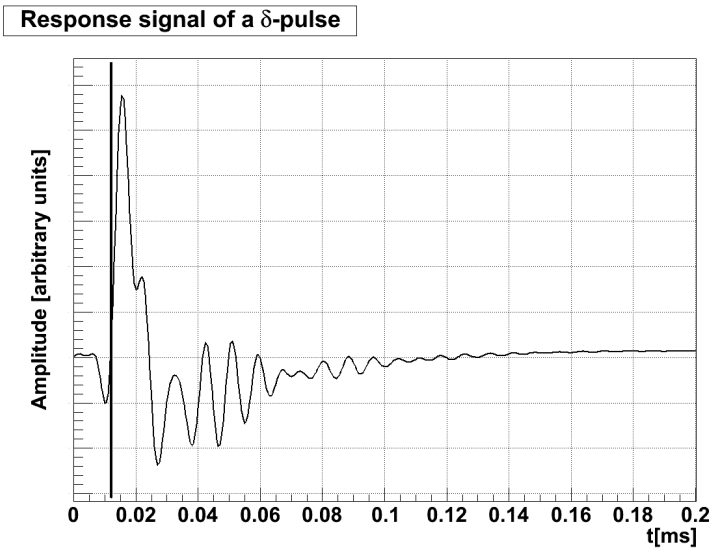

Figure 4.1: *Thin line*: the expected response signal of a input δ-pulse calculated via the transfer function for the sensor array; *thick line* the time delay determined by the linear phase terms of the amplifiers

order of magnitude. But to ensure that this is the case, some kind of reference signal is required.
A δ-pulse has, on the one hand, no temporal extent and thus a precise time point, and on the other, a broad frequency spectrum which will be taken into account. The resulting response signal is calculated by the Fourier transformation of the complete sensor array's transfer function, i.e.

$$U_{\text{out}}(t) = \mathcal{F}^{-1}\left[\hat{H}(\omega)\right](t) \tag{4.2}$$

The subsequent output signal is shown in fig. 4.1 together with the time shift calculated via the slope of the linear phases. This time shift is close to the first zero-crossing of the output signal, thus the shift can be assumed to yield the order of the magnitude for the time delay of the sensor array.
Clarifying the significance of the delay, the difference in the positioning of a optical module is calculated, the velocity of sound in water is assumed to be constant at about $1500\frac{m}{s}$ and time delay is set to 12μs. From this it follows:

$$\Delta d = v_s \cdot \Delta t \approx 1.8\text{cm} \tag{4.3}$$

This is within the same order of magnitude as the ANTARES positioning accuracy of about 1cm [3, 1]. Thus, it has to be taken into account for travel time measurement, but it can be treated as a systematic error.

4.1.2 First "Dry Run" of the Sensor Array

As the next step, the acoustical sensor array were integrated into the optical module. The complete module is seen in fig. 4.2(a). The big yellow golden circles are the PMTs,

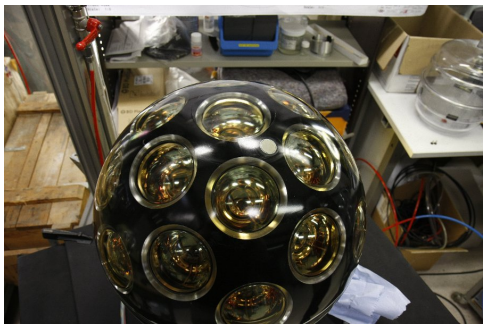

(a) The complete optical module

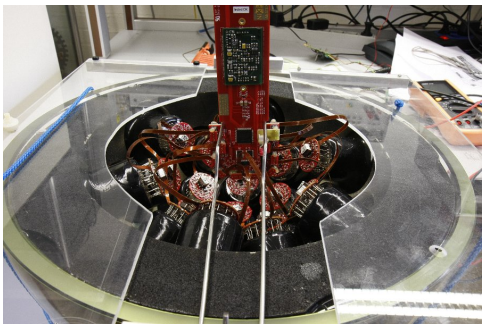

(b) With a view to the acoustic master amplifier (green circuit board)

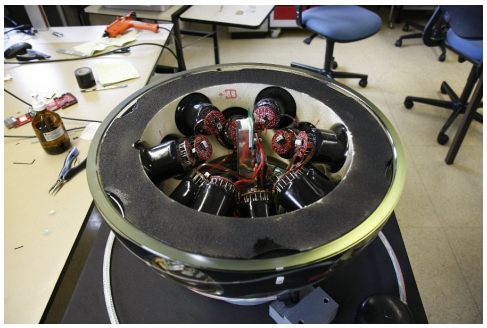

(c) The bottom half of the module with a look inside

(d) Detailed top view inside the module

Figure 4.2: Pictures of a optical module for KM3NeT, holding the PMTs and the acoustic sensor array. Pictures are taken from [11]

while the little beige circle is the piezo ceramic of the acoustical sensor. Fig. 4.2(b) provides a view inside the upper half of the optical module with a view to the master amplifier of the acoustical sensor array.
Due to technical restriction, an implementation of a measurement in a water tank has not been possible so far. Consequently, an attempt was made to achieve the measurement with the air as the surrounding medium, in a manner of speaking as a dry run. For this reason, an emitter was tied onto the exterior of the module in order to fix the emitter at a precise position in such a manner to achieve the maximum output signal strength.

Two different output signals are seen exemplarily in fig. 4.3. Neither yields a clear response signal. For the sine signal in fig. 4.3(a), a periodic behavior is observable, but with more than one frequency. But the response of the Gaussian, see fig. 4.3(b), is more comparable to a sine signal than to a Gaussian. Thus, massive disturbances seems to interfered in the measurement.
There are some possible reasons which would create these disturbances:

- The emitter was positioned close to the acoustical sensor array, leading to near-field-effects which are not perfectly known for the emitter.

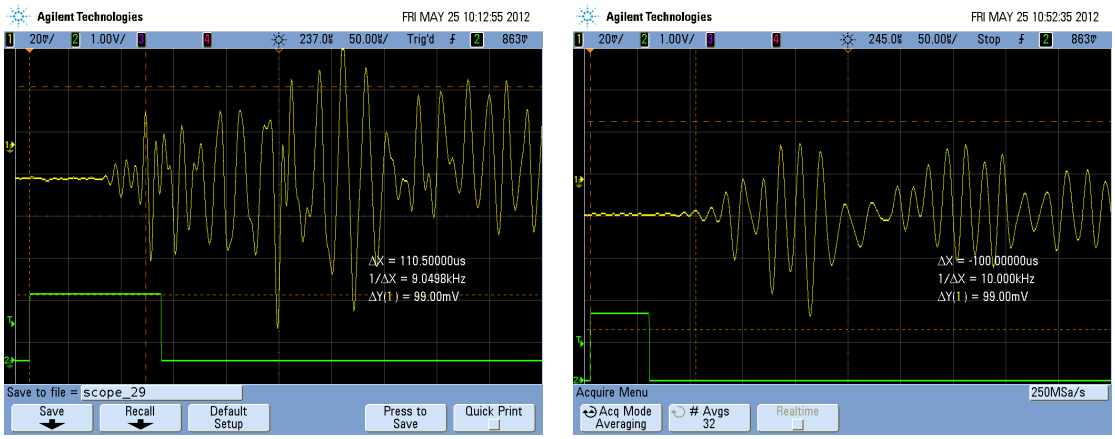

(a) Response of a 40kHz sine input signal

(b) Response of a Gaussian input signal

Figure 4.3: Output signals of the sensor array generated by an acoustical input signal from a emitter, which was fixed outside the optical module.

- A further consequence, caused by the short distances to the sensor, is the increasing of reflections inside the surrounding glass sphere, seen in fig. 4.2(c) and fig. 4.2(d), of the optical module relating to the geometrical factor.

- Additional reflections caused by the coupling between the emitter and the optical module

Because of a significant greater acoustical absorption of air as compared to water, a greater distance between emitter and sensor could lead to a significant loss of the signal's strength. Thus, it seems to be necessary to conduct the measurement in water in order to achieve clear response signals.

4.2 Theoretical Detection Possibility of the Pinger Signal

For the distinction between the actual pinger signal and the background noise, the amplitude of the pinger signal is increased in order to determine the value at which the pinger signal is indistinguishable from the background noise. Therefore, a theoretical pinger signal is calculated and merged with real noise data.
The noise data is taken from the integrated acoustical sensor devices, seen in fig. 4.2. There are two different measurement. The first is a measurement without active PMTs, while the PMTs were activated for the second measurement. Each measurement is studied with and without a digital band-pass-filter, generating four different sets of noise data.
The complete analysis and all plots are generated with ROOT [6].

Figure 4.4: The basic shape of the pinger signal

4.2.1 Creation of the Pinger Signal with Background Noise

In principle, the initial pinger signal consisted of a sine signal with a increasing Fermi distribution to get sensitive for the signal increase. In addition, a decreasing Fermi distribution was multiplied at the end of the signal in order to avoid FFT artifacts caused by a sharp edge. A basic shape of such pinger signal is shown in fig. 4.4.
For the further calculation of the pinger function is based on the analytic function $U^{\text{in}}_{\text{pinger}}(t)$, determined in eq. 4.4.

$$U^{\text{in}}_{\text{pinger}}(t) = U_0 \cdot \frac{\sin\left(2\pi \cdot f \cdot t\right)}{\left(\exp\left(-f \cdot \frac{t-p_1}{0.3}\right)+1\right) \cdot \left(\exp\left(f \cdot \frac{t-p_2}{0.3}\right)+1\right)} + 0.1U_0 \cdot \frac{\sin\left(2\pi \cdot f \cdot t + 0.4\pi\right)}{\left(\exp\left(-\frac{f\cdot(t-p_1)+0.2}{0.3}\right)+1\right) \cdot \left(\exp\left(\frac{f\cdot(t-p_2)+0.2}{0.3}\right)+1\right)} \tag{4.4}$$

With the scaling parameter U_0, the frequency f, the position of the first Fermi edge $p_1 = 0.1\text{ms}$ and the position of the second Fermi edge $p_2 = 2.1\text{ms}$.
$U^{\text{in}}_{\text{pinger}}(t)$ are used as the pinger input signal of the piezo of the acoustical sensor array. The input signal is convolved with the transfer function to obtain the pinger output signal $U^{\text{ou}}_{\text{pinger}}(t)$ of the sensor array. From this follows:

$$U^{\text{out}}_{\text{pinger}}(t) = \left(H \otimes U^{\text{in}}_{\text{pinger}}\right)(t) \tag{4.5}$$

In order to merge the pinger output signal $U^{\text{out}}_{\text{pinger}}(t)$ with the noise data, their sampling frequencies had to be adjusted to each other: meaning that both the pinger and the

noise signal are described by an identical set of time points. Each noise signal is divided into segments of 20 ms. Each of these segments is separately merged with a pinger signal which has a random position within the segment. The pingers' frequencies periodically run successively through nine different values in a predetermined sequence. After each cycle, the amplitude of the pinger is increased as a linear function of the cycle index, but within each cycle the amplitude remains constant. Nine such segments are shown in fig. 4.5. This was done for all four different sets of noise data. As a reference, the bare pinger signal is also provided for each segment with the identical parameters as the merged pinger, but with the adjusted sampling frequency as the respective noise data. After the merging, all segments were separately transformed into the frequency domain. Then, a one-dimensional peak search by ROOT[6] was applied on all spectra of both the bare pinger and the pinger with noise signals. Fig. 4.6 to fig. 4.9 show nine exemplary spectra for each set of noise data. The unfiltered data with the PMTs offline, see fig. 4.6, has an almost flat spectrum, but for the lower frequencies the noise increases significantly. This high peak in the noise spectrum effects the search of the peaks in the remaining spectrum because only peaks with at least 50% of the maximum peak are found. Due to the big distances between the peak in the noise spectra and the one of interest, a band pass filter, cf. fig. 4.7, should improve the result. This is seen in more detail in the next section. In contrast, in the spectra of the unfiltered data with running PMTs, see fig. 4.8, the noise dominates within the part of interest. In this case, a band pass filter could not simply cut of the peaks, cf. fig. 4.9. More on that in next section.

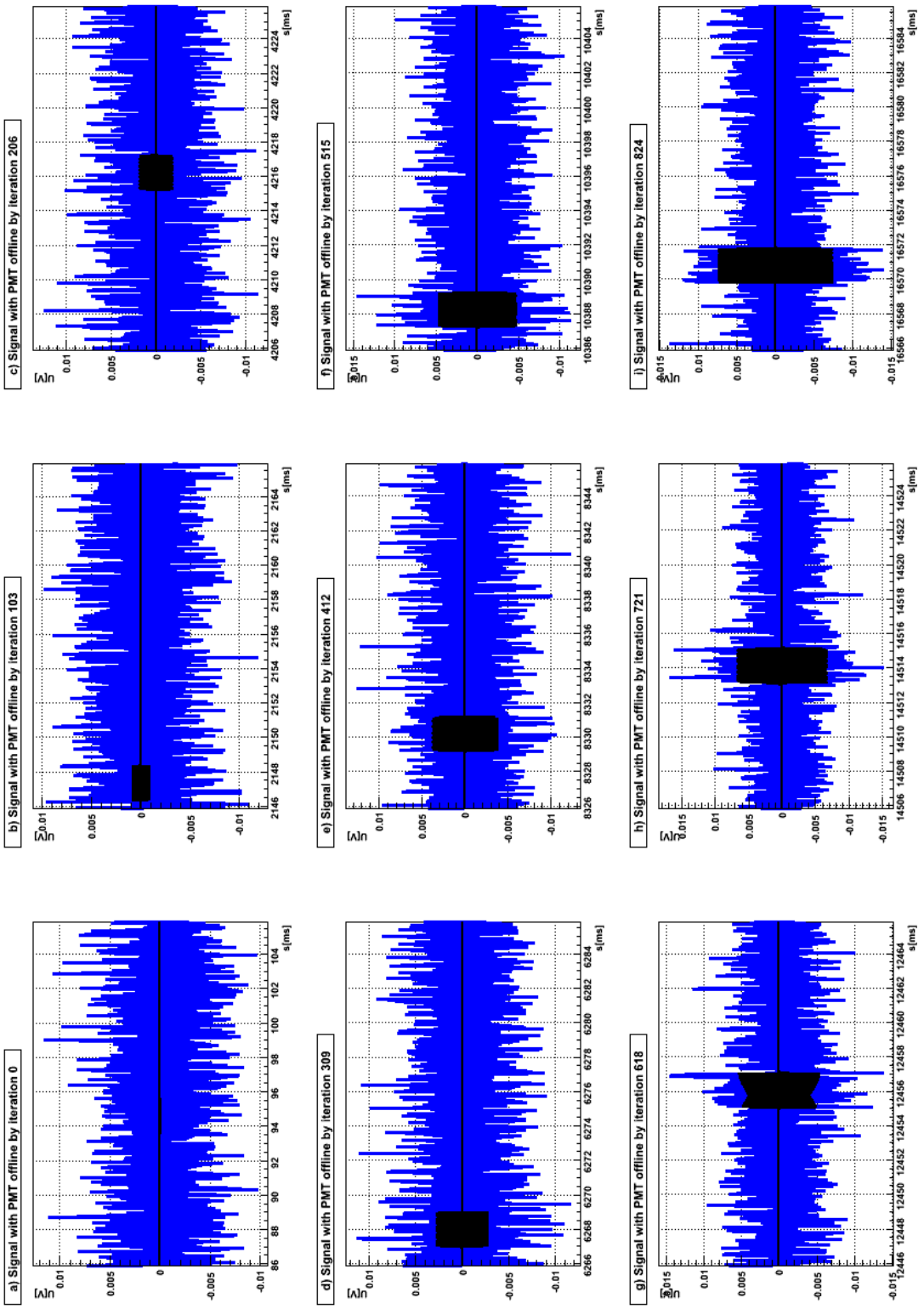

Figure 4.5: The pinger signal with background noise (*blue*) as compared to the bare pinger signal (*black*) for a few selected iterations

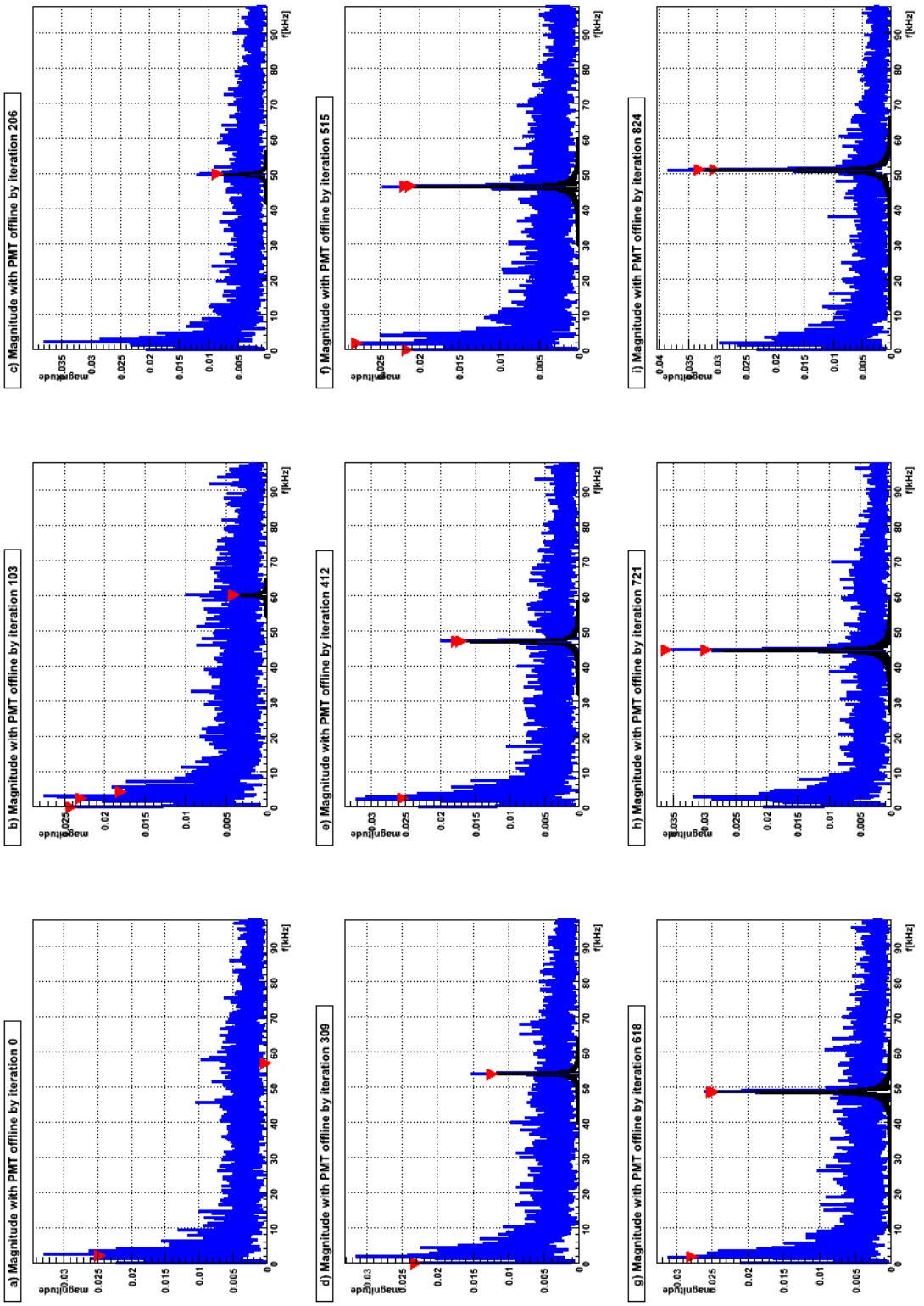

Figure 4.6: The FFTW of the pinger signals with (*blue*) and without (*black*) background noise. The PMTs are offline and no digital filter is used. The found peaks are distinguished by the red triangles

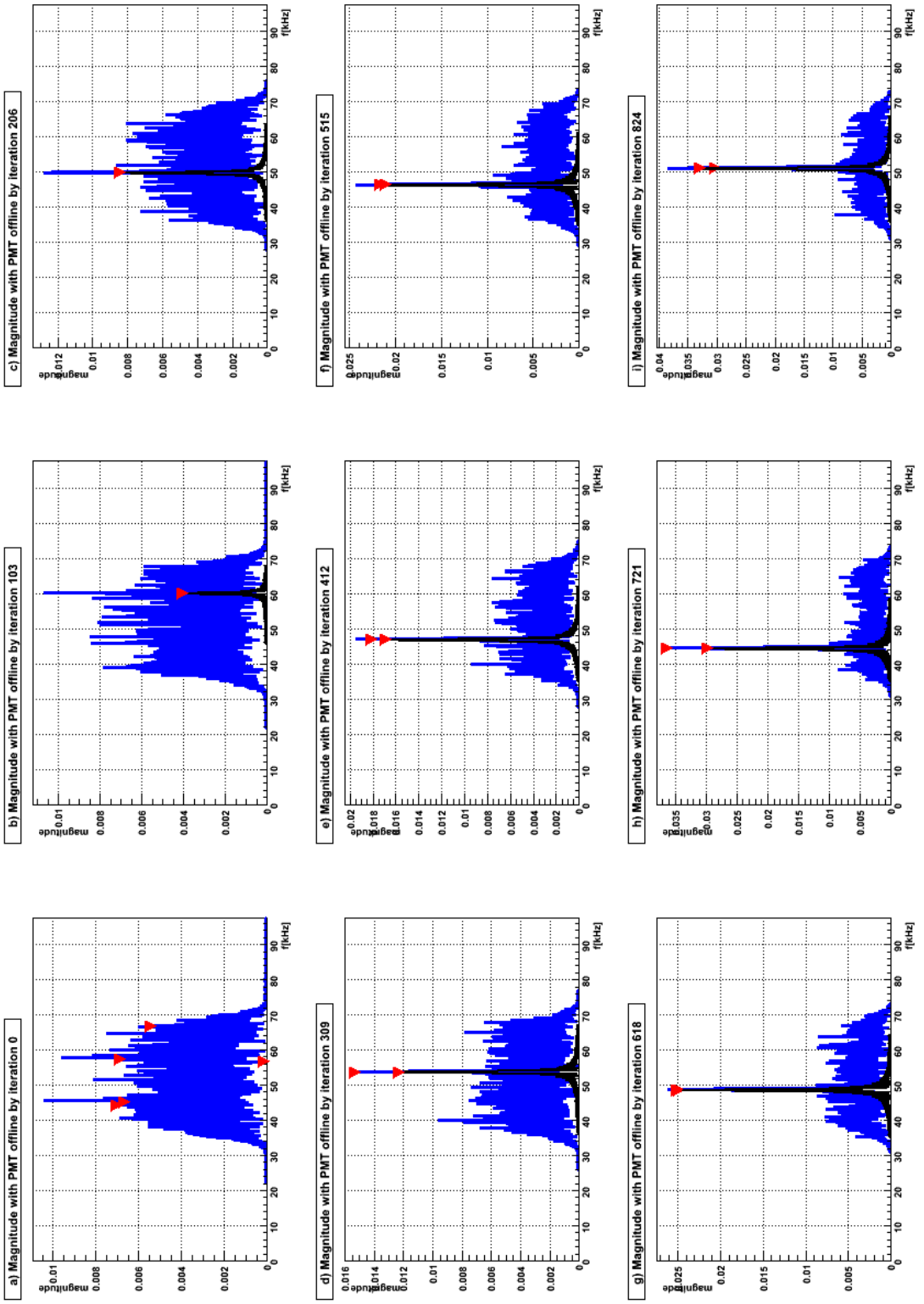

Figure 4.7: The FFTW of the pinger signals with (*blue*) and without (*black*) background noise. The PMTs are offline and a band pass digital filter is used. The found peaks are distinguished by the red triangles

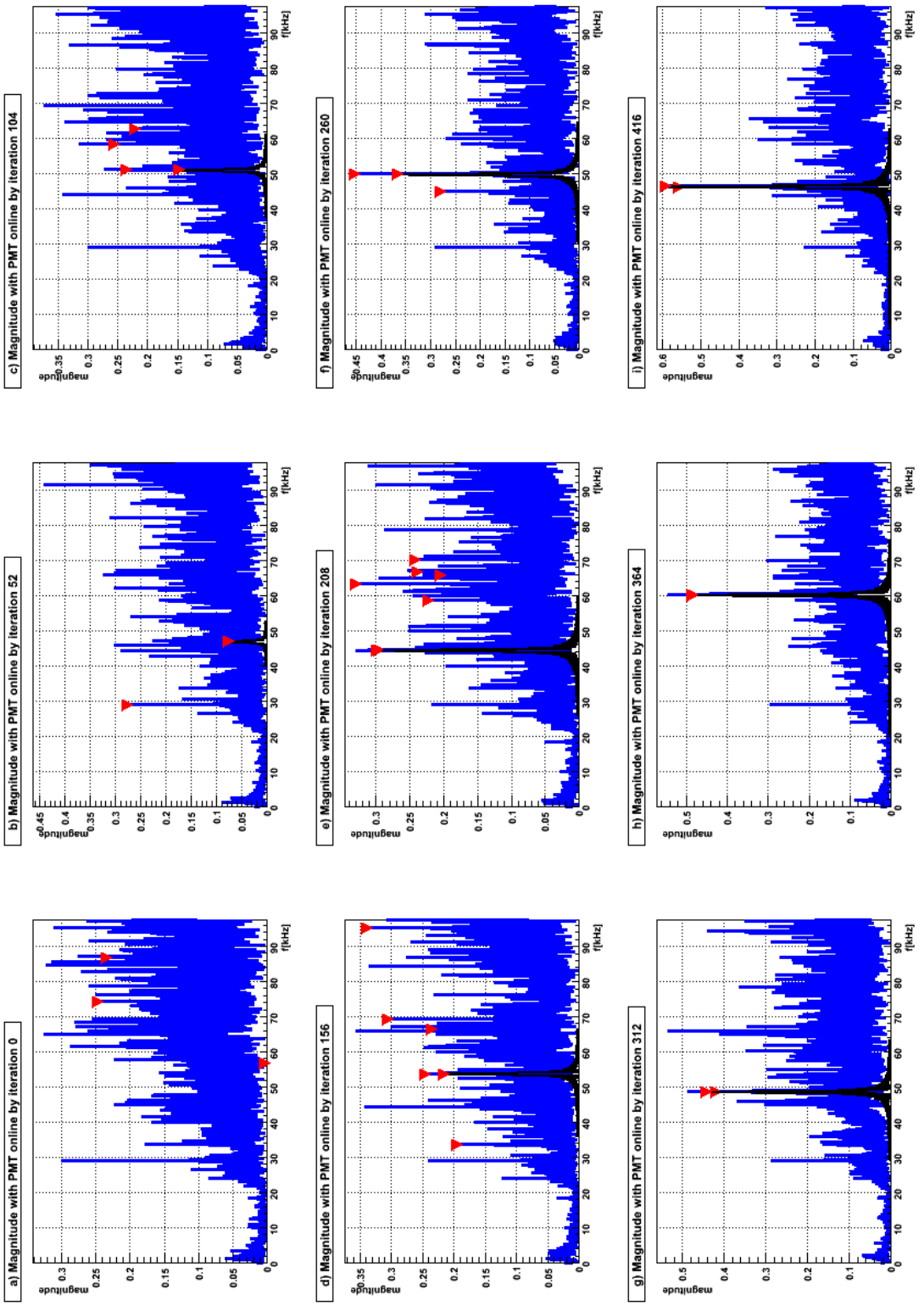

Figure 4.8: The FFTW of the pinger signals with (*blue*) and without (*black*) background noise. The PMTs are online and no digital filter is used. The found peaks are distinguished by the red triangles

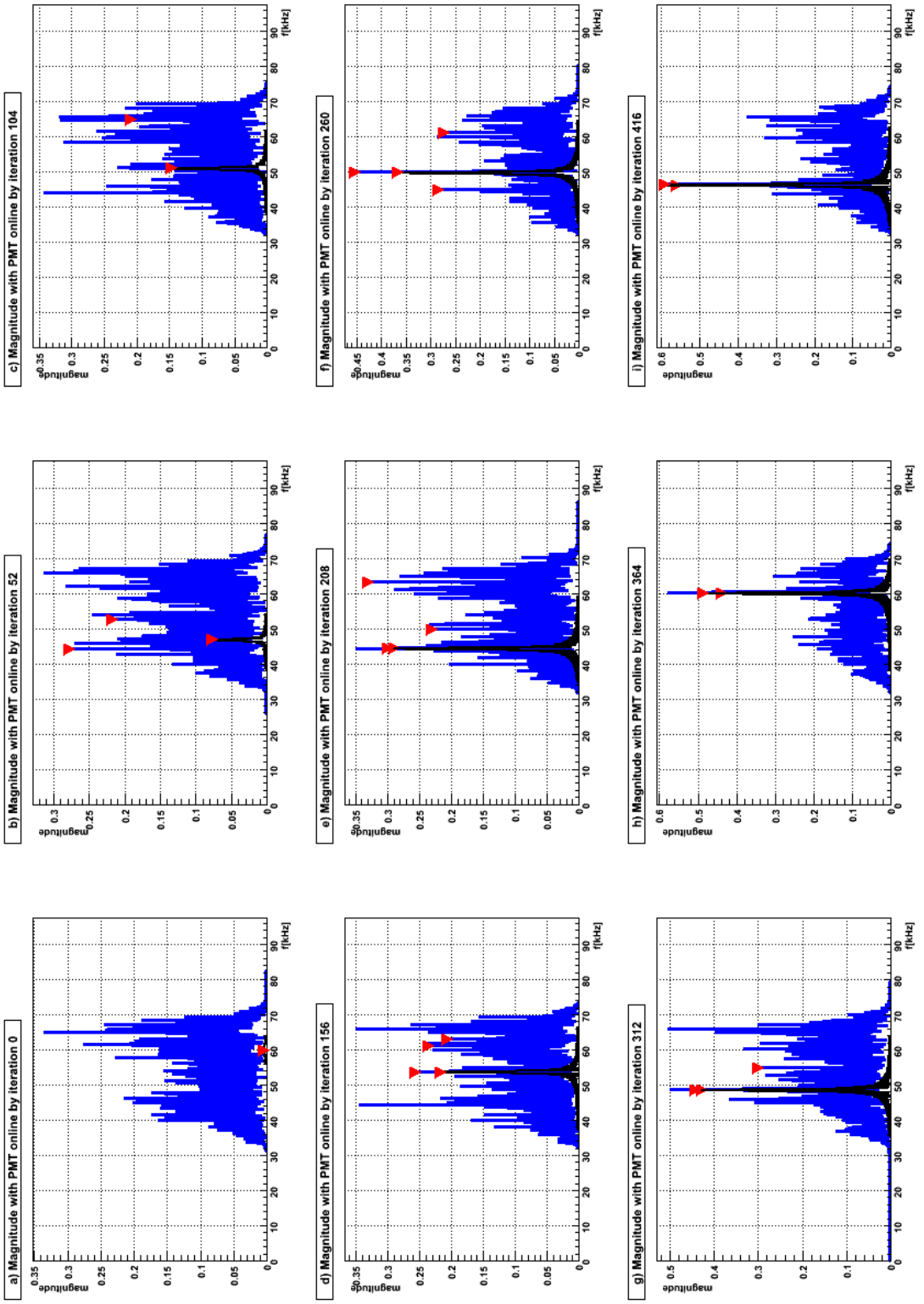

Figure 4.9: The FFTW of the pinger signals with (*blue*) and without (*black*) background noise. The PMTs are online and a band pass digital filter is used. The found peaks are distinguished by the red triangles

4.2.2 Detection in the Background Noise

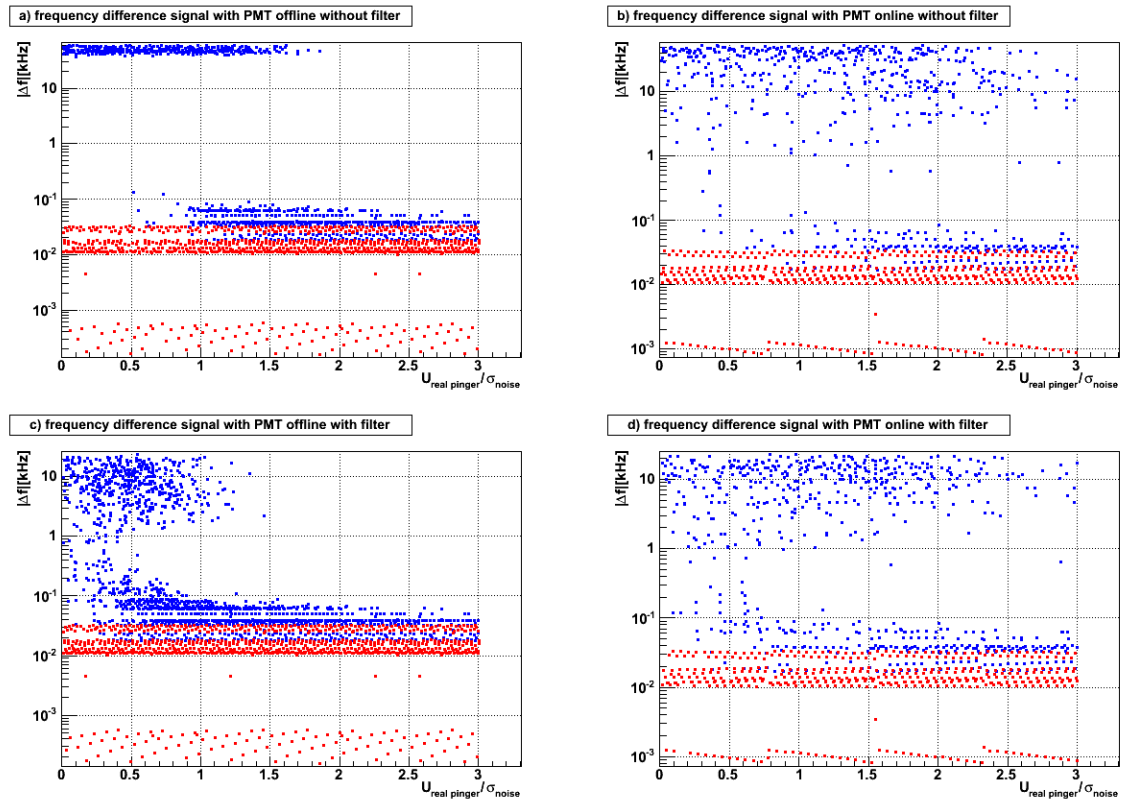

Figure 4.10: The minimal absolute value of the peak frequency difference for the pinger with (*blue*) and without (*red*) background noise

The merging procedure, described in the previous section, was repeated several times, randomly changing only the position of the pinger signal to a different position within the respective noise segment. Usually, more than one peak is found in a signal segment, but only segments with at least one peak are taken into account for the further analysis. For each signal segment, a peak is chosen whose position is closest to any of the nine initial frequencies.
Fig. 4.10 shows the absolute value difference between the frequency of the peak position and actual initial frequency, used in eq. 4.4, as a function of the actual pinger amplitude measured in the respective standard deviation σ_{noise} of the unfiltered noise. The frequency differences for the bare pinger signal are maximal about 40Hz which is in accordance to the FFTW precision of 50Hz conditioned by the segment's range of 20ms. Thus, possible effects which are caused by the adjustment, are precluded.
With disabled PMTs and no filter used, see fig. 4.10a, the shape of the frequency difference distribution consist of two lines. One is located at about 50Hz and the other at about 40kHz. This hard split-up is caused by the peak in the noise data. This shows that the increasing to lower frequencies in the background dominates the peak search. Compared with powered PMTs, see fig. 4.10b, the distribution is more scattered because

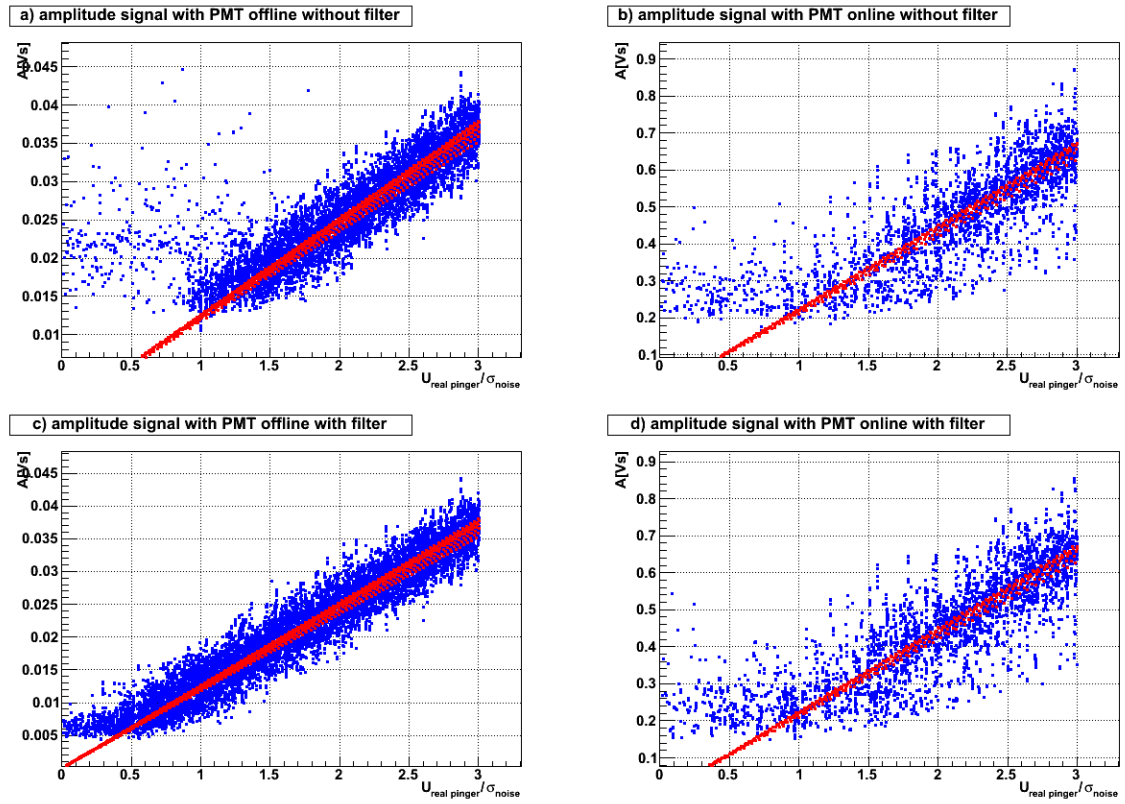

Figure 4.11: The peak amplitude for the pinger with (*blue*) and without (*red*) background noise

the dominant part of the background noise is flatter over a greater frequency interval. By using a band pass filter, see fig. 4.10c and fig. 4.10d, respectively, the peak search with disabled PMTs could be significantly improved, while with powered PMTs it is nearly unchanged. In this case, the filtering could not improve the peak search.
Due to the filtering and the influence of the PMT, a similar situation happens for the peak maximum, seen in fig. 4.11. For higher values of the initial pinger amplitude, the peak maximum is almost linear, but at some point it deviates. This knee yields a first indication how far down the pinger can be detected.

In order to improve the shape of the distributions, they are smoothed and the result is shown in fig. 4.12. According to distributions with the disabled PMTs, a drop in the shapes of the frequency difference distributions can be located around 1.5 σ_{noise} for the unfiltered and 1 σ_{noise} for the filter data. The knee of the peak amplitude is located at 1.5 σ_{noise} for the unfiltered and 0.5 σ_{noise} for the filter data. Taking this together, the pinger can be detected after filtering, if they are greater than 1 σ_{noise} after passing the sensor array. In this case, it is about 3mV. Due to the powered PMT, it has to be greater than 3 σ_{noise}, which is about 0.17V.
Note that this values only gives a upper limit of the detection possibility of the pinger signals. It can be improved by other algorithms. Furthermore, by determining the precise

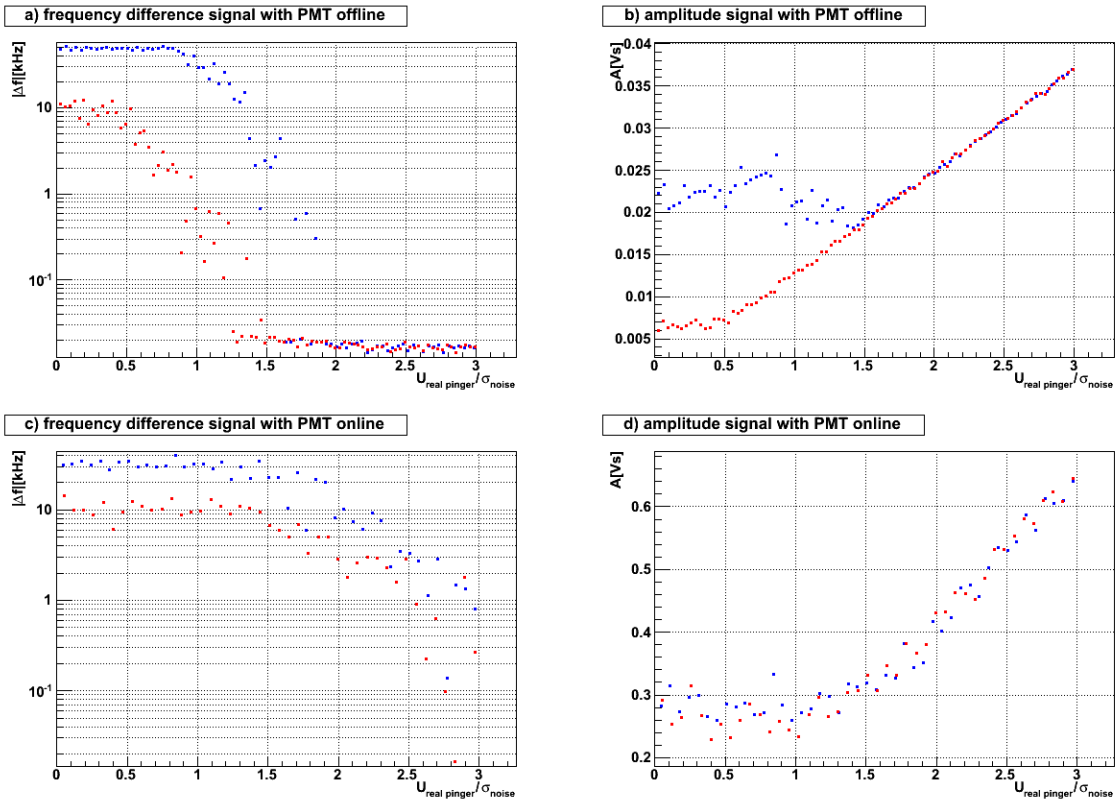

Figure 4.12: The smoothed peak parameters without (*blue*) and with (*red*) digital filter

origin of the PMT noise coupling it may be screen out. But this is not part of this work.

5 Characteristics of different kinds of complete Hydrophones

As mentioned previously, a full understanding of the detector is essential for further analysis, placing a high importance on the understanding of the hydrophones. Therefore, a few hydrophones of each kind are investigated.
For this chapter, a description of the experimental arrangement will be presented. This includes a short introduction of inspected hydrophones, the concept of the measurement and the measurement setup. As a second step, the obtained data is analyzed and artefacts generated by parts of the measurement setup are sorted out for further analysis. For the HTIs a transfer functions was calculated. Finally, the characteristics of the hydrophones are defined by the revised data and arising artefacts are discussed.

5.1 Experimental Arrangement

5.1.1 Inspected Hydrophones

First of all, a short description of the hydrophones used will be given. There were eight hydrophones of four different kinds:

1. **HTI** (*High Tech Inc.*)
   The HTIs were developed and produced by High Tech Inc. and four of the HTIs were tested. Three HTIs labeled HTI-037, HTI-036 and HTI-035 were new hydrophones, while the HTI with the label HTI-010 had been used in ANTARES for approximately five years. The HTI-010 was chosen to create a better contrast between the sensitivity of a new and a used one, how significant the aging of the HTI is.
   The specifications of the tested HTIs type HTI-92-WB are provided by High Tech Inc.[8]

   - Sensitivity: from min -180dB to max -145dB re: 1V/μPa
   - Frequency Response: from 2Hz to 50kHz
   - Maximum Operating Depth: 1000 meters
   - Size: 4.0” length $\times$ 1.5” dia

   A picture of one HTI is shown in fig. 5.1.

Figure 5.1: A picture of a HTI type HTI-92-WB provided by High Tech Inc. [8]

2. **LTI** (*Self-made hydrophone*)
   The LTIs are self-made hydrophones of the ECAP, short for Erlangen Center for Astroparticle Physiks, and they are used in the ANTARES Neutrino Telescope. The development and their specifications are presented in the dissertation of Christopher Lindsay Naumann[5].
   One LTI labeled LTI-112 is characterized in order to compare the sensitivities of the HTIs and the self-made hydrophone. A picture of a finished hydrophone is shown in fig. 5.2.

Figure 5.2: A picture of a LTI hydrophone produced by ECAP. [5]

3. **FFR** (*Sensor Technology*)
   The Free Flooded Rings (FFR) are developed and produced by Sensor Technology [9]. Two FFRs with the labels FFR-10218-06 and FFR-10218-08 of the type SX-30 were tested.
   The provided specifications by Sensor Technology for the FFRs:
   - Resonance frequency: 30kHz
   - Transmit Voltage Response, TVR: 133db re 1μPa/V @ 1 meter
   - Receive Voltage Response, OCV: -193db re 1V/μPa
   - Useable Frequency Range: 20kHz to 40kHz

- Operating Depth: unlimited

4. **SMID** (*Security Multi-sensor Integrated Devices*)
   The SMID hydrophone is developed and produced by SMID Technology[10]. It has been used in the Italian Institute for Nuclear Physics (INFN) and in the NEMO Phase II detector. A picture is shown in fig. 5.3
   There was one SMID inspected using two different setups. The one setup was to measure without a steel box and the other was with a surrounding steel box. This is discussed later in more detail.

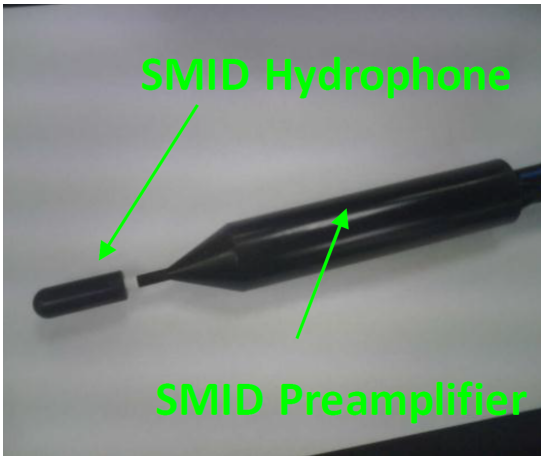

Figure 5.3: A SMID hydrophone with its preamplifier [10]

5.1.2 Concept of the Measurement

The following section will illustrate the concept of the signal response measurement from the hydrophones described in the previous section. Goal of this measurement is to analyze the sensitivity of the hydrophones as a function of the frequency. Due to the fact that the hydrophones had to be installed in the ANTARES Deep Sea Neutrino Telescope, there was just a short period for the measurement, thus the hydrophones are characterized by the Pulse-Analysis method as described in sec. 3.1.3, while further methods of analyses will be omitted.
Drawing on sec. 3.1.3, a δ-pulse would be an ideal input signal for the measurement, however it is not possible to create an exact δ-pulse and secondly even an extreme small pulse could damage or at least overdrive the hydrophone, distorting the measurement. Therefore, Gaussian pulses of different widths were chosen and their parameters determined, so that on the one hand as much as possible of the frequency spectrum was involved and on the other hand the hydrophones were not overdriven. To get an better comparison between the hydrophones, the chosen widths was identical for each hydrophone and just the amplitudes were varied.
Because the hydrophones need a pressure input signal, the Gaussian pulses were sent to

an emitter which turns the voltage signal into a pressure signal. For this reason, four different signals are distinguished by the following notations:

1. $U_{\text{input}}(t)$: The voltage input signal of the emitter
   Fourier transformation: $\hat{U}_{\text{input}}(\omega)$
2. $p_{\text{output}}(t)$: The pressure output signal of the emitter
   Fourier transformation: $\hat{p}_{\text{output}}(\omega)$
3. $p_{\text{input}}(t)$: The pressure input signal of the hydrophone
   Fourier transformation: $\hat{p}_{\text{input}}(\omega)$
4. $U_{\text{output}}(t)$: The voltage output signal of the hydrophone
   Fourier transformation: $\hat{U}_{\text{output}}(\omega)$

Note that $p_{\text{output}}(t)$ and $p_{\text{input}}(t)$ are not measured separately, but calculated from the sensitivity provided by the manufacture.
Hence, the frequency dependent sensitivity of the hydrophones is constituted by the ratio of the pressure input $\hat{p}_{\text{input}}(\omega)$ and the voltage output signal $\hat{U}_{\text{output}}(\omega)$ of the hydrophone. Mind that these two quantities are complex-valued, thus they are defined by the amplitude and the phase.

5.1.3 Measurement Setup

Now, the final measurement setup will be presented. As seen in fig. 5.4(a), a metal tank holds the water wherein both the emitter and the to be inspected hydrophone are contained. The emitter and the hydrophone were placed face to face, so that the notional line between them is parallel to the side walls and the distances to the side walls were equal, as it can be seen in fig. 5.4(b) and fig. 5.4(c). This was done to minimize the effects of reflections of the signal from the side walls, because the closer the hydrophone or the emitter are to the side wall, the closer the temporal distance is between the original signal and the reflected one. This in turn could result in both signals being indistinguishable from each other.
The sieve like steel box, as it can be seen especially in fig. 5.4(c), is used for just one measurement of the SMID hydrophone. All other measurements of the hydrophones, including one of the SMID, are done without this steel box. The purpose of this steel box was to avoid electromagnetic disturbances. But this is discussed later in further detail.
As it was explained for the hydrophones' positioning in the plain, the vertical positioning is also important to prevent an indistinguishability between the original signal and a reflected one. As it is shown in fig. 5.5, the distance to the bottom of the tank was equal to the distance between the emitter and the hydrophone. This is the result of a compromise between a minimal overlapping of the original and a reflected signal and a large enough distance to the emitter in order to prevent near-field effects. Because of the relation of the size between the hydrophone and the depth of the tank, there was just a little clearance for the adjustment.

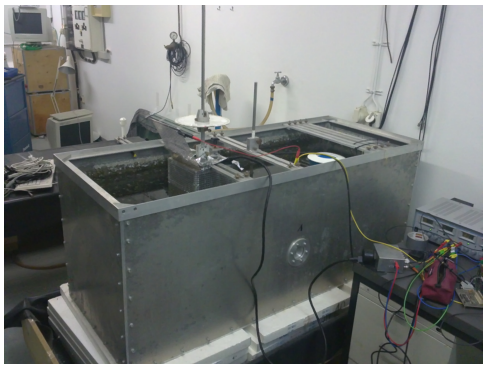

(a) The tank for testing the hydrophones

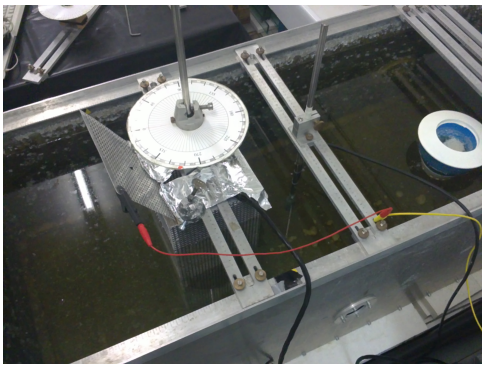

(b) An top view of the measurement setup

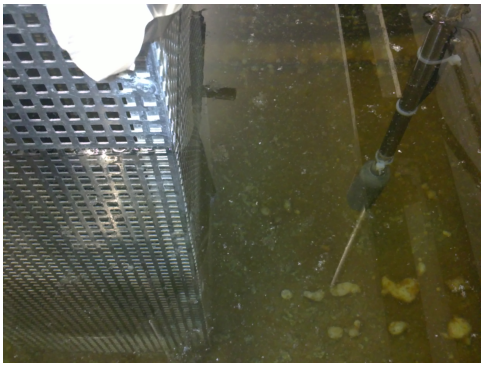

(c) Left: the hydrophone in the steel box;
right: the emitter

Figure 5.4: The pictures show the measurement setup for the SMID hydrophone contained in the steel box

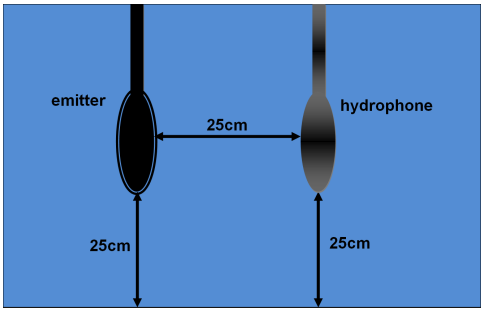

Figure 5.5: A schematic of the hydrophone's position perpendicular to the bottom during the measurement

5.2 Data Analysis

5.2.1 Original Data

Fig. 5.6 is an example of the original data. The amplitudes of the Gaussian pulses are set individually for each hydrophone and pulse widths to prevent an overdriving of the

hydrophone, while still receiving a clear output signal. As a result, the output signals of the hydrophones cannot be directly compared. Thus, each input signal is rescaled to set its peak value to one in the analysis. Of course, each output signal is also rescaled by the same factor of its respective input signal.
As it can be seen in fig. 5.6b, there is a constant voltage offset in the output signal. This DC voltage component yields no relevant information for the hydrophone characterization, but it disturbs the lower frequencies of the signal spectrum. Thus, the signal is shifted, so that if no input signal is picked up the output of the hydrophone is close to zero.
According to the limited size of the water tank, shown in sec. 5.1.3, the signals reflected by the walls are measured by the hydrophones, too. These reflections carry no further information, in fact their analysis is more time intensive and yields no further results than the analysis of the signal measured directly from the emitter. Therefore, the signal was cut off at the time ($\approx$ 0.36ms) the first reflection should theoretically occur. To prevent FFT artefacts caused by a sharp edge, the output signal is set continuously differentiable to zero by an exponential function.

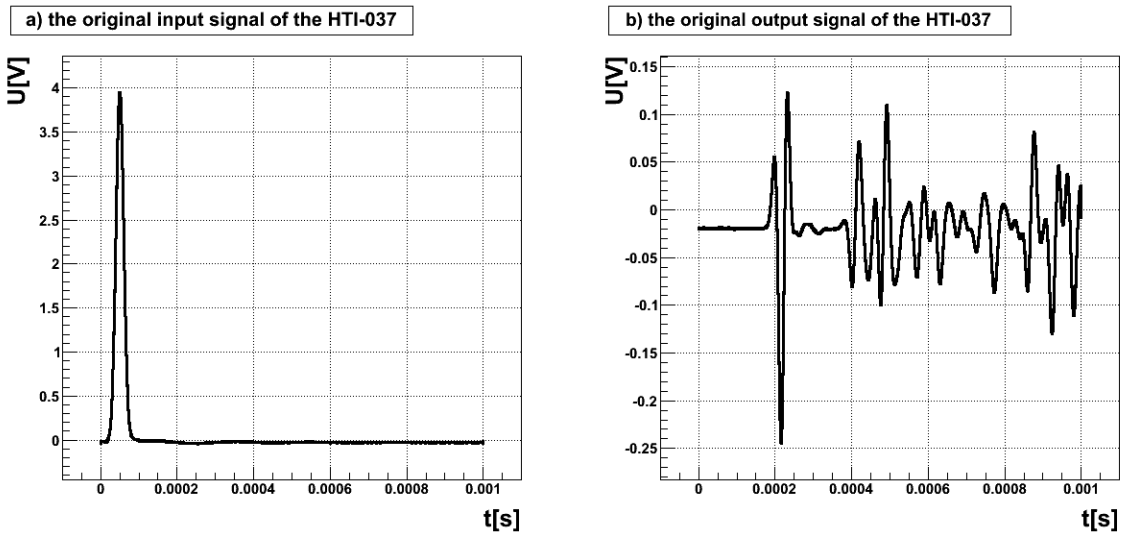

Figure 5.6: The original signal of the HTI-037 hydrophone, generated by a 100μs pulse and recorded directly by the oscilloscope

According to their construction, the FFRs and the SIMD hydrophones have a too low output signal given a maximum input signal, requiring the output signal to be increased by an additional amplifier. The AcouADC board was used to increase the output signal by an factor of 562 for the FFRs and the two measurements of the SMID. Accordingly, the output signal was rescaled a second time by this factor in order to receive the direct hydrophone output signal.
In fig. 5.7 the original data of the two SMID measurements is depicted for one input signal. The primary output signal occurs for both measurements at approximately 2 ms and the reflections at approximately 4 ms, but there is a first peak in the measurement

without the steel box. This peak is simultaneous with the input signal, but this is impossible according to a finite propagation speed of the signal. Therefore, it can assumed that this first peak is of electric origin and due to a mismatch in the measurement setup for the SMID hydrophone and as a result, the measurement is repeated with the steel box, seen in fig. 5.4. Note that this peak only occurs in the SIMD measurement, but it is assumed that this is a phenomena caused by the measurement setup and it should not occur in the deep sea.

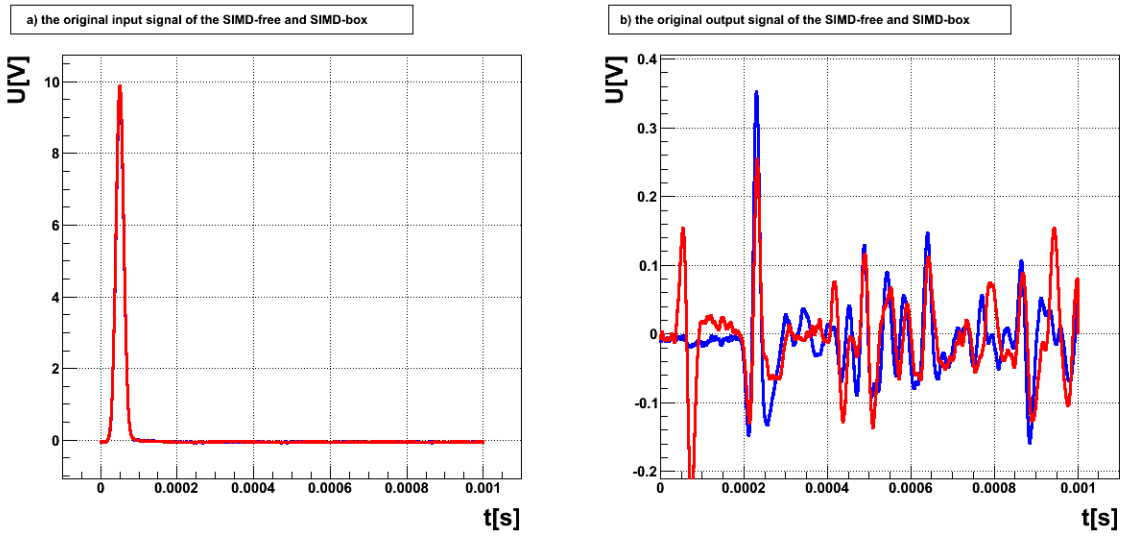

Figure 5.7: The original signal of the SMID hydrophone, generated by a 100μs pulse and recorded directly by the oscilloscope. The *red* line represents the measurement without the steel box and the *blue* line with steel box, respectively

To arrive at the characteristics of the hydrophone, the ratio between the output and input signal was examined. But the pressure input signal of the hydrophone is unknown, only the input signal of the emitter is known. Thus, the pressure output signal of the emitter is calculated in the frequency domain via the sensitivity $\hat{H}_{\text{emitter}}(\omega)$ of the emitter provided by the manufacture. Note that they only provide the sensitivity of the magnitude, the phase is assumed to be constant. From this follows that:

$$\hat{p}_{\text{output}}(\omega) = \hat{H}_{\text{emitter}}(\omega) \cdot \hat{U}_{\text{input}}(\omega) \tag{5.1}$$

In addition, the pressure input signal at the hydrophone is calculated in the frequency domain by scaling the magnitude with the geometric attenuation $H_{\text{geometric}}$ and adding the linear phase term $\varphi_{\text{propagation}}(\omega)$ which is constituted by

$$\varphi_{\text{propagation}}(\omega) = -\Delta t \cdot \omega = -\frac{\Delta x}{v_{\text{sound}}} \cdot \omega \tag{5.2}$$

Δt being the time the signal needs to get from the emitter to the hydrophone, Δx is the distance between emitter and hydrophone and $v_{\text{sound}} \approx 1480\text{m/s}$ is the velocity of sound

in the water tank. As a consequence:

$$\hat{H}_{\text{propagation}}(\omega) = H_{\text{geometric}} \cdot \exp\left(i\varphi_{\text{propagation}}(\omega)\right) \tag{5.3a}$$

$$\hat{p}_{\text{input}}(\omega) = \hat{H}_{\text{propagation}}(\omega) \cdot \hat{p}_{\text{output}}(\omega) = \tag{5.3b}$$

$$= \hat{H}_{\text{propagation}}(\omega) \cdot \hat{H}_{\text{emitter}}(\omega) \cdot \hat{U}_{\text{input}}(\omega) \tag{5.3c}$$

$$= \hat{H}_{\text{total}}(\omega) \cdot \hat{U}_{\text{input}}(\omega) \tag{5.3d}$$

The magnitude and the phase of the total transfer function of the emitter and the propagation are presented in fig. 5.8. All pressure input signals are calculated via $\hat{H}_{\text{total}}(\omega)$ in the frequency domain.

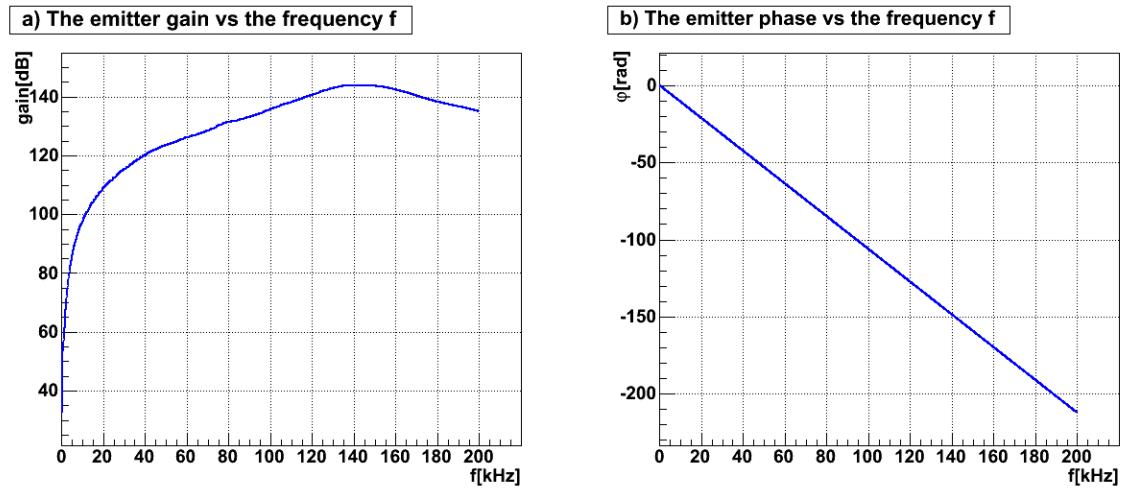

Figure 5.8: The total sensitivity of the emitter used for the hydrophone characterization. The gain is provided by the manufacture in dB re 1V/μPa and no phase difference is assumed. Additionally, the gain is scaled by a geometric factor and a linear phase term was added in order to obtain the sensitivity at the hydrophone

In the following part, the single revised signals are examined in the time domain. To get the output signals of the hydrophones comparable to each other, the input signals had to be as identical as possible. Therefore, both the measured voltage input signal of the emitter and the calculated pressure input signal are depicted for each hydrophone and pulse width to ensure they can be assumed to be identical, which proved to be true, as seen in fig. 5.9 to fig. 5.12.

As it can be seen in fig. 5.9, the HTI hydrophones describe an almost identical response signal for all three pulse widths. There is only a slight difference discernible in the fading out of the signal. Thus, it can be assumed that all other new HTI hydrophones describes a similar response.
More important are the signal response differences after a few years in the deep sea. For this reason, a new HTI is compared with the used HTI-010 and the self-made hydrophone

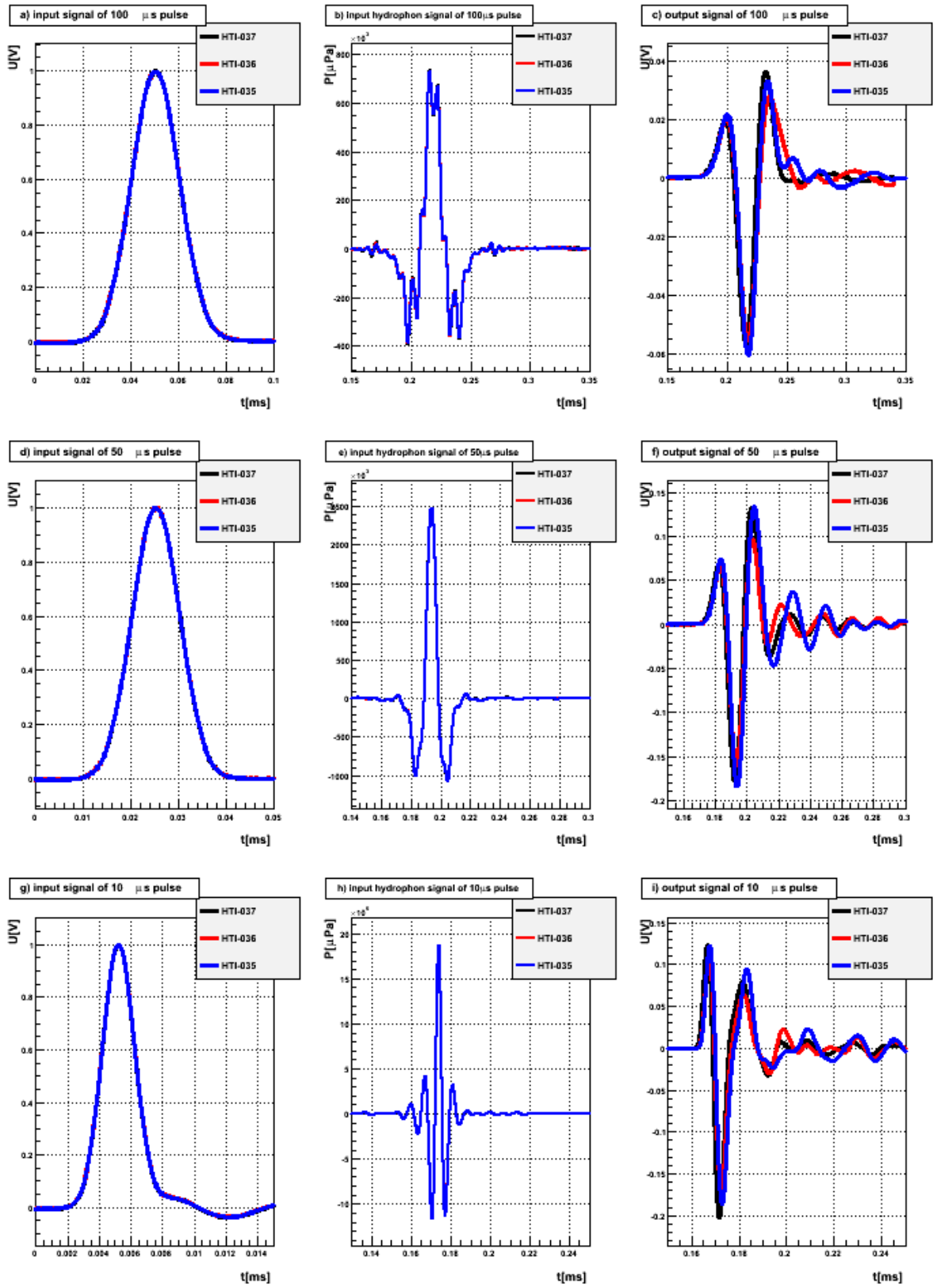

Figure 5.9: The revised data of all three measured pulses for the HTI hydrophones, including the calculated pressure input signal

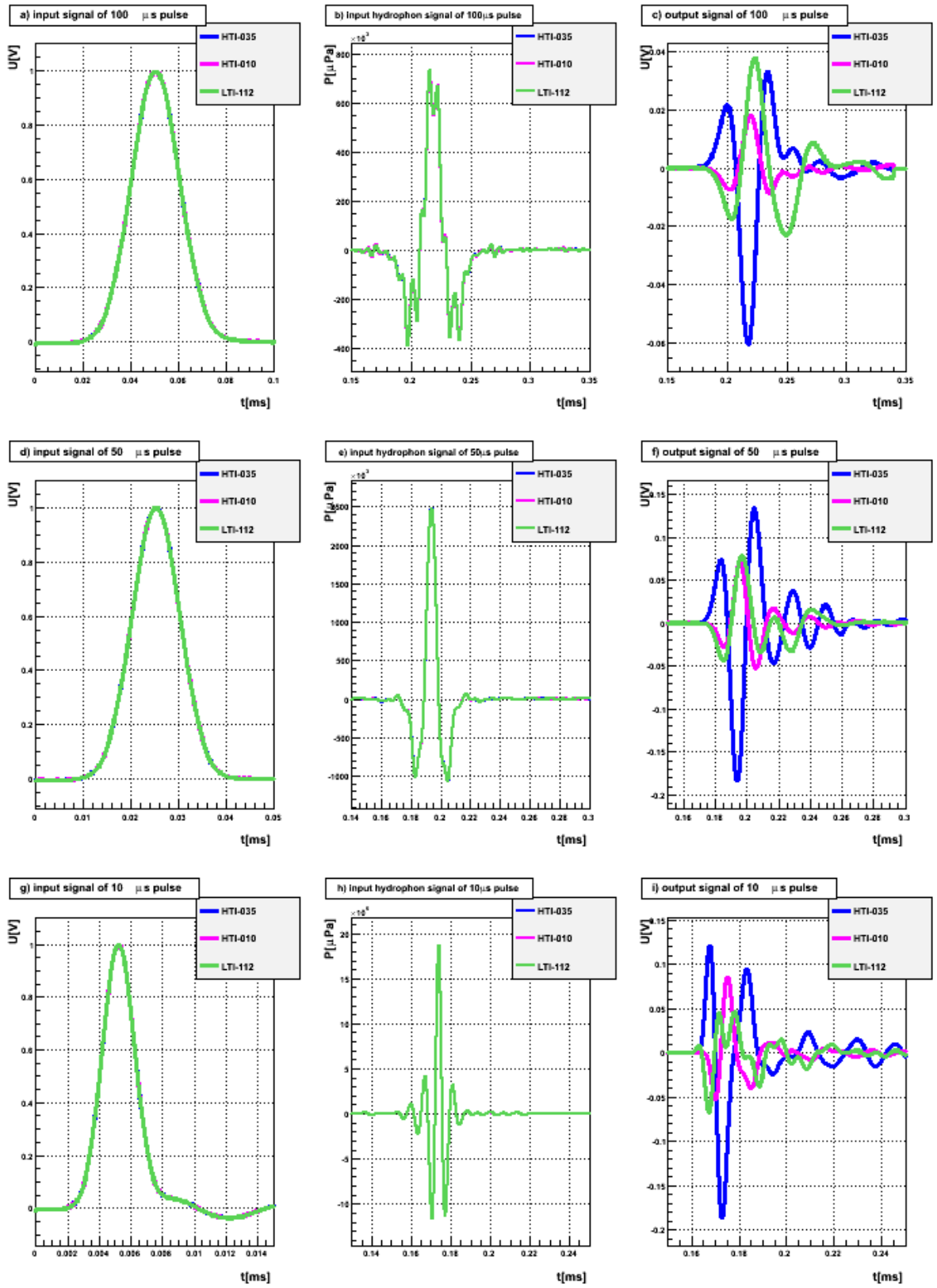

Figure 5.10: The revised data of all three measured pulses for a new HTI, the used HTI-010 and the LTI hydrophone, including the calculated pressure input signal

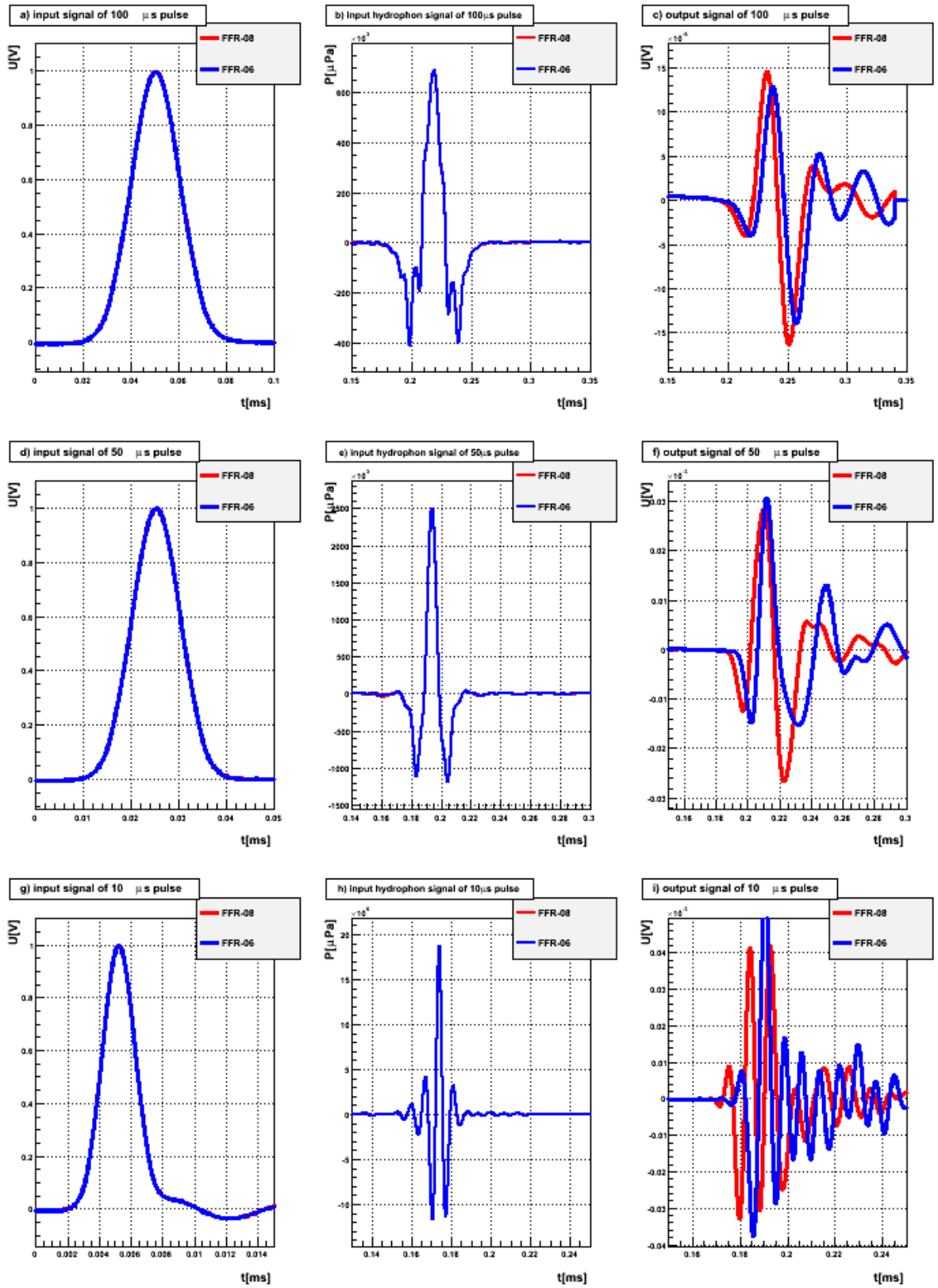

Figure 5.11: The revised data of all three measured pulses for the Free Flooded Rings hydrophones, including the calculated pressure input signal

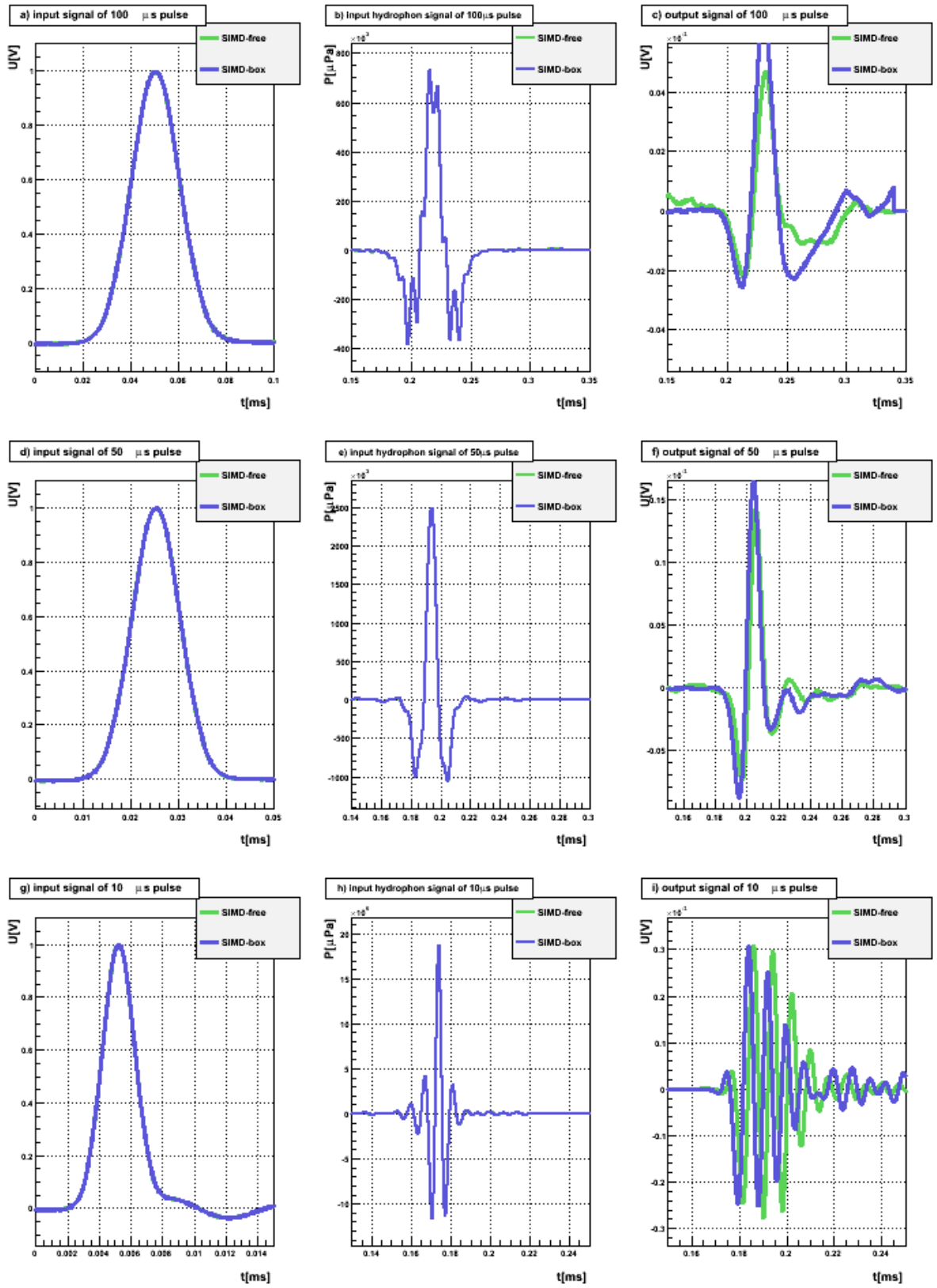

Figure 5.12: The revised data of all three measured pulses for the SMID hydrophone (with and without the steel box), including the calculated pressure input signal

LTI-112. Leaving aside the fact that the used HTI and the LTI are inverted, they describe a similar signal response, seen in fig. 5.10. The HTI-010 only has a lower amplitude than the new one; but for the LTI the smaller the pulses, the more distorted the response signal becomes. It seems that the LTI is stretched to its limits for such small pulses.
Fig. 5.11 shows the signal response of the FFRs. For the widest pulse width, the two FFRs describe the same response. But the smaller the pulse widths, the more distorted the response becomes. So it seems that the FFRs are also stretched to their limits for such small pulses.
For the time interval of interest for the SMID, the two measurements yield an almost identical signal response. According to this, it was assumed that the steel box has no effect on the characteristics of the SMID and the results can also be applied to measurements without the steel box.
All in all, at a first glance the hydrophones exhibit their expected behavior. Further analysis will give a more detailed insight into the behavior and the characteristics of the hydrophones.

5.2.2 HTI Transfer Funktion

To analyze the data measured in deep sea a detailed understanding of the hydrophones has to be established. For this purpose, the HTIs should be described by an analytic transfer function which is found in the same way as described in chap. 3.
All of the three new HTI spectra are used for the calculation. Fig. 5.13a,b show the magnitude and the phase of the input frequency spectra scaled by the emitter sensitivity, seen in fig. 5.8, to get the pressure input signal at the hydrophone, while fig. 5.13c,d show the magnitude and the phase of the unchanged voltage output frequency spectrum. The spectra are limited in the frequency to a maximum of 200 kHz, because the emitter's sensitivity is only known up to this frequency. The resulting transfer distribution is given in fig. 5.13e,f. Because of the differences between the hydrophones, seen especially in fig. 5.13c, the transfer distribution had to be smoothed over for all nine spectra to improve the adaptation of the analytic function.
For the amplifier, seen in chap. 3, the analytic function was based on their schematics. But in the case of the HTI, the schematics were unknown, thus the analytic function is based only on the measured output characteristics. As a result, the analytic function is not meant to be the exact transfer function but rather a approximation of the measured distribution.
Another difficulty lies in the pulse width being too small to receive significant values for the lower frequencies. Thus, it is not possible to examine whether there is some kind of high pass behavior of the hydrophones.

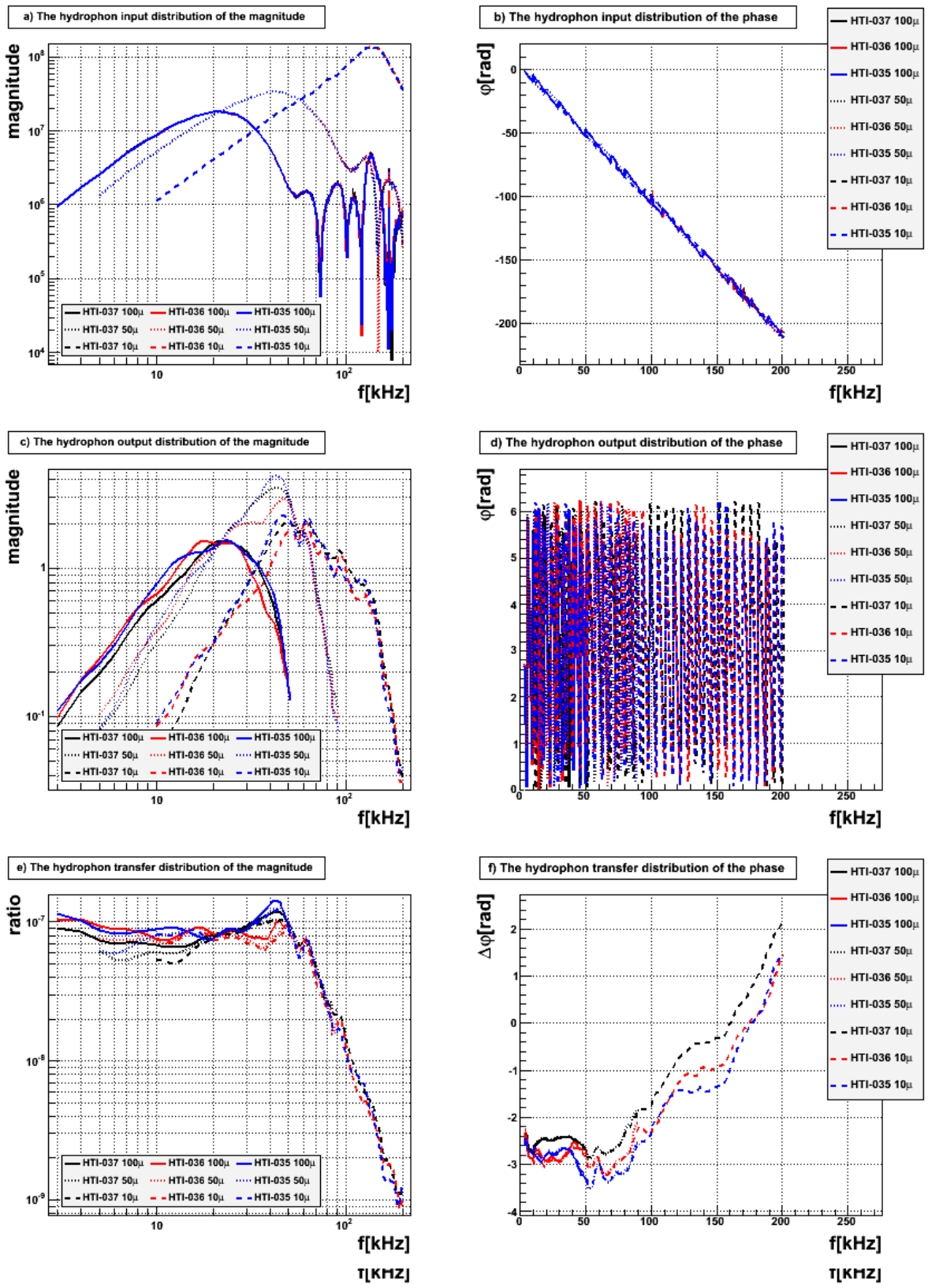

Figure 5.13: The spectra of the HTI hydrophones used for the calculation of the transfer function

Taking all this into account, magnitude of the analytic function results to:

$$A = A_{\text{tot}} \cdot \prod_{i=1}^{2} \left[A_i^{\text{sallen}} \right] \tag{5.4a}$$

$$A_i^{\text{sallen}} = \frac{1}{\sqrt{\left(1 - \left(f/f_i^{\text{sallen}}\right)^2\right)^2 + \delta_i^{\text{sallen}} \cdot \left(f/f_i^{\text{sallen}}\right)^2}} \quad (\textit{Sallen-Key low pass}) \tag{5.4b}$$

While the phase results to:

$$\varphi = \varphi_{\text{tot}} + \sum_{i=1}^{2} \left[\varphi_i^{\text{sallen}} \right] + \varphi^{\text{lin}} \tag{5.5a}$$

$$\varphi_i^{\text{sallen}} = \arctan\left(\frac{\sqrt{\delta_i^{\text{sallen}}} \cdot f/f_i^{\text{sallen}}}{\left(f/f_i^{\text{sallen}}\right)^2 - 1} \right) \quad (\textit{Sallen-Key low pass}) \tag{5.5b}$$

$$\varphi^{\text{lin}} = -2\pi \cdot \delta^{\text{lin}} \cdot f \quad (\textit{linear phase}) \tag{5.5c}$$

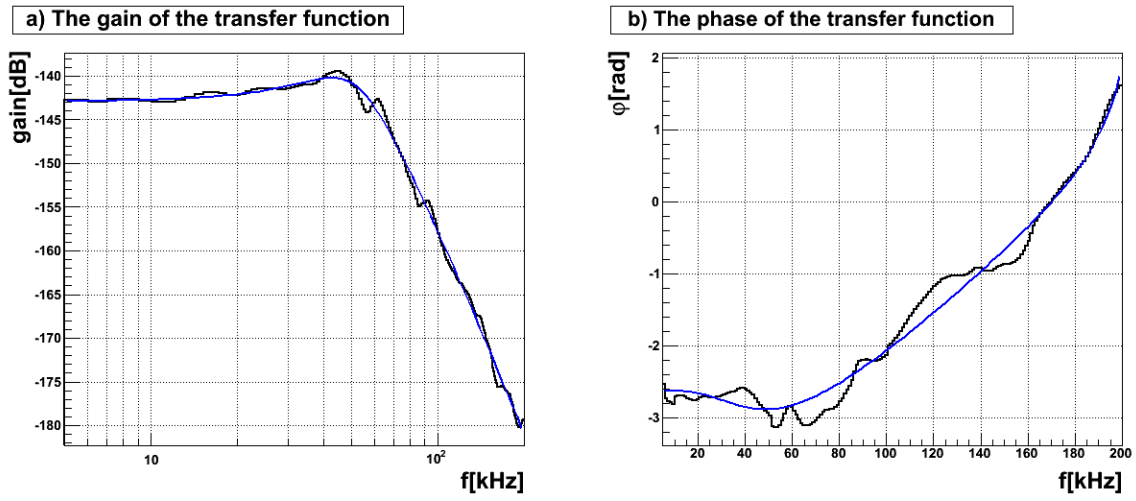

Figure 5.14: The transfer function (*blue* line) fitted to the data smoothed over all HTI spectra (*black* curve)

The approximations of the smoothed data by an analytic function, determined by eq. 5.4 and eq. 5.5, are shown in fig. 5.14. Basically, the function describes the measured

total gain:	7.134e-008 ± 2.531e-008	
total phase:	-2.625e+000 ± 5.714e-001	
1. Sallen-Key low pass	frequency f_1^{sallen} [kHz]	shift δ_1^{sallen}
gain	5.225e+001 ± 1.683e+001	5.210e-001 ± 5.820e-001
phase	4.293e+001 ± 1.689e+001	1.634e+000 ± 1.994e+000
2. Sallen-Key low pass	frequency f_2^{sallen} [kHz]	shift δ_2^{sallen}
gain	8.599e+001 ± 3.147e+001	2.422e+000 ± 4.295e+000
phase	-2.029e+002 ± 8.201e+000	7.624e-003 ± 2.628e-002
linear phase [ms]:	-4.865e-003 ± 7.671e-004	

Table 5.1: The parameter values for the transfer functions described in eq. 5.4 and 5.5

distribution. But on closer inspection, some sort of resonances occur, most probably generated by the piezo element of the hydrophone. These resonances were not taken into account for the analytic function because of their low intensity and for time reasons. Far more important is the distribution of the phase, because it has a positive global slope. Tab. 5.1 shows the values of the analytic function calculated by the fit: negative parameter values occur only for the phase. Particularly, for the linear phase term a negative parameter would imply that the output signal is measured before the input signal arrived the hydrophone, but this is physically not possible. The most likely explanation for this is that the assumption, taking zero for the emitter's phase shift, was not correct or that there are inconsistencies in the values for the velocity of sound and the distance between the hydrophones. To examine this, a further characterization of the emitter would be necessary, but this is not part of this work.

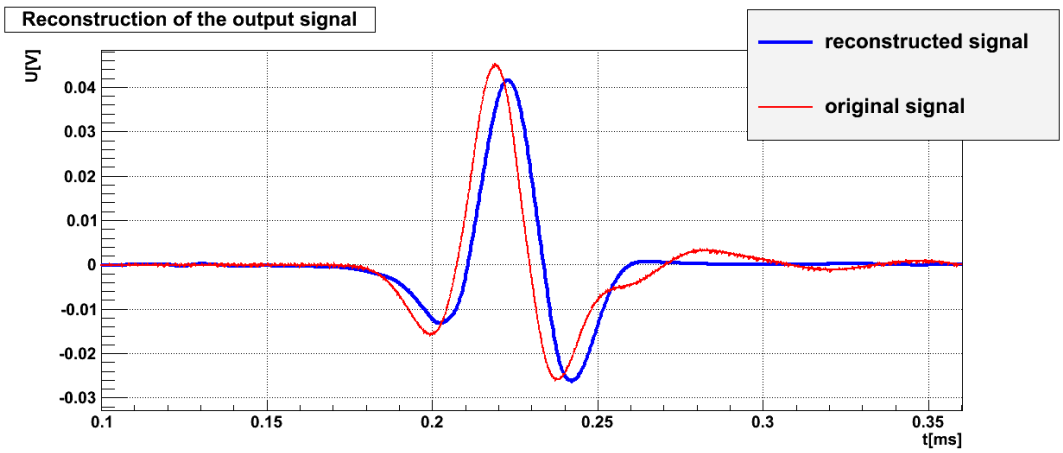

Figure 5.15: The reconstruction of one output signal calculated via the emitter input signal and the transfer function of both the emitter and the hydrophone

To ensure that the previous calculation is consistent, one voltage output signal is reconstructed via the transfer functions for the emitter and the hydrophone utilized on the voltage input signal. The result is seen in fig. 5.15. It is just slightly shifted in time

and is not fading out, as compared to the original one. This is possibly caused by the afore mentioned mismatch of the resonances. But as seen, this is just a small effect on the reconstruction. So it can be assumed that the positive slope in the phase is not the result of a failure of the calculation.

5.2.3 Characteristics of the Hydrophones

In the following subsection, the characteristic sensitivities of the hydrophones are calculated in the exact same manner as for the new HTI, shown in fig. 5.13. For these sensitivities, the same emitter sensitivity is used, as seen in fig. 5.8. For the sake of completeness, the sensitivities of the new HTI are also presented.
Fig. 5.16 shows the full sensitivities of the new HTIs. As expected, all hydrophones describe the same distribution, but for the two lower pulse widths the phase difference is almost constant up to the frequencies dominated by the noise, while there is only a slope for the smallest width. According to the available data, it is difficult to determine what caused this positive slope.
Comparing a new HTI with the used HTI-010, see fig. 5.17, there is a constant differences of about 10 dB between them, otherwise they describe an almost identical distribution. Thus, the aging of the HTI hydrophones seems mainly to effect the total frequency independent gain, while the qualitative distributions are just slightly changed. But this reduction is greater than the expected 3 dB from the deep sea observation [12]. It could caused by the huge pressure change during the recovery and the redeployment of the hydrophone. For a more detailed study of the aging, further measurements would be necessary.
In comparison with the LTI, see also fig. 5.17, the HTIs and the LTI hydrophones have a similar distribution, but for the higher frequencies the HTIs are more sensitive. For the smallest pulse width, see fig. 5.17e, the low pass behavior of the LTI is disturbed at frequencies greater than 70 kHz. This could be caused by the LTI being stretched to its limit for such small pulses, while the HTIs show a clear low pass behavior.
In contrast to the HTIs, the FFR hydrophones show bigger differences among themselves, as shown in fig. 5.18. Hence, it is not possible to calculate a general transfer function valid for all FFRs. However, due to the absence of a pre-amplifier, the FFRs can be used as both a hydrophone and an emitter, but as a consequence, their gain is very low. By comparison with the HTI, their gains are about 60 to 70 dB lower.
Because of its pre-amplifier, the SMID hydrophone is about 15 dB more sensitive than the FFR, as seen in fig. 5.19. But in relation to the HTIs, these are still far more sensitive than the SMID hydrophone. Comparing the two SMID measurements, the effect of the steel box is an attenuation of the ripples. These ripples are due to some electromagnetic coupling to the hydrophone, but their exact cause is unknown. It is assumed that it occurred only due to the laboratory environment of the measurement setup and will not arise in the deep sea.

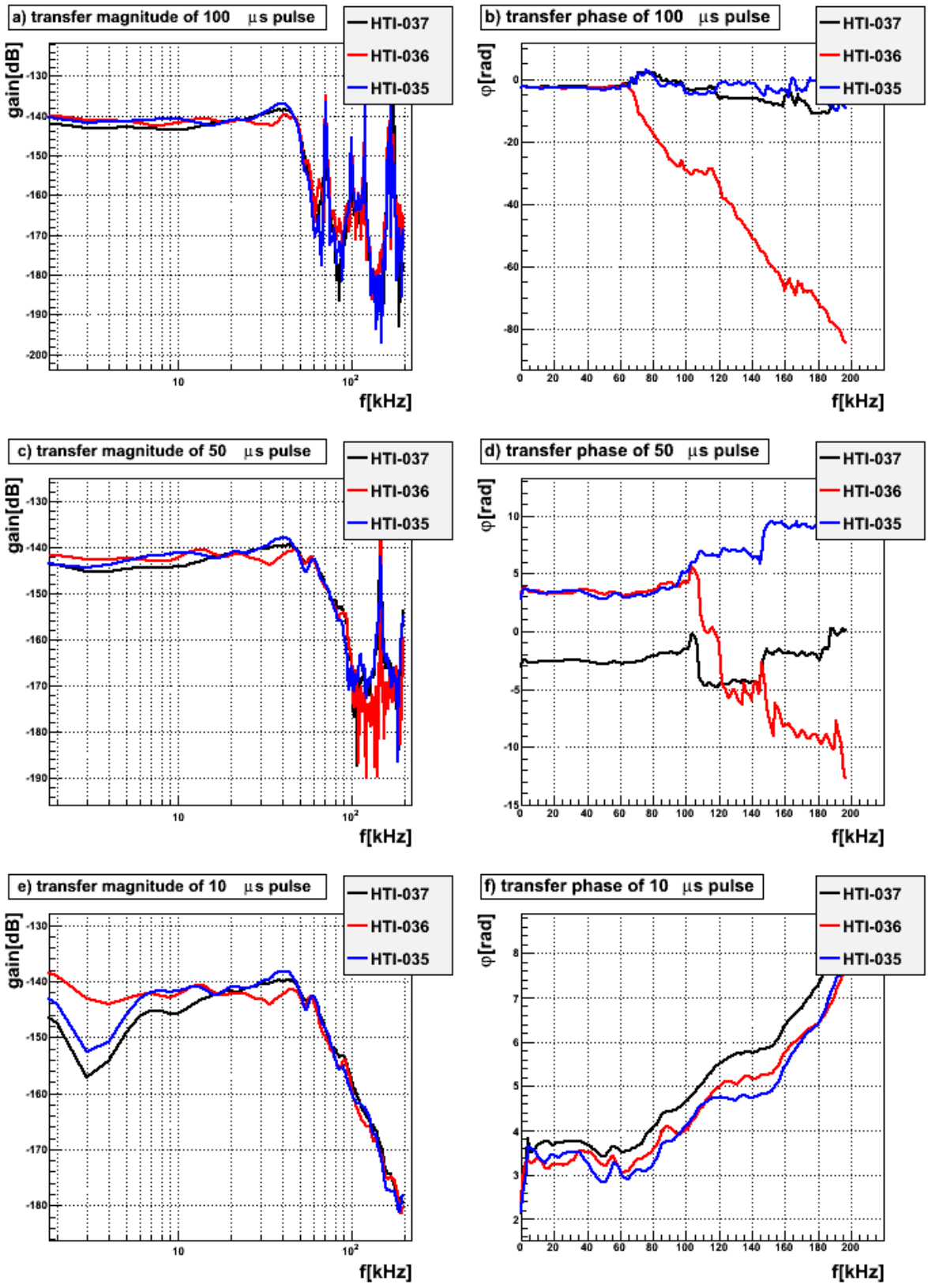

Figure 5.16: The characteristics of the new HTI hydrophones for all three different pulse widths

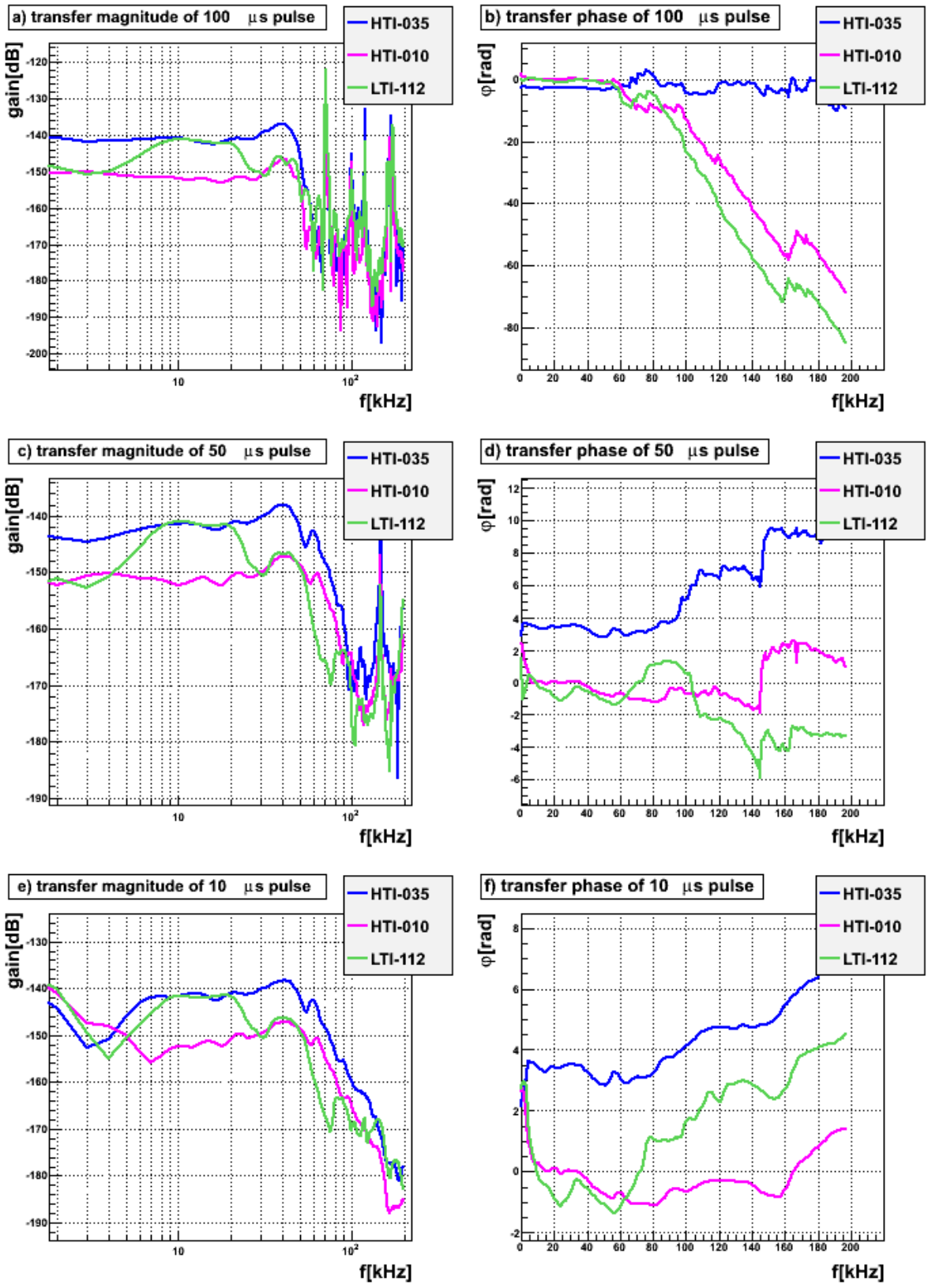

Figure 5.17: The characteristics of the used HTI-010 and the LTI hydrophone for all three different pulse widths

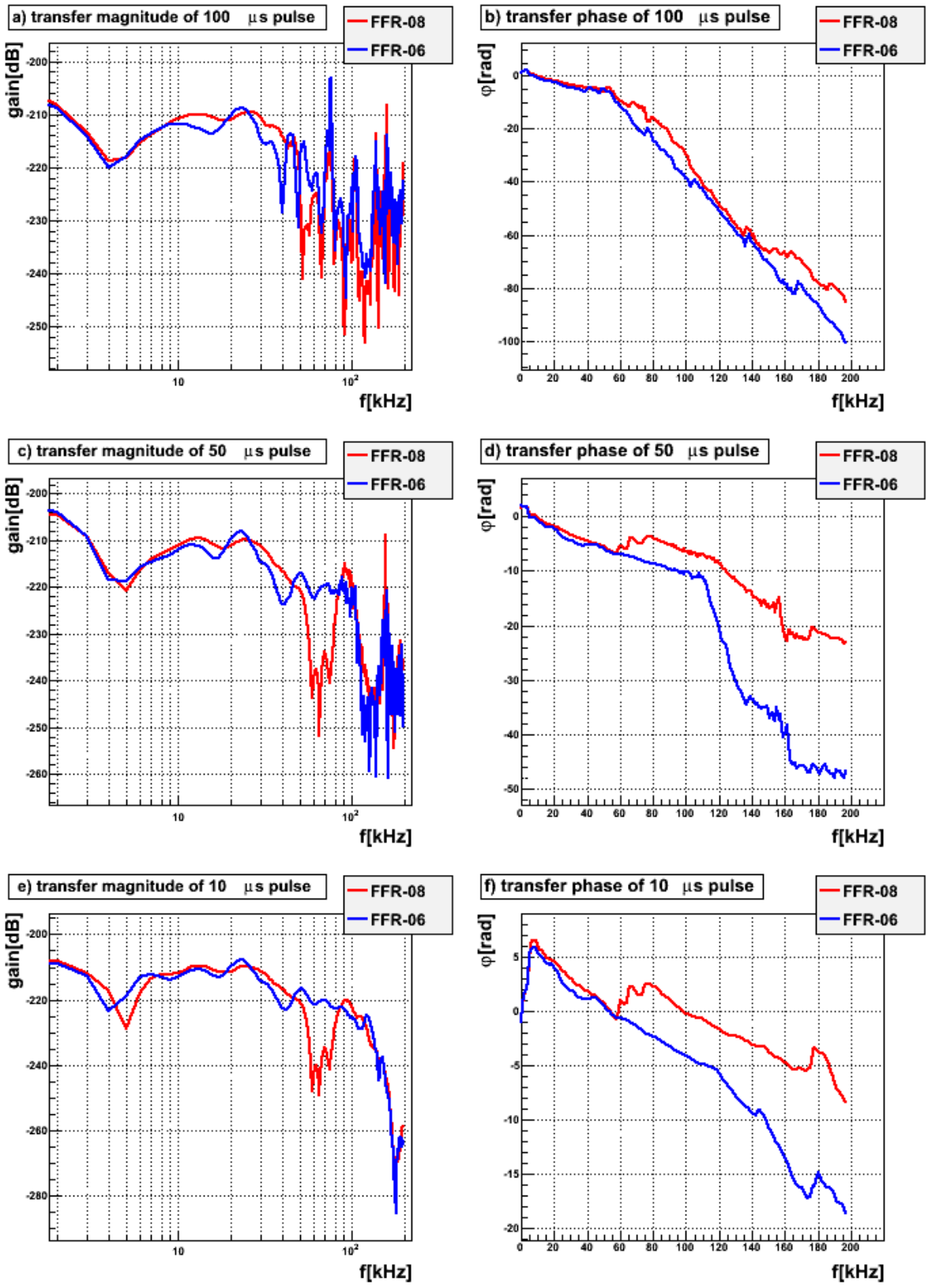

Figure 5.18: The characteristics of the new FFR hydrophones for all three different pulse widths

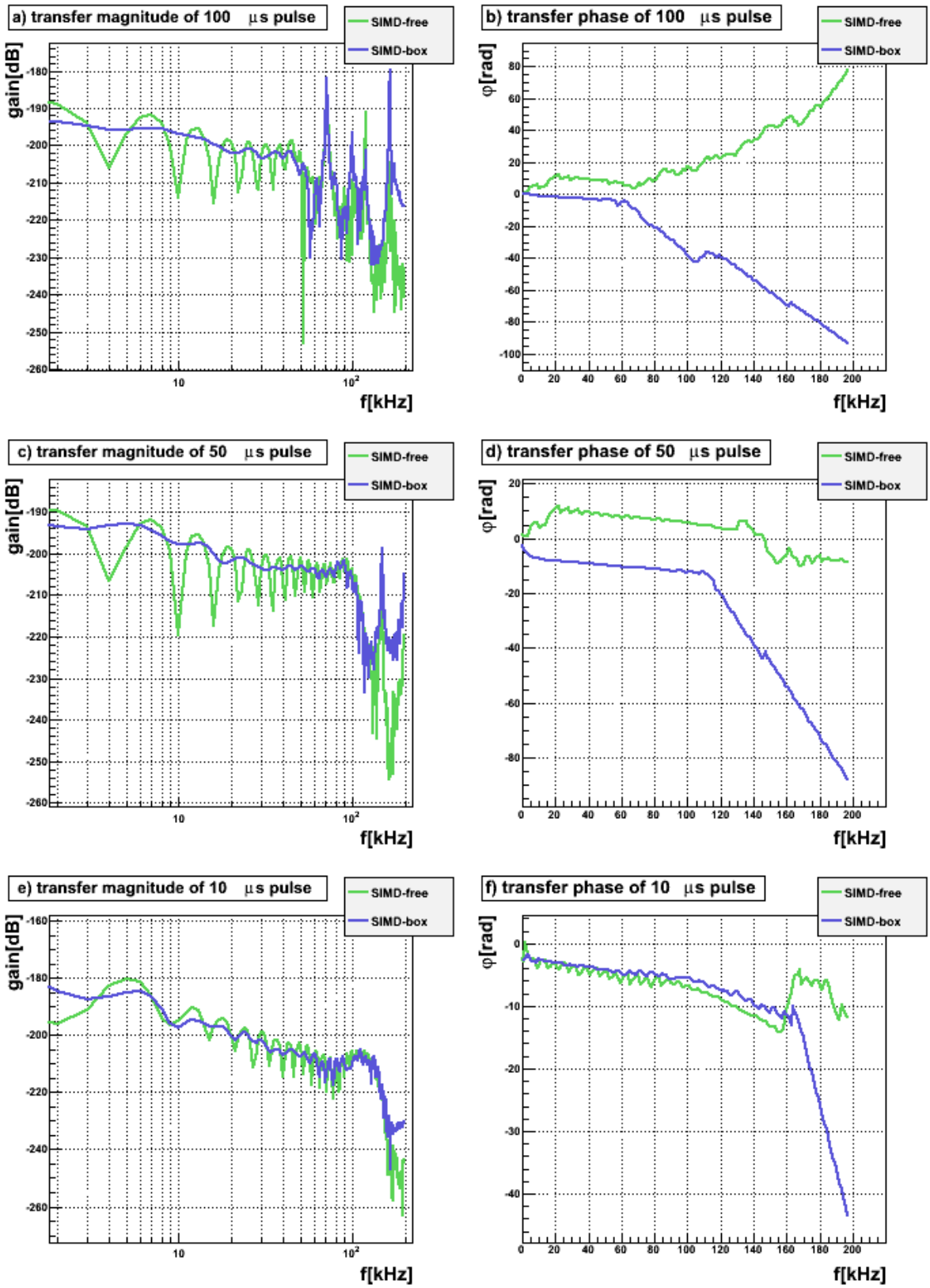

Figure 5.19: The characteristics of the new SMID hydrophone for all three different pulse widths

6 Summary

Goal of this work was to enhance the understanding of acoustical sensor devices for KM3NeT and ANTARES. These devices can be used to determine the complete positioning in both the displacement and the orientation of the optical modules in deep sea neutrino telescopes by measuring the travel times. Furthermore, they provide an additional detection possibility for neutrinos as they can measure the pressure impulse caused by the neutrino's interaction within the water.
The main part focused on the detailed analysis of the properties of the amplifiers used for acoustical sensors developed at the ECAP. In particular, the acoustical sensors were piezo elements to be glued inside an optical module and being proposed as an option for KM3NeT. For that purpose, the pre- and master amplifier were characterized in order to obtain a transfer function which describes the behavior of a signal passing through the amplifier. For this characterization, two different measuring methods had been used to reduce the impact of potential disturbances during the measurement. The first was to measure the amplifier behavior for signal frequencies using sine signals, while the second method was to measure the pulse response using Gaussian pulses. As a result, it was possible to reconstruct the output signal with known input signal for the amplifiers, including the complete acoustical sensor, consisting of the piezo element, the pre- and master amplifier.
After the transfer function was determined, the potential for positioning was investigated. In a first step, the time delay caused by the acoustical sensor was approximated based on theoretical calculations. Then, the compete acoustical sensor, consisting of a piezo element, the pre- and the master amplifier, was integrated in an optical module. As a first dry run, an acoustical emitter was tied onto the exterior of the optical module and a position was chosen to obtain the maximum output signal strength. But this measurement did not lead to usable results. In addition, an upper limit for the possibility of the pinger detection in the background noise was determined: analytically calculated pinger signals with different amplitudes were merged with background noise, received from measurement with the integrated acoustical sensors. The effects of powered and disabled PMTs on the detection possibility were studied, as well as the effects of a digital band pass filter.
In the third part, eight complete hydrophones of four different kinds were characterized in order to obtain their properties and to search for unexpected effects. To achieve this, the pressure impulse response in a water tank was measured. With respect to the specifications of the emitter, the frequency dependent sensitivities of each hydrophone were generated and an additional transfer function was calculated for one type of hydrophone. Taking all this into account, it was found that there is a consistent behavior of the hydrophones. But with respect to the derived transfer function it cannot be

totally excluded that there are some unknown uncertainties in the emitters phase and consequently in the sensitivities of the hydrophones and the transfer function.

List of Figures

List of Tables

Bibliography

[1] Journal of Instrumentation, S Adrian-Martinez et al., *The positioning system of the ANTARES Neutrino Telescope*, iopscience, http://iopscience.iop.org/1748-0221/7/08/T08002

[2] KM3NeT Neutrino Telescope: http://www.km3net.org/home.php

[3] ANTARES Neutrino Telescope: http://antares.in2p3.fr/

[4] G. A. Askaryan, B. A. Dolgoshein, A. N. Kalinovsky and N. V. Mokhov, *Acoustic detection of high energy particle showers in water*, Nuclear Instruments and Methods 164 (1979) 267

[5] Doctoral thesis, C. Naumann, *Development of Sensors for the Acoustic Detection of Ultra High Energy Neutrinos in the Deep Sea*, Friedrich-Alexander-Universität Erlangen-Nürnber,17.09.2007

[6] ROOT software, F. Rademakers et al.,*A Data Analysis Framework*, CERN

[7] Bachlor thesis, Stefan Pickel, *Kalibration piezo-akustischer Sensoren für KM3NeT*, Erlangen Centre for Astroparticle Physics, 01.08.2012

[8] High Tech Inc.: http://www.hightechincusa.com/92_WB.html

[9] Sensor Technology LTD, Free Flooded Rings: http://www.sensortech.ca/site/index.cfm?DSP=Page&ID=99

[10] Security Multi-Sensor Integrated Devices (SMID) Technology: http://www.smidtechnology.it/

[11] National Institute for Subatomic Physics (NIKHEF): http://www.nikhef.nl/~jwschmel/.DOM-Ref-Pic/Dom_Antares_assembly/album/#

[12] Private Communication K. Graf, D. Kiessling (ECAP), November 2012

Danksagung

Ich möchte mich an dieser Stelle bei allen bedanken, die mich unterstützt haben, auch tatkräftig zur Seite standen und mir so diese Arbeit ermöglicht haben.

Ein besonderer Dank gilt:

Herrn Dr. Kay Graf und Herrn Alexander Enzenhöfer für ihre Unterstützung in technischen Angelegenheiten

Allen Mitgliedern der Akustik-Gruppe, für ihre Hilfsbereitschaft, umfangreichen Ratschläge und die absolut angenehme Arbeitsatmosphäre

Herrn Dr. Robert Lahmann für das Korrektur lesen

Angela Wilcke für die umfangreiche Unterstützung in der englischen Sprache

Ein besonderer Dank geht auch an all meine Freunde und Familie, die mich in dieser Zeit moralisch unterstütz haben.

Erklärung

Hiermit bestätige ich, dass ich diese Arbeit selbstständig und nur unter Verwendung der angegebenen Quellen und Hilfsmittel angefertigt habe.

Erlangen, 28. März 2013

Robert Karl